Nucleation and Growth of Pharmaceutical Crystals

A thesis presented in fulfilment of the requirements for the degree of
Doctor of Philosophy
in the Faculty of Science of the University of Strathclyde

By

Monika Warzecha

Strathclyde Institute of Pharmacy and Biomedical Sciences
April 2019

Declaration of Author's Right

This thesis is the result of author's original research. It has been composed by the author and has not been previously submitted for examination, which has led to the award of a degree.

Signed:

Date:

Acknowledgements

I would like to extend thanks to many people, who so generously contributed to the work presented in this thesis.

Firstly, I would like to express my sincere gratitude to Prof. Alastair Florence and Dr. Blair Johnston for giving me the opportunity to complete my PhD at CMAC and for their continuous support, patience, motivation, and immense knowledge. Their guidance helped me in all the time of research and writing of this thesis.

Special mention goes to Prof. Peter Vekilov who is the most enthusiastic scientist I have ever met. I would like to thank him for his tremendous academic support and for giving me the wonderful opportunity to visit his group at the University of Houston. I would like to especially thank Mohammad Safari for hosting me during my stay in Houston. I have very fond memories of my time there.

This thesis could not be completed without my colleagues from CMAC and CPOSS especially Prof. Sally Price, Dr. Rui Guo, Dr. Rajni Miglani Bhardwaj, Dr. Susan Reutzel-Edens and Dr. Vijay Srirambhatla from whom I received a great advice throughout the project.

I thank CMAC National Facility staff for provided training, especially Thomas McGlone and Laura Harvey for help with Raman and NMR measurements.

Last but not the least; I would like to thank my family, my parents and my beloved husband Bartosz for supporting me spiritually throughout writing this thesis.

Abstract

Investigating nucleation, crystal growth and solid-state transformations at the nanoscale are of significant interest, as more complex routes have roused questions about the classical view of these processes. This thesis reports the characterisation of prenucleation clusters in olanzapine (OZPN) aqueous solutions, their role in non-classical heteronucleation of OZPN hydrates and during crystal growth mechanism. Atomic force microscopy studies of the $(100)_{OZPNI}$ face of OZPN I crystals in contact with water show the formation, growth, and order of dense nanodroplets leading to crystallization of OZPN dihydrate on the surface of OZPN I. Dihydrate polymorphic form is driven by a templating effect of the underlying OZPN I lattice. The size and volume fraction of nanodroplets in purely aqueous and mixed ethanol and water OZPN solutions show that their radius is steady in time at *ca.* 35 nm and it is independent of the OZPN concentration and the solvent composition. The OZPN fraction captured in the clusters is dictated by the solution thermodynamics. Both behaviours are consistent with the predictions of a model that assumes the formation of OZPN dimers and their decay upon exiting the clusters. Although the presence of prenucleation clusters is critical during OZPN phase transformation, it was observed that clusters do not take part in a growth mechanism and OZPN layers are generated by a spiral growth. Step velocity shows a nonlinear dependence on OZPN concentration. The proposed growth model suggests that OZPN layers propagate by incorporation of OZPN dimers present as a minor species in OZPN solution. The growth by dimers is faster not owing to spatial or entropic factors or weakly bound solvent, but to the accumulation of dimers on crystal surfaces due to stronger binding.

These findings provide guidance towards enhanced control over nucleation, molecular transitions, and the solid forms in molecular systems.

Table of Contents

List of Figures

List of Tables

List of abbreviations

AFM – Atomic force microscopy

API – Active pharmaceutical ingredient

BM – Brownian microscopy

CIS – Complex induced shift

CNT – Classical nucleation theory

CMC – Critical micelle concentration

CSD – Cambridge structural database

CSP – Crystal structure predictions

CPA – Crystallisation by particle attachment

DLS – Dynamic light scattering

FDA – Food and Drug Administration

GRACE – Geometric real-space analysis of crystal epitaxy

IR – Infra red

NMR – Nuclear Magnetic Resonance

OZPN – olanzapine

OZPN DD – olanzapine dihydrate D

OZPN DB – olanzapine dihydrate B

OZPN HE – olanzapine hydrate ethanoate

PCNs – Prenucleation Clusters

PXRD – Powder X-ray diffraction

ROY – 5-methyl-2-[(2-nitrophenyl)amino]-3-thiophenecarbonitrile

RH – Relative humidity

SAXS – Small angle x-ray scattering

SLS – Static light scattering

TEM – Transmission electron microscopy

WAXS – Wide angle X-ray scattering

List of Symbols

β – step kinetic coefficient

β_{ad} – kinetic coefficient for adsorption

β_{surf} – kinetic coefficient for incorporation from the terraces

γ – surface free energy for a unit area

δ – NMR shift

ε – binding energy of the atoms

ε – extinction coefficients

λ – characteristic length of surface diffusion

Λ – resistance to enter the step from bulk solution to the crystal surface

Λ_s – resistance for incorporation into kinks from the surface

μ – chemical potential of the solution

η – viscosity

ν – solute fraction

σ – supersaturation ratio

ϕ – volume fraction

Ω – the volume of the molecule

A – pre-exponential kinetic factor

B – nucleation thermodynamic factor

C_e – concentration at equilibrium

C_D – concentration of dimers

C_{M-} concentration of monomers

D – diffusion coefficient

D – diffusivity of molecules from solution

d_{hkl} – interplanar distance

Dz – cantilever deflection

E_{att} – attachment energy

E – Epitaxial scores

ΔG^{o}_{cryst} – free energy of crystallisation

ΔG_v – volume free energy

ΔG_s – surface free energy

ΔG^{*} – free energy barrier for incorporation into a kink

ΔH^{o}_{cryst} – crystallisation enthalpy

$H_{crystal}$ – enthalpy of the crystal

$H_{solution}$ – enthalpy of the solution

$\Delta H^{\neq}$ – enthalpy change of the transition state

$\Delta H^{\neq}_{ads}$ – kinetic barrier for incorporation of a molecule to a growth site

$\Delta H^{\neq}_{des}$ – kinetic barrier for detachment of a molecule from a growth site

ΔH^{o}_{ads} – enthalpy change for adsorbed molecules on a surface

J – crystal nucleation rate

j_{+} – number of molecule entering a kink per second;

j_{-} – number of molecules leaving the kink

k – spring constant

K_D – dimerization constant

k_B – Boltzmann's constant

ℓ – step separation

ρ_k – kink density

$N_{cluster}$ – concentration of clusters

R – cluster radius

r_{crit} – critical radius

r – interatomic distance

ΔS^{o}_{cryst} – crystallisation entropy

$\Delta S^{\neq}$ – entropy change of the transition state

$S^{\neq}$ – entropy of transition state

$S_{solution}$ – entropy of the solution

T – absolute temperature

U_{ads} – adsorption energy

v –step velocity

v^{+} – effective frequency of attempts by a solute molecule to enter a kink

$q_{rotation}$ – molecular rotation partition function

List of publications

Warzecha, M.; Guo, R.; Bhardwaj, R. M.; Reutzel-Edens, S. M.; Price, S. L.; Lamprou, D.; Florence, A. J. Direct Observation of Templated Two-Step Nucleation Mechanism during Olanzapine Hydration. *Cryst. Growth Des.* **2017**, *17* (12), 6382–6393.

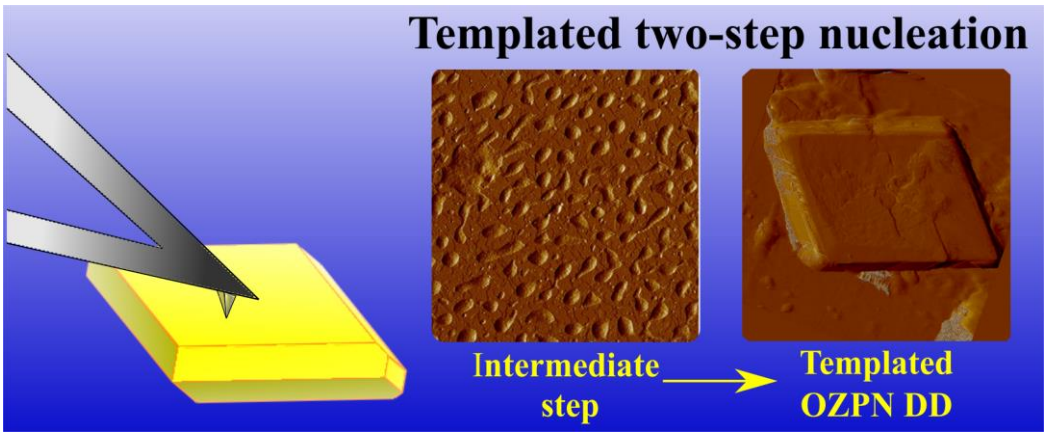

Warzecha, M.; Florence, A. J.; Safari, M.; Vekilov, P. G. Mesoscopic Solute-Rich Clusters in Solutions of the Schizophrenia Drug Olanzapine. *Cryst. Growth Des.* **2017**, *17* (12), 6668–6676

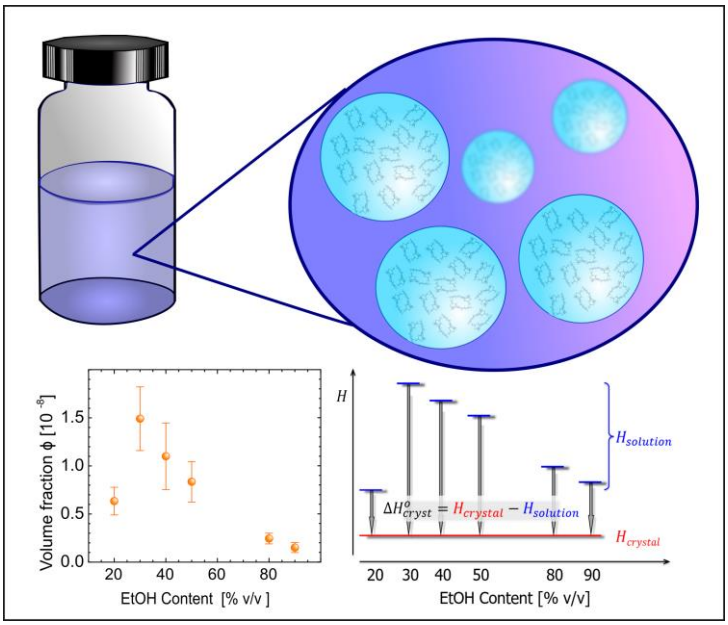

1 Introduction

1.1 Role of crystallisation in the pharmaceutical industry

Crystallisation is widely used to control the purity and solid-state properties of active pharmaceutical ingredients (API) and others chemicals. Since organic molecules may crystallise in numerous solid-state forms each with distinct physical properties, there is a significant interest in the pharmaceutical industry in controlling size,[1] purity,[2] morphology,[3] and crystal structure.[4] While both the crystal morphology and size are important for downstream processing such as filtration, drying and milling, crystallising the inappropriate polymorph directly impacts key biopharmaceutical attributes including solubility and may have serious consequences for human health. This can also bring high reformulation costs to a manufacturing process. Efforts in advancing design strategies, growth techniques, and characterisation of pharmaceutical crystals has progressed dramatically in the last two decades since the critical case of Ritonavir, where a metastable polymorph reverted to a less soluble form during the manufacturing process, reducing the bioavailability of the formulated dosage with $250 million reformulation costs.[5] Although metastable forms may exhibit not only the higher solubility but also other physical properties such as compressibility (e.g. paracetamol form II),[6] the most stable polymorph is typically desired for manufacturing and solid-form screening is a regulatory requirement for new pharmaceuticals. With strict standards from the US Food and Drug Administration (FDA) there are a limited number of formulations that include metastable forms or co-crystals. While experimental solid-form screening generates multiple useful information about physical and chemical properties of new solid-state forms these studies are time-consuming and costly. Crystal structure prediction (CSP) methods are used as a complementary technique to experimental screening.[7–9] Advancements in

algorithms and computer power have introduced significant advantages in terms of accuracy and time in predicting crystal structures, yet these cannot be considered as entirely reliable. Over-prediction is still a problem with CSP as it does not lead to a single crystal structure, but rather to many possible structures within a small range of energy (~5 $kJ \cdot mol^{-1}$).[10] Therefore, studies combining solid form screening and crystal structures predictions, provide a more complete picture and better understanding of the solid-state diversity of organic compounds. The standard approach for polymorph screening includes solvent, temperature and supersaturation control. However more examples show that less conventional approaches, including templating with surface attributes such as topography,[11,12] lattice matching,[8,13–15] or molecular functionality,[16–23] are more successful in producing less accessible polymorphic forms.

Crystallisation outcomes are still not fully predictable as crystal nucleation, growth and polymorphic transformations are not completely understood. Nucleation and growth processes are difficult to monitor experimentally at the molecular level due to the short timescales and small sizes of the nuclei involved. Considerable efforts continue to be devoted to understanding nucleation processes[5] including using dynamic simulations.[6] Classical nucleation theory (CNT) [24–28] is widely applied to describe crystal nucleation kinetics from solution. However, it cannot fully explain all observed phenomena. Recent studies have shown evidence of a two-step nucleation process[29–32] in which the initial formation of clusters of a dense, disordered, liquid-like phase precedes the formation of an ordered solid nucleus inside clusters. Evidence for two-step nucleation has been observed in protein crystallisation,[33–36] with the existence of pre-nucleation clusters (PNCs) comprising small, thermodynamically stable solute clusters also being reported for inorganic systems including calcium carbonate and

calcium phosphate.[37–40] It has been proposed[38] that within PNCs local ordering of structural motifs corresponding to specific crystalline polymorphs can occur, influencing the resultant crystal form obtained. The formation of dense clusters has also been observed in aqueous solutions of organic molecules (including several amino acids such as glycine, aniline and DL-valine[41–45]), polymers[46] and inorganic structures including heteropolyacids[47] and InP quantum dots.[48] The increasing evidence for two-step nucleation in organic, protein and inorganic systems suggests it may play a significant role in the formation of crystals under many different situations.

Recent publications suggest that metastable clusters also have a significant role in the crystal growth mechanism.[31,49–51] In contrast to widely accepted crystal growth by monomer-to-monomer addition (Figure 1), formation of new crystal layers by sedimentation and spread of metastable species such as dense liquid droplets, amorphous nanoparticles, prenucleation clusters, or nanocrystals (Figure 1) is now recognized. Observation of crystal formation and growth is achievable due to advancement in nanoscale techniques such as dynamic light scattering (DLS), transmission electron microscopy (TEM),[43,52] *in situ* small-angle and wide-angle X-ray scattering (SAXS/WAXS)[53] and in particular, atomic force microscopy (AFM)[54–60] which has been widely applied to characterize both classical and non-classical crystal growth mechanisms.

The complexity of nucleation and growth mechanisms of pharmaceutically relevant products raises questions about the ability to truly predict and control the crystallisation outcomes.[61–64] Clearly, a better understanding of how molecules assemble from a solution or melt needs more fundamental investigation. Considering the non-classical

mechanism for nucleation and growth, deeper understanding of the nature and evolution of the various metastable species is needed, especially for the purpose of modelling crystallisation outcomes. Since there is some strong indication that solvents can direct the self-association of the molecules in solution,[65–70] there is a question about the growth units for the nucleus and crystal layers and how they are related to the attachment frequency of the molecules. Additionally, in most cases the molecular mechanism of the transformation of the metastable to more stable form remains unknown. Hydrates formation is especially important due to the widespread exposure of APIs to water, whether in solution or vapour form, since the incorporation of water molecules in the crystal lattice can have a dramatic effect on solubility and possibly bioavailability of an API. Finally, it is also unclear how surface and solvent properties enhance nucleation and drives the polymorphic selection, especially how it can be used on a wider scale to enable a full control over the crystallisation outcomes.

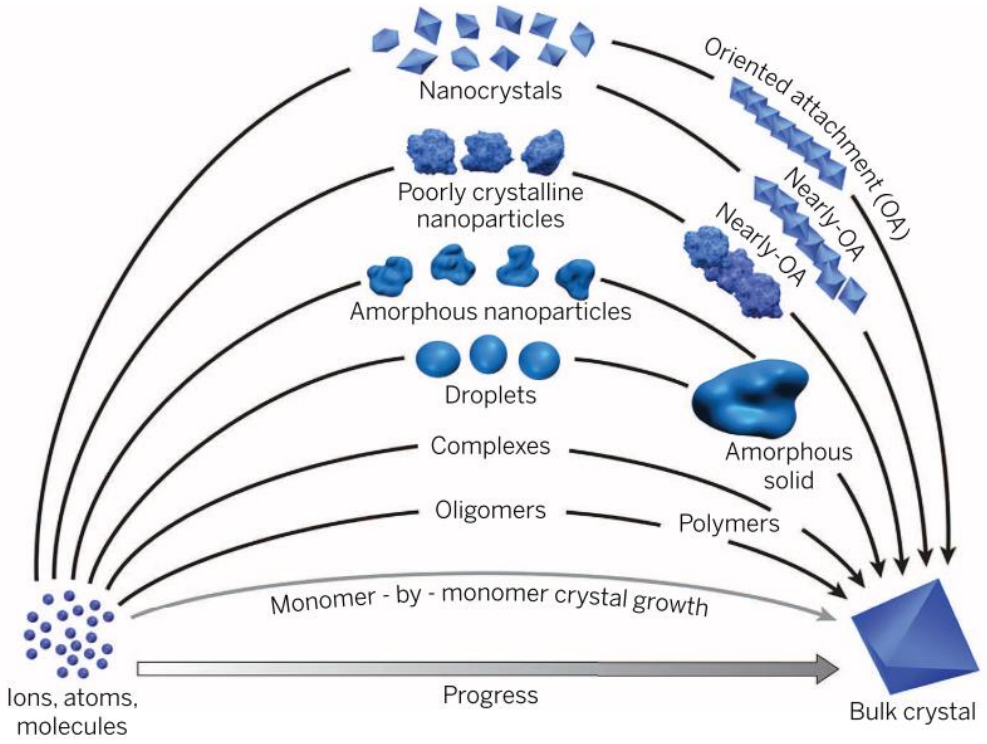

Figure 1 Pathways of non-classical growth. In contrast to monomer-by-monomer addition as envisioned in classical models of crystal growth (grey curve), non-classical crystal growth occurs by the addition of higher-order species ranging from multi-molecule complexes to ordered nanocrystals. Copied from reference.[49]

1.2 Classical nucleation theory

Understanding the fundamentals of nucleation is essential to control crystallisation processes. Primary (homogeneous) nucleation occurs when crystalline surfaces are not present, whereas secondary nucleation requires the presence of parent (seed) crystal surfaces (of the same compound) and their interaction with the surrounding medium.[71–73] If the seed surface of a different material is used for crystallisation (specially designed template or a dust particle), heterogeneous nucleation occurs.

Two main models have been proposed for primary nucleation mechanisms: classical nucleation theory and two-step nucleation theory. CNT assumes that the first step of

nucleus formation requires a supersaturated solution containing the solute present in the form of free monomers, this may give a beginning of a small ordered cluster. The formation of nuclei is associated with a free energy change ΔG_{crys}, which is given as the sum of the gain in a volume free energy ΔG_v (green curve, Figure 2), associated with the formation of intermolecular bonds, and the loss in free energy by the formation of a surface ΔG_s (red curve, Figure 2). The free energy change ΔG_{crys} for an initialised nucleus in solution (assuming spherical shape) is described as (Equation 1):[74]

$$\Delta G_{crys} = -\frac{4}{3}\pi r^3 \Delta G_v + 4\pi r^2 \gamma \quad (1)$$

where r is the radius of the spherical nucleus, and γ is the surface free energy for a unit area. Consequently, unfavourable interfacial contribution dominates at small sizes and the favourable bulk term dominates at large sizes (blue curve, Figure 2).

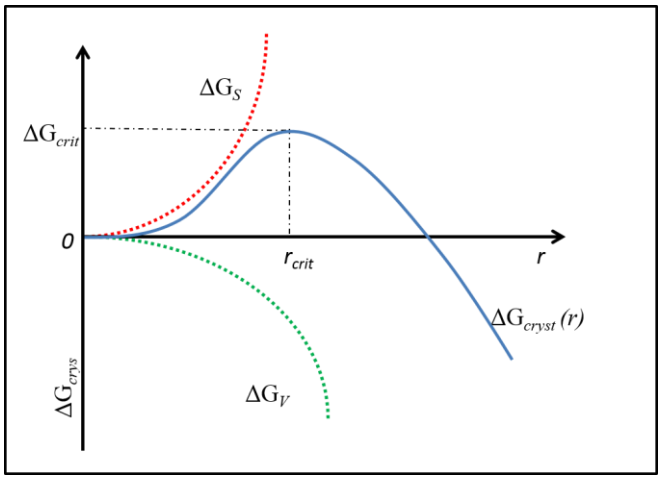

Figure 2 Free energy diagram for nucleation according to CNT. Adapted from reference [101]

The initial total free energy increases initially until it reaches the activation energy for nucleation, ΔG_{crit} at the corresponding radius r_{crit} (Equations 2 and 3).

$$\Delta G_{crit} = \frac{16\pi\gamma^3}{3\Delta G_v{}^2} \quad (2)$$

$$r_{crit} = \frac{2\gamma}{\Delta G_v} \quad (3)$$

Above this critical size the total free energy constantly decreases and growth becomes energetically favourable, resulting in the formation of the crystal nuclei. The crystal nucleation rate *J* is equal to the number of nuclei formed per time and unit volume, as described by (Equation 4):[75]

$$J = Aexp\left(-\frac{B}{ln^2\sigma}\right) = Aexp\left(-\frac{\Delta G_{crit}}{kT}\right) \quad (4)$$

where σ is the supersaturation ratio, k is Boltzmann's constant and A is the pre-exponential kinetic factor that is related to the rate of attachment of molecules to the critical nucleus, B is a thermodynamic factor and reflects the structure of the nucleus.

CNT assumes that nuclei grow by incorporating each monomer individually and that crystal nuclei have the same structure as that of the bulk crystal. Therefore, widespread intermediate metastable species in aqueous solutions of organic molecules including several amino acids,[42–45] polymers[46] and inorganic structures[47,48] cannot be explained by the CNT. Additionally, CNT does not provide any information about the nature of clusters formed in undersaturated solutions and does not take into consideration the impact of solvent-induced molecular self-association in solution on the polymorphic effect. Furthermore, classical nucleation theory does not predict correct crystal

nucleation rates, as the pre-exponential factor *A* (Equation 4) remains undetermined and is usually adjusted to fit the experimental data.[76]

1.3 Two-step nucleation theory

Intensive studies of proteins and colloidal system crystallisations, supported by computer studies are in favour of the two-step nucleation mechanism. Two-step nucleation theory suggests that the formation of crystal nuclei from supersaturated liquid is described by two transitions (Figure 3), firstly by the formation of a droplet of a dense liquid, metastable with respect to the crystalline state, followed by ordering within this droplet to produce a crystal.

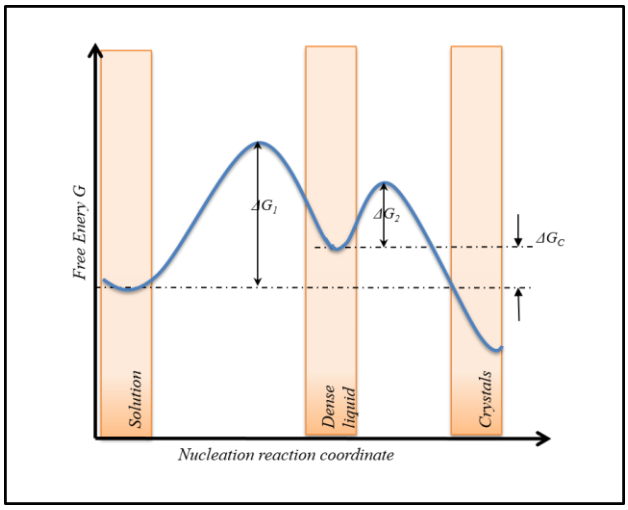

Figure 3 Free energy ΔG for two-step nucleation of crystals from solution. Adapted from reference.[31]

Studies on protein crystallisation have made a big contribution to the development of the two-step mechanism. They have been observed in solutions of several proteins: lysozyme,[35,36] haemoglobin A and S,[77] glucose isomerase,[51] and lumazine synthase.[31,78] It was first demonstrated that dense liquid droplets assist the nucleation of the protein lysozyme followed by nucleation of a crystal within the droplet under a

wide range of conditions (Figure 4 a). Their extended lifetimes indicate that the clusters are not concentration fluctuations and surprisingly, lysozyme dense clusters of sizes ~100 nm were also detected in a homogenous region of a phase diagram. The clusters contain $10^3 – 10^4$ molecules and occupy less than 10^{-3} of the total solution volume. It was shown that the cluster population volume responds to varying protein concentration although, the cluster size was independent of protein concentration.[35,77,79] The decoupled behaviours of the cluster size and population volume contradicted predictions of classical theories of phase transformation and aggregation models. The developed two-step nucleation theory suggests that the mechanisms determining the cluster size is dictated by the dynamics of formation and decay of protein oligomers of a limited lifetime. Hence, it was concluded that such oligomers are required for the clusters' existence.[35] Further studies[80] also showed other types of prenucleation species present in lysozyme supersaturated solutions. All kind of particles exhibited spherical shape, although the internal structure and their role during crystal nucleation process varied. Some particles after growing to the certain size developed crystal faces and eventually transformed to orthorhombic lysozyme crystal (Figure 4 b) while others had a more solid-like character and served as a surface for heteronucleation of a lysozyme crystal (Figure 4 c).

Experimental observations of nucleation show an increasing number of other chemical systems where the presence of prenucleation clusters is a common step. Prenucleation clusters were detected during nucleation of calcium carbonate, calcium phosphate and silica. These clusters were reported to be highly dynamic and thermodynamically stable solutes in equilibrium with surrounding solution. In supersaturated solution of calcium phosphate clusters coalesced and formed a layer of amorphous calcium

phosphate that next transformed to crystalline calcium phosphate.[81] It has been proposed[38] that within PNCs local ordering of structural motifs corresponding to specific crystalline polymorphs can occur, influencing the resultant crystal form obtained. The presence of an amorphous phase was only observed for inorganic compounds and never observed for any other systems.

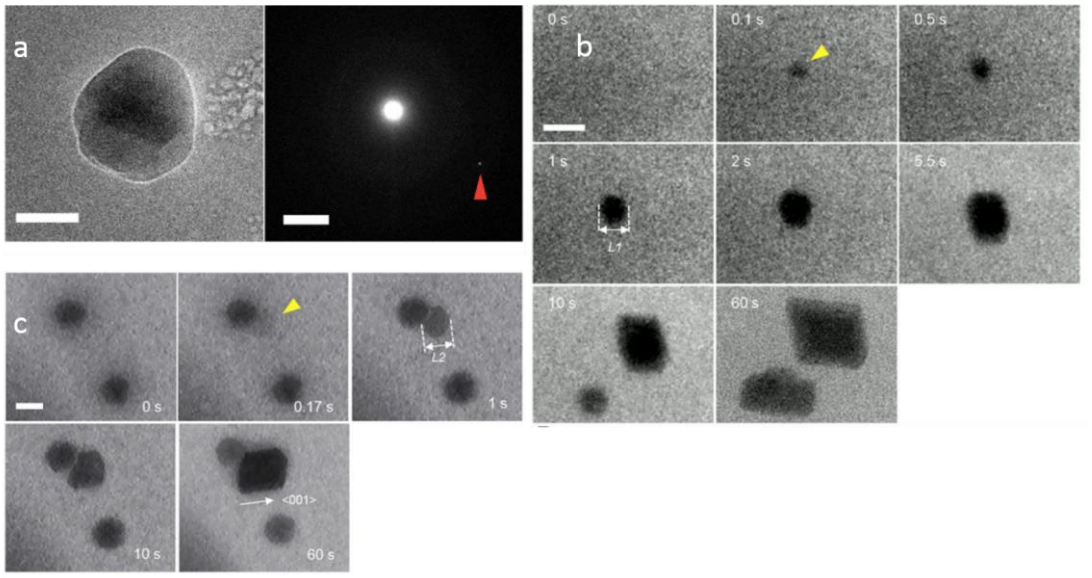

Figure 4 The nucleation of lysozyme crystals assisted with various types of prenucleation clusters, a) nucleation of a crystal in a liquid droplet, b) transformation of a spherical particle to a orthorhombic crystal, c) pre-nucleation cluster serve as a surface for a crystal nucleation. Copied from reference.[80]

In the case of small organic compounds it was demonstrated that the dissolution of glycine and DL-alanine[43,45] in water leads to the formation of a solution containing submicron size mesospecies (Figure 5). Their size distribution depends on the concentration and chemical properties of the solute. Dissolution of glycine crystals in water showed mesospecies with a mean diameter of ~250 nm. Glycine crystals were reported to grow only when smaller species coalesce to larger nanodroplets (diameter >750 nm) since a critical mass of glycine was required to form crystals large enough to be stable in less concentrated solution.

Molecular dynamic simulation of the nucleation process of urea suggest that nucleation pathways strongly depend on the solvent system. Simulations for three different solvents (methanol, ethanol, and acetonitrile) revealed that in methanol and ethanol urea forms crystal-like clusters suggesting one step nucleation directly from solution, while in acetonitrile urea first forms disorder clusters indicating a two-step nucleation mechanism.[82] This diverse role of prenucleation particles present in the solution shows the importance of further nucleation studies also in different systems.

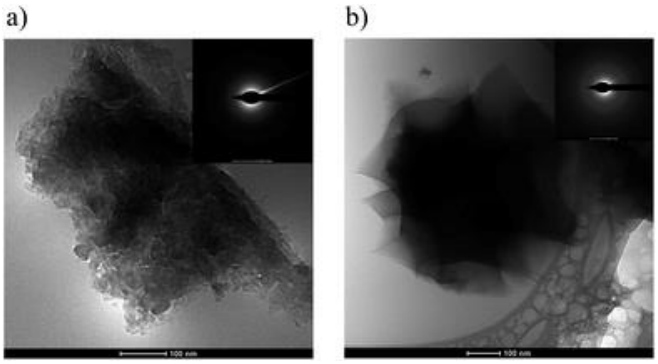

Figure 5 Cryo-TEM images of colloidal (a) DL-alanine 150 mg/mL and (b) glycine (200 mg/mL). Copied from reference [43]

A two-step nucleation mechanism was also proposed during the heterogeneous nucleation of organic molecules on carbon nanohorns.[83] The impurity surface may have the ability to induce order within the dense prenucleation clusters and lower the surface free energy for nucleation as well as effectively template the resultant crystal form. Clearly, a better understanding of how surfaces can influence the structure of prenucleation species could provide a basis to select or design surfaces that specifically template crystalline materials with desirable solid-state properties.[8,15]

1.4 Classical crystal growth mechanism

After a stable crystal nucleus is formed, their growth continues to macroscopic crystals. Crystal growth is governed by internal factors such as three-dimensional crystal structure and crystal defects, and external factors such as temperature, supersaturation, solvent, and the presence of impurities. While the first group will affect intermolecular interactions between the crystal surface and the solution the second group will affect the type of interactions at the solid-liquid interface.[84]

When growth occurs by addition of a monomer from a solution to a crystal surface this is considered as a classical growth mechanism. A crystal surface contain the three most characteristic sites where monomers can be attached, mainly kinks, terraces and steps.[85] Kinks are energetically most favourable positions where molecules can be built into a crystal surface since there is a maximum number (three) of bonds that are created during that process. This equals to a half of the possible crystal lattice intermolecular interactions. In comparison, there are two bonds created then the molecule adsorbs to the step and one for the terrace. After the solute molecules diffuse toward the face of the crystal, monomer incorporation may occur either through direct incorporation[86] to the kink site (Figure 6, path *a*) or by surface diffusion.[87–89] Surface diffusion occurs when a monomer is first adsorbed to the terrace and then diffuses along the crystal surface to the growth site (Figure 6, path *b*). During direct incorporation from solution to a kink site a molecule encounters a single energy barrier that takes into account multiple factors, including the orientation of the molecule, the geometry of the site, and the displacement of solvent (Figure 6 c). During surface diffusion incorporation of molecules from the solution to the kink include the kinetic barriers for adsorption on a

terrace, desorption, diffusion along the surface toward a step, and attachment to a growth site (Figure 6 d).[87,90]

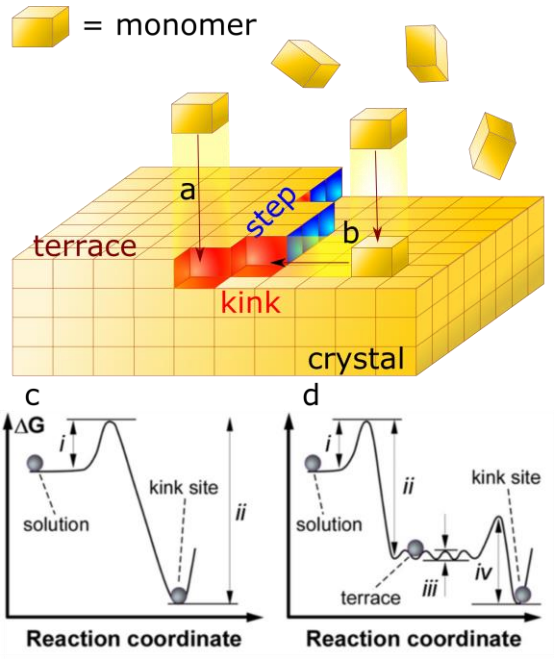

Figure 6 Classical growth mechanism by monomer-by-monomer addition (monomers are illustrated as blocks) where a) monomers attach to the growth sites or b) monomers adsorb onto terraces followed by possible surface diffusion and incorporation into growth sites, c) The free energy profile for direct incorporation into a step. i and ii are the kinetic barriers for incorporation and detachment of a molecule from a growth site, respectively, d) The free energy profile for the surface diffusion mechanism. i, ii, iii, and iv are the kinetic barriers for, respectively, adsorption, desorption, surface diffusion, and incorporation into steps from the surface. Copied from reference [87]

Classical crystal growth typically involves two-dimensional (2−D) layered growth or rough growth.[91] If faces of the crystal are mostly composed of kink sites, molecules can incorporate into the crystal at all positions. In this situation, growth is limited only by the transport of solute molecules to the surface and this process is described as rough growth. If the density of kink sites is much lower, layered growth occurs and 2−D nucleus spreads across the face by addition of the monomer until the new layer is finished and reaches the boundary of the crystal edge. When a screw dislocation is present in the crystal lattice and terminate on a crystal face, crystal faces grow via the

spiral growth mechanism.[60,63] Screw dislocation serve as a continuing source of steps where new molecules can be built into the crystal face. The steps will grow in its onward direction until it encounters a boundary, while the new steps will continually be generated at the dislocation.

The role of solvent ordering in crystal growth is not yet clear, although it is well known that the choice of solvent is one of the most critical decisions when designing the crystallisation process. Solvent molecules influence the solubility, impurity rejection and most importantly crystal morphology. A lot of attention is paid to the control of the morphology of API crystal in the pharmaceutical industry, because of the influence of the crystal morphology on downstream processes like filtering, drying, blending, and tableting.[92] Needle-shaped and plate-shape crystals are quite difficult to handle due to their breakage during processes required to formulate drug product, making the manufacturing process less efficient.[93] Design of modelling tools[61–64] for crystal morphology screening is only accurate when the full picture of the interaction between solvent-solute, solute-solute, solute-surface and solvent-surface during growth from solution is known. Therefore, further understanding of the growth mechanism and a role of solvent leads to a better design of crystallisation process, prediction of the crystal morphology and rational design of growth modifiers with desired specificity.[94]

1.5 Non-classical crystal growth mechanism

When a crystal growth occurs by attachment of growth units that have a higher configuration than a monomer (dimers, trimers, clusters of molecules or nanocrystals), it is considered as a non-classical crystal growth mechanism and is it now recognised as a common phenomenon.[39,51,95] This mechanism involves the presence of crystal

layer precursors in a solution that can be incorporated into a crystal surface and contribute to the growth of the crystal layers. Precursors are formed in a solution and differ in complexity and composition (Figure 7), from simple dimers, through oligomers and mesoscopic liquid-like droplets,[31,50] amorphous particles[96,97] or nanocrystals.[98,99] The structure of the oligomers is usually simple and their presence in solution can be easily confirmed by techniques such as IR or NMR spectroscopy,[67,69,100,101] in contrast to the characterisation of the internal structure of more complex precursors. Analogous to monomers, oligomers can be adsorbed on the growth sites on the crystal surface, although up to date growth via oligomers has not been confirmed directly. The assumption that crystals can grow by oligomers comes from the fact that their structures can be often detected in a solution[67,69,100,101] or they are a common motif in many crystal structures of the same compound.[62]

The pathways for other precursors may involve attachment of particles such as crystallographically aligned nanocrystals, polycrystalline nanoparticles, disordered clusters or liquid-like droplet. This mechanism is generally called crystallisation by particle attachment (CPA).[49] It was mostly observed for biocrystallisation and the crystallisation of inorganic materials such as zeolites. However there are more studies showing it is also valid for organic systems such as proteins and amino acids.

For protein crystallisation,non-classical growth mechanism was first observed for lumazine synthase.[31] The crystal growth mechanism involved the sedimentation of a submicron dense droplet on the crystal surface and its incorporation into the crystal layer. Droplets landed on the crystal surface between existing steps, then grew sideways and became an integral part of the crystal, generating five new layers as

shown on the Figure 8 a. The droplets were able to take part in the growth mechanism since the internal mobility of the protein molecules inside the droplets is considered high and the molecules can be rearranged under the influence of the periodic structure of the underlying crystal generating new ordered layer.

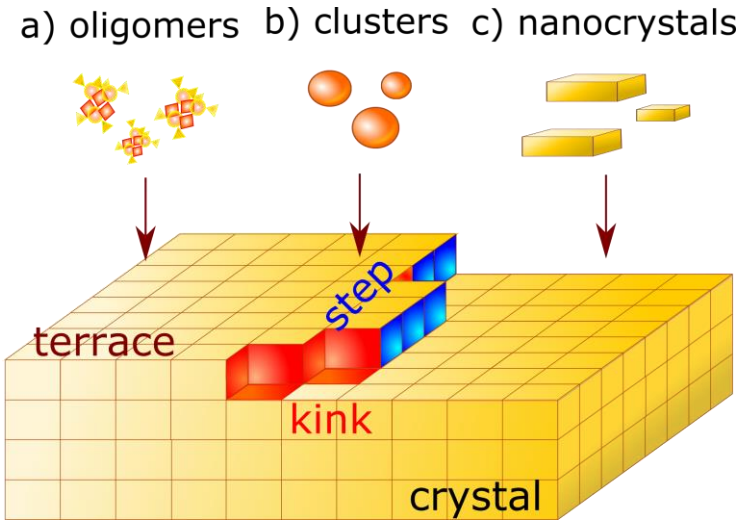

Figure 7 Non-classical crystal growth pathways can involve the formation of a) oligomer species, b) amorphous clusters, c) nanocrystalline particles that directly add to the crystal surface.

For small organic molecules a new growth mode for crystals of DL-glutamic acid monohydrate through the attachment of nanoscopic clusters from solution was confirmed by AFM.[50] Clusters of a size ~4 nm high and 150–300 nm wide were observed on the surface of a DL-glutamic acid monohydrate crystal placed in a growth solution. Some of the clusters dissolved (e.g. Figure 8 b, green circles), although most of the clusters served as a source of new crystalline layer with the same height as those in the parent crystal (e.g. Figure 8 b, red circles). Next, the layers were observed to grow by the additions of monomers. Interestingly, when the same clusters were adsorbed on the silica wafer surface they did not transform into a crystalline layer, which suggests that the significant chemical or structural match between the surface

and the clusters is necessary to enable their rearrangement and incorporation into a crystal layer.

With the discovery of new growth mechanisms, several new questions regarding the control over the non-classical growth process emerge. It remains unclear what are the most active sites on the crystal surface are for the precursor attachment or what is the relationship between the supersaturation, growth rates and number of precursors present in solution. Also due to limited of knowledge about how solvent or temperature affects the structure and a number of precursors it is difficult to implement the observations of the non-classical growth mechanisms in current modelling frameworks. Additionally, without the knowledge of fundamental processes occurring inside the clusters during disorder to ordered transitions it remains impossible to design potential modifiers for non-classical growth process.

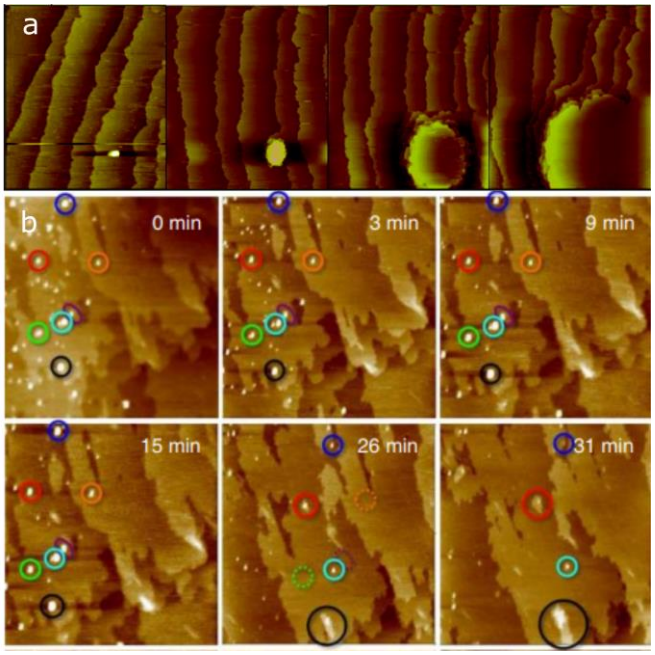

Figure 8 Example of non-classical growth for organic molecules, a) Lumazine synthase-sedimentation of a 3-D object and its development into a stack five crystalline layer, copied from reference, [31] b) DL-glutamic acid monohydrate- clusters marked with coloured circles contribute to the growth of a single crystal layer copied from reference.[50]

1.6 Techniques to study crystal nucleation and growth

Crystal nucleation and growth studies are more and more accessible due to rapid development of nanoscale imaging techniques. Light scattering techniques such as DLS, SLS or oblique illumination microscopy (OIM, also known as Brownian microscopy, BM) are good tools to study the physical properties of prenucleation nanoclusters while microscopy techniques such as optical microscopy, scanning electron microscopy (SEM), transmission electron microscopy and atomic force microscopy are useful tools for imaging the mechanisms of the crystal growth. Additionally, infrared (IR), Raman and nuclear magnetic resonance spectroscopy are able to provide information about the solution composition and solute-solute interactions.

1.6.1 Infra-Red and Raman Spectroscopy

IR and Raman spectroscopy are very common vibrational spectroscopies used in determining the conformation of compounds. These techniques allow rapid and nondestructive measurements without sample preparations. In IR spectroscopy, the molecules absorb infra-red light, and the intensity of the absorption is measured by Lamber-Beer Law. In Raman spectroscopy, a sample is irradiated with intense, monochromic laser beam and inelastically scattered light intensity is measured in the direction 90° or 180° to the incident beam. Raman vibrational transitions are in the same range as IR absorption (200 – 4000 cm^{-1}). Selection rules for Raman scattering and IR absorption are different, however the information obtained about the structure are similar. To determinate whether a vibration is active in IR and/or Raman spectroscopy the selection rules must be applied to each normal vibration. According to quantum mechanics, a vibration is IR-active if the dipole moment is changed during the vibration. The vibration is Raman active if the polarizability is changed during the vibration, making both techniques complementary. IR and Raman spectroscopy are widely used to study intermolecular interaction in a solution and solid state in particular the correlation between self-association of the solute in the solution and in the solid-state structure. Several studies[100–103] report direct correlation between the dimers present in the solution and the presence of dimer in the crystal structure.

1.6.2 Nuclear magnetic resonance spectroscopy (NMR)

NMR spectroscopy is a technique based on phenomena occurring when the nuclei unpaired proton with ½ spin (^{1}H, ^{13}C, ^{19}F or ^{31}P) is placed in strong magnetic field. Nuclei may take up either a low-energy orientation (aligned with the field) or high-

energy configuration (against the field). When the system is in equilibrium the lower level (N1) will have a higher population than higher level (N2) the energy difference between them will be equal to *ΔE* [MHz]. NMR technique is sensitive to the nuclei environment and identical functional groups with differing neighbouring substituents give distinguishable signals. ^{1}H NMR spectroscopy can be used to investigate solution aggregation processes. Experimental complexation-induced changes in chemical shift[104] can be used to determine the three-dimensional structures of solution phase aggregates.[65–67,105]

1.6.3 Oblique lllumination microscopy

OIM is a technique designed to measure the size of single particles in solution using light scattering. The method relies on light scattered at wavevectors of order μm^{-1} and probe lengthscales in the range 10^{-3} – 10 μm. The Rayleigh law, according to which the scattered intensity scales as the sixth power of the scatterers' sizes, makes this technique particularly well suited to study the mesoscopic, 50 to 100 nm large clusters, but are present at very low concentrations. OIM is also referred to as Brownian microscopy[106–108] or particle tracking.[109] The clusters are visualised as coloured sparkles. As the clusters are smaller than the diffraction limit, the speckle size accounts for the deviation of the cluster position from the microscope focal plane. The Brownian trajectory of a particle is recorded in the image plane (Figure 9 c), and the correlation between the mean squared displacement $\langle \Delta x^2 \rangle$ and the lag time Δt is computed.

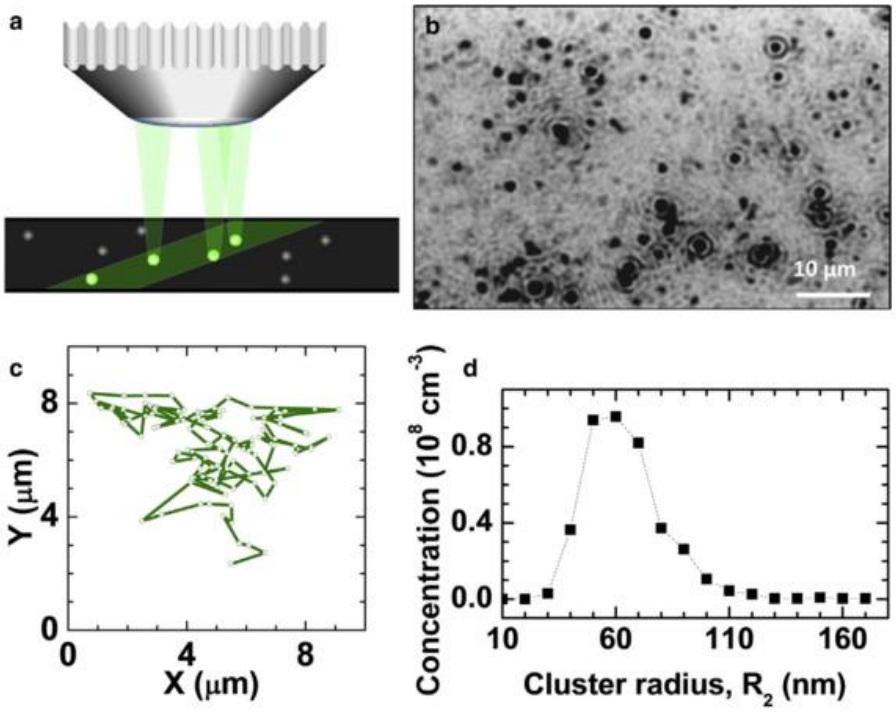

Figure 9 Characterization of particles by OIM. a) The OIM set up, b) a typical OIM image shown as a negative, in which clusters appear as dark speckles, c) a typical cluster trajectory obtained from the position of a cluster in a sequence of images, d) The distribution of cluster sizes obtained from five OIM movies recorded at distinct solution volumes. Copied form reference.[109]

The diffusion coefficient *D* is calculated from the slope of the $\langle \Delta x^2 \rangle(t)$ correlations; using the first five data points as they provide the highest accuracy of *D*.[109] The cluster radius *R* is determined using the Stokes-Einstein relation, equation 6, Figure 9 d:

$$R = k_B T / 6\pi\eta D \tag{6}$$

Additionally, the cross polarizer can be used to determine the internal order of the observed particles. OIM was used for studies of the size and evolution of prenucleation species for protein and amino acid crystallisation.[36,44,45,106]

1.6.4 Electron microscopy

The electron microscope was invented in the middle of the 20th century to address the need for higher optical resolution. There are two main types of electron microscopes SEM and TEM. Both types of microscopes use a beam of electrons to create an image of the specimen. SEM uses low energy electron beam (1 – 30 keV) compared to TEM (100 keV – 1 MeV) and produce three-dimensional (3–D) images from secondary or back-scattered electrons from the sample, while TEM only produces flat (2–D) images by transmitting electrons through the sample. Furthermore, TEM provides the higher resolution and magnification (0.1 nm), plus provides details about internal composition. Electron microscopes have undergone big improvements over the last few years, e.g. development of *in-situ* techniques allows the observation of crystal nucleation in real time without concerns that the sample has been transformed during the measurement. *In-situ* CryoTEM helped to observe mesopecies of DL-alanine and glycine[45] with diameters in the range ca. 100 to 300 nm (Figure 5). It is also widely used to study non-classical processes of nucleation and growth of inorganic materials.[38,50,110]

1.6.5 Atomic force microscopy

Atomic Force Microscopy has been the most widely used technique for analysis of the classical and non-classical crystal growth of proteins, amino acids, small organic molecules, pathological crystals[87,111–115] and zeolites[116] and other inorganic materials.[55,57,59,60] It was also used to observe phase changes,[56] crystal morphology,[54] and to study dissolution.[58] AFM is a kind of scanning tunnelling microscope (STM), although compared to STM, AFM does not require the sample to be conductive;

therefore, a wider range of samples and various environments can be studied. The AFM operation is based on the atomic forces such as van der Waals, Coulombic attraction, capillary forces and chemical potential. A tip (Figure 10 a, b) is located at the end of the cantilever, which bends as a consequence of atomic forces present between the tip and the surface. The tips differ in size (from single molecules at the apex for an atomic resolution imaging to a few hundred nanometres for nanoindentation measurements) and shape (from spheres to needle like) depending on the application. According to Hooke's Law (Equation 7) cantilever deflection (*dz*) is directly proportional to the force (F_{res}), which is needed to restore the cantilever to its equilibrium position. AFM is highly sensitive to small forces owing to small tip radius (5 – 50 nm) and elastic cantilever (100 – 500 μm long).

$$F_{res} = -k_{res}dz \tag{7}$$

The cantilever deflection is usually detected by an optical technique. Usually, laser light beam is reflected from the cantilever onto a position sensitive-photodetector (Figure 10 a).

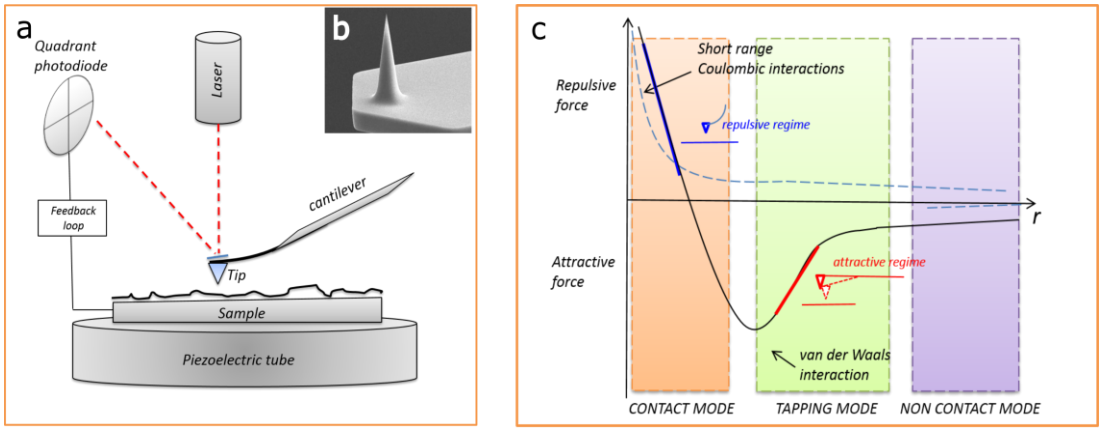

Figure 10 a) Schematic of AFM setup, b) field of view 30 microns, c) intermolecular interactions and atomic force mode operations.

Interaction between the tip and atoms can be described by van der Waals interactions model (Figure 10 c) and Lenard-Jones empirical potential (Equation 8):

$$V_{L,J} = 4\varepsilon\left[\left(\frac{\sigma}{r}\right)^{12} - \left(\frac{\sigma}{r}\right)^{6}\right] \tag{8}$$

where ε is the binding energy of the atoms, σ is an atom diameter, and r is the interatomic distance.

AFM can work both in force-mode (adhesion, cohesion forces, hardness and elasticity measurements) and imaging mode. In imaging mode, the images are produced by a raster scan by the tip moving back and forth along the fast axis (usually *x*-axis). When one line is completed the tip is moved by a small increment in perpendicular direction (slow axis, *y*-axis) and the process is repeated. The imaging mode can be divided into contact mode, tapping mode, non-contact and newly introduced Peak Force Tapping™. In contact mode, the force between the probe and the sample is repulsive (Figure 10) and remains constant while an image of the surface is obtained. The change in deflection reflects changes in topography. This mode allows fast scanning and may

be used for friction analysis. It is not suitable for soft samples, which can be easily damaged. For soft samples, AFM tapping mode can be used. In tapping mode, the cantilever oscillates slightly below its resonance frequency. If the tip is close to the sample, the oscillation is reduced due to energy loss caused by the tip contacting the surface. The decrease in oscillation amplitude is the output signal and is used to identify surface topography.

In the non-contact mode, the oscillating tip is positioned ca. 50 – 150 Å above the sample surface. The tip detects attractive van der Waals forces present between the tip and the sample. Although those interactions are weaker than in tapping mode, they still can be detected by measuring the change in amplitude, phase, or frequency of the oscillating cantilever in response to force gradients from the sample. A disadvantage of non-contact mode is that ultrahigh vacuum conditions must be applied, making it unsuitable for *in situ* studies.

Peak Force Tapping™ (*Bruker*) AFM is a new operating mode, which allows the collection of mechanical properties data while imaging the sample. Opposite to a contact mode in Peak Force Tapping the probe is in contact with sample just for a short time, and opposite to tapping mode the maximum force on the tip is controlled. These modifications result in better protection of both tip and the sample from damaging during scan. A short contact time between the tip and the sample is sufficient to generate the force curve. Each curve is saved and can be analysed to obtain quantitative information (PF-Quantitative Nanomechanical Property Mapping) about different material properties such as adhesion, modulus, dissipation, and deformation.

Recent developments of combining AFM with spectroscopic techniques such as IR[117] and Raman[118] spectroscopy overcome the limitations of spatial confines originating from the diffraction limit of light, allowing to achieve simultaneous submicrometer resolution chemical images on the top of AFM micrographs and nanomechanical properties maps.

1.6.6 Molecular modelling

Materials Studio package is an integrated molecular modelling tool and it is available from Accelrys (San Diego, CA). It is used to build and display atomistic models and perform simulations on a variety of length and time scales. There are over twenty modules available for visualisation and calculation of various chemical and physical properties. Modules used in this thesis include:

Forcite is the forcefield-based molecular mechanics based on classical simulation theory. Bulk properties, such as diffusion coefficients or Young's moduli are averaged over a set of atomic nuclei configurations, causing the details of electronic motion to be lost in the averaging processes these properties. They can be extracted using Forcite without a need of using quantum mechanical techniques, which are usually computationally expensive. There are many potentials (or forcefields) and distribution generating techniques integrating the Newtonian (classical) equations of motion. The forcefield describes approximately the potential energy hypersurface on which the atomic nuclei move and it depends on the type of structure that is being investigated.

Morphology allows the prediction, study and visualisation of crystal morphologies based on the crystal structure using three methods: BFDH (Bravias-Friedel-Donnay-

Harker),[119] growth morphology and equilibrium morphology. This module does not take into account factors such as solvent, impurities or additives that can have a profound effect on crystal morphology. In the BFDH method the crystal morphology is modelled based on crystal lattice and symmetry to generate a list of possible growth faces based on the assumption that the centre-to-plane distance for a given plane is proportional to the inverse plane spacing $d_{hkl.}$ In the growth morphology method the crystal morphology is calculated based on the attachment energy E_{att} that is released on the attachment of a growth slice to a growing crystal face.[119] The growth rate is assumed to be proportional to the attachment energy, so the lowest attachment energy faces are the biggest and the slowest growing faces. In the equilibrium morphology method the crystal morphology is modelled based on a minimum of the surface free energy for a given volume and temperature.[120] It assumes that a surface is a perfect termination of the bulk and there is no surface relaxation.

DMol^3 allows modelling of the electronic structure and energetics of molecules, solids, and surfaces using density functional theory (DFT). In DFT techniques, the properties of a many-electron system can be determined by using the spatially dependent electron density. Density functional theory states that all ground-state properties are functionals of the charge density ρ. This module can be used to calculate specific chemical and physical properties including UV-Vis and Raman spectra in a solvent using COSMO (COnductor-like Screening Model),[121] which is a continuum solvation model that treats each solvent as a continuum with a permittivity ε surrounding the solute molecules outside of a molecular cavity. COSMO derives the polarisation charges of the continuum, caused by the polarity of the solute, from a scaled-conductor approximation.

Adsorption Locator is used to simulate an adsorption process of a chosen adsorbate on a surface with a fixed composition. Adsorption Locator will find low energy adsorption sites on both periodic and non-periodic substrates based on a Monte Carlo simulation of a substrate – adsorbate system. In Adsorption Locator, the output consists of a study table. This collects all lowest energy configurations found in the sampling obtained in the temperature cycles to allow the system to settle to a state of minimal energy. The process can be repeated in a number of cycles to allow the system to explore states of still lower energies.[122]

1.7 Olanzapine

Olanzapine (OZPN, $C_{17}H_{22}N_4S_1$, (2-methyl-4-(4-methyl-1- piperazinyl)-10H-thieno-[2,3-b] [1,5]benzodiazepine), Figure 11 a)[7,123,124] is a BCS class II (low solubility, high permeability)[125] benzodiazepine derivative used against the positive (hallucinations and delusions) and negative (social withdrawal) symptoms of schizophrenia, bipolar disorder and other psychoses.[126,127] It is manufactured under the trademark name Zyprexa® by Eli Lilly and Company. It appears as a light yellow (Form I) or white (Form II) crystalline solid, is practically insoluble in water (43 mg/L) and freely soluble in chloroform. The drug is stable at ambient temperature and humidity with melting point 190−195°C.[128] The olanzapine molecule is composed of a central seven-membered 1,5-diazepine ring (Figure 11 a, R2) fused with benzene (Figure 11 a, R1) a thiophene (Figure 11 a, R3), and an N-methyl-piperazine substituent ring (Figure 11 a, R4). A central diazepine ring adopts a distorted boat conformation. Benzene and thiophene rings are coplanar with dihedral angle between them 127.2°.[129] Olanzapine has a single hydrogen-bond donor, N1-H, and two good acceptors, the imine N2 and

piperazine N4, which are exposed in the crystal building blocks to near neighbour dimers.[123]

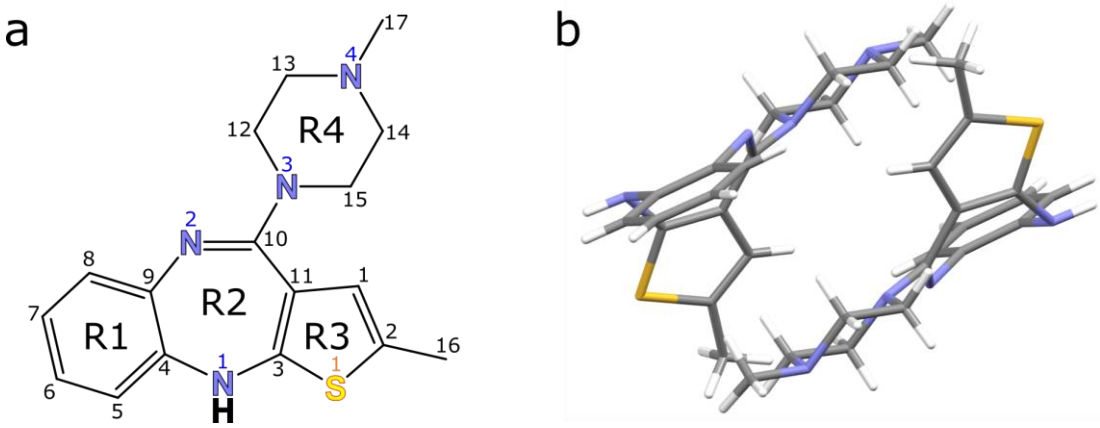

Figure 11 a) Molecular structure of OZPN, numbering of the atoms according to reference[7] , numbering of rings according to reference[130] b) Centrosymmetric (SC_0) dimer observed in most of the experimental crystal structures of olanzapine.

Whilst all neat and solvated solid forms of OZPN contain a centrosymmetric $(OZPN)_2$ dimer (SC_0) as a common structural building block (Figure 11 b),[7] the divalent cation in olanzapinium dipicrate, dimaleate, and dimaleate monofumaric acid, contain a novel structural motif, different from the SC_0 dimer.[128,131] SC_0 dimer is stabilized by three types of multiple C−H···π interactions: i) between piperazine C12 and thiophene C1-C2 fragment, ii) between piperazine C13 and thiophene C3-C11, iii) between piperazine C13, C14 and C17 the phenyl ring (multiple H· · ·π interactions).[129] The intradimer binding energy for olanzapine dimer computed at MP2 level of theory is -8.68 kcal/mol.[124] Since SC_0 dimers are observed in all crystal structures, it has been proposed to be the crystal building block from which other solid-state structures of olanzapine may be assembled.[62] Crystal structure prediction (CSP) calculations have indicated that OZPN structures without the dimeric motif are also thermodynamically feasible but they have yet to be observed experimentally.[7] To date, 60 distinct OZPN

forms have been identified, including three polymorphic forms (I, II, III), where form I is the most stable non-solvated form.[7] Form I of olanzapine, can be obtained from dry solvents including ethyl acetate, isopropyl acetate, butyl acetate, isobutyl acetate, diethyl ether, diisopropyl ether, toluene, and fluorotoluene.[7,123] Form II is usually concomitantly crystallised with traces of form III through vapour phase via sublimation or by desolvation of number of solvents such as methanol, dichloromethane, chloroform, trifluoroethanol solvates, and the 1-butanol solvate hydrate.[7] Neither of the pure form II or III has been obtained and the crystal structure of form III has not been determined so far. Based on CSP model A162[7] form II and form III exhibit the same 2-D crystal layers (SC_{24}), where every second layer in form III runs in the opposite direction. These structural similarities make the separation of two forms practically impossible. Olanzapinium dimaleate monofumaric acid is the first case of a ternary co-crystal of an active pharmaceutical ingredients (API) in the CSD database.[132]

In water the drug also forms three polymorphic dihydrates (B, D, E) and a disordered higher hydrate. In water slurries OZPN I converts to a kinetic form OZPN dihydrate B (OZPN DB) after few hours, while it transforms to OZPN dihydrate D, the thermodynamically stable hydrated crystal form of olanzapine, after slurrying in water for several days.[123] In high humidity environment the dihydrate formation pathway depends on the starting form and water activity.[133] Structural analysis showed that OZPN I shares 1−D structural similarity with olanzapine dihydrate B, dihydrate E and the higher hydrate and 2−D structural similarity to dihydrate D.[133] OZPN and OZPN hydrates exhibit low aqueous solubility and there is interest in studying the

mechanism of anhydrate to hydrate formation given the potential impact on performance and stability.[123]

2 Aims and Objectives

2.1 Aims

Design of various modelling tools for crystallisation is only reliable with an in-depth understanding of the fundamentals of crystal nucleation and growth. An increased understanding of these processes may allow a greater degree of control over the crystallisation outcomes, such as morphology, purity, or stability which are the key properties of pharmaceutical products. The overall aim of this thesis is to provide a better understanding of processes occurring during crystal nucleation, growth and solid-state transitions in aqueous solutions based on a pharmaceutical molecule, olanzapine. In the case of olanzapine, the impact of dissolution properties on drug product performance is critical. Therefore a particular emphasis is placed on non-classical nucleation processes taking place during the transition between anhydrous olanzapine to its hydrated forms. A range of advanced analytical techniques has been applied to characterise the nature of olanzapine prenucleation aggregates and to identify the key factors driving the nucleation pathways and polymorphic selection for olanzapine hydrates.

The work reported in this thesis also focuses on a crystal growth mechanism for olanzapine crystals. Since all crystal structure of olanzapine contain the SC_0 dimer as a building block, the dimer formation in various solvents was investigated and the crystal growth kinetics were studied in order to identify the growth mechanism and confirm the growth unit.

2.2 Objectives

- ✓ Apply optical and atomic force microscopy to study the effect of water activity, stirring and the role of OZPN I surface on the hydrate nucleation.
- ✓ Identify the key properties of the OZPN I surface that influence the selection of a polymorphic form of OZPN dihydrate by epitaxial match calculations, ledge geometry analysis and energy calculations
- ✓ Compare the observed nucleation mechanism with existing classical and non-classical theories.
- ✓ Monitor the properties of the dense clusters forming in OZPN solutions and deduce the cluster formation mechanism.
- ✓ Compare the cluster behaviours in aqueous solutions that contain varying quantities of ethanol with thermodynamic parameters of the solutions.
- ✓ Explore the role of the dense clusters in the mechanism of crystal growth of OZPN hydrate ethanoate.
- ✓ Explore the relationship between solution phase OZPN species and SC_0 found in OZPN crystal structures using NMR and Raman spectroscopies.
- ✓ Employ atomic force microscopy to identify of the growth mechanism and growth unit for OZPN hydrate ethanoate.

3 Materials and methods

3.1 Materials

All analytical grade solvents were purchased from Fisher Scientific, UK. NaCl (anhydrous, ≥99.5%) was purchased from Sigma Aldrich UK, and OZPN from Molekula Ltd., UK. It was confirmed as form I by X-ray powder diffraction (PXRD), was used without further purification.

3.2 Crystallisation

OZPN I, OZPN dihydrates and hydrate solvates were prepared according to the methods described by Reutzel-Edens *et. al.*[49] and Wawrzycka-Gorczyca.[124] Single crystals of OZPN I were obtained by dissolving ~200 mg of OZPN in 30 mL of ethyl acetate. The solution was stirred and heated to ensure complete dissolution of OZPN. The solution was then filtered through a 0.45 μm PTFE filter, transferred to 5 mL glass vials, sealed and kept at room temperature (RT) for 3−5 days without stirring. The resulting crystals were filtered under vacuum and washed with a 1/1 v/v ethyl acetate/hexane mixture to remove any surface deposited material. Crystals were dried on a filter paper in a desiccator over a silica drying agent. OZPN DB and OZPN DD for Raman measurements were obtained by stirring ~200 mg of OZPN I in 3 mL of water for 6 h and 8 days respectively. The presence of each dihydrate polymorph was then confirmed by PXRD.

Dihydrate ethanoate OZPN:EtOH:H_2O (2:1:2) for solubility studies were obtained by dissolving excess of OZPN I in 5 mL of 1/1 v/v EtOH/H_2O solution. The solution was heated up to 50°C and stirred overnight. The presence of the desired OZPN:EtOH:H_2O (2:1:2) was confirmed by PXRD. OZPN:EtOH:H_2O (2:1:2, P21/c) crystals for AFM analysis (70-200 μm in length) were grown by dissolving excess OZPN I in 5 mL of

1/1 v/v EtOH/H_2O solution. The solution was heat up to 50°C and stirred for around 15 minutes. Next, the solution was filtered through 0.22 μm PES filters to clean 5 mL vials with the coverslip scratched near the centre and placed in the vial beforehand. This way the crystals were immobilized on the coverslips without the need to use a glue. The coverslip with OZPN crystals was removed from the vials and rinsed with 1/1 v/v EtOH/H_2O to remove loosely attached crystals. The presence of the desired OZPN:EtOH:H_2O (2:1:2) was confirmed by PXRD and SC-XRD. Crystals prepared in that way were moved to the AFM instrument.

Experiments on OZPN I single crystals submerged in water. OZPN I single crystals (size between 1−1.5 mm) were attached to the end of a glass capillary with epoxy glue, and were oriented so that $\{100\}_{OZPNI}$ planes were exposed perpendicular to the capillary axis. The capillary was suspended in water so that when stirring was applied, the magnetic stirrer placed at the bottom of the vial was not in close contact with the crystal at the tip. Where specified as ‘stirring conditions’, the stirring rate was set as 100 rpm, otherwise no stirring was used. All experiments were performed at RT.

All the crystal structure parameters are summarized in Table 1.

Table 1 Unit cell parameters for all solid forms of OZPN used in this thesis

	OZPN I	OZPN DB OZPN:H_2O (1:2)	OZPN DD OZPN:H_2O (1:2)	OZPN HE OZPN:EtOH:H_2O (2:1:2)
Crystal system	Monoclinic	Monoclinic	Triclinic	Monoclinic
Space group	P21/c	P21/c	P-1	P21/c
a [Å]	10.38	9.87	9.93	15.13
b [Å]	14.83	12.72	10.10	12.43
c [Å]	10.56	14.39	10.51	20.20
α [°]	90	90	84.71	90.00
β [°]	100.62	92.97	62.67	92.72
γ [°]	90	90	71.18	90.00
V [$Å^3$]	1597.8	1802.8	884.1	3760
Z	4	4	2	4

3.3 Raman Spectroscopy

Solid-state Raman measurements. Raman spectra for OZPN crystals were collected using a Thermo Scientific™ DXR Raman microscope with a 532 nm (diode-pumped, solid state) laser excitation source and CCD equipped with a high precision X, Y, Z motorized stage in the shift region of 50−3400 cm^{-1} over 10 scans using a resolution of 1 cm^{-1} and an exposure time of 1 s.

Solution Raman measurements. The chloroform solutions were prepared by dissolving an adequate mass of OZPN I to achieve concentrations of 0.206 M, 0.169 M, 0.087 M, 0.023 M, 0.009 M in 3 mL of a solvent at RT to match the concentrations used for the

NMR study. Just before the analysis all solutions were filtered through 0.22 μm PTFE filter. All the solutions are assumed to be undersaturated against OZPN form I. Supersaturated EtOH/H_2O solutions (0.043 M and 0.032 M) were prepared dissolving the maximum amount of OZPN I in 3 mL EtOH/H_2O heated up to 40 °C and 35 °C and slowly cooled down to RT. The mass of the dissolved OZPN was then verified after the samples were completely dried and desolvated. Other three solutions were prepared at RT by dissolving adequate mass of OZPN I to achieve concentrations of 0.019 M, 0.012 M, and 0.005 M. These match the concentrations used for NMR study. All the solutions were filtered through a 0.22 μm PTFE filter and stayed clear for the time of the analysis. A Kaiser RXN2 Raman spectrometer with PhAT probe was used to monitor the solution non-invasively, in order to avoid any crystallisation on the probe The PhAT probe had the laser beam optically expanded to give a 3 mm spot size. This allows simultaneous analysis of a large sample area. A focal length of 12.5 mm. The beam was directed at the process through the top of the vial. The laser wavelength of 785 nm was produced by an Invictus diode laser operated at 350 mW at the source, with a CCD detector cooled to −40 °C by a Peltier cooling system. In advance of any measurements a verification (which measures relative peak intensity and peak position against known peaks from a cyclohexane standard) using the external sample compartment accessory for the instrument was performed. Raman spectra were recorded using iC Raman V4.1 software. Each Raman spectrum was recorded with eight scans and 30 s integration time. Solvent and glass spectra were collected and subtracted from each sample.

3.4 Nuclear magnetic resonance

The stock solutions were prepared by dissolving the maximum amount of OZPN I soluble at RT in deuterated solvents: chloroform, acetone, 1/1 v/v D_2O:EtOD. The mass of the dissolved OZPN was then verified after the samples were completely dried and desolvated. ^{1}HNMR spectra were prepared as a function of concentration. Stock solution for each solvent was diluted as follow: for chloroform-*d*: 0.80, 0.40, 0.10; for acetone-*d*: 0.90, 0.50, 0.20, 0.14; for EtOD/D_2O 0.95, 0.60, 0.25. All solutions were filtered through 0.22 μm PTFE filters and NMR spectra were collected up to 15 min after sample preparation using a Bruker Advance 3HD two-channel 500 MHz spectrometer. Sixteen scans were acquired for each sample at RT using a residual solvent peak as the reference. Spectra were analysed using Top Spin 3.5 (Bruker) and the shifts were quoted in ppm on the δ scale.

Optical Microscopy. Optical images were obtained using a Leica DM6000M optical microscope equipped with a motorized stage and Leica DFC495 camera. Images were analysed using LAS v.4.8 software (Leica).

3.5 X-ray powder diffraction

PXRD patterns were obtained using a Bruker AXS D8-Advance transmission diffractometer equipped with θ/θ geometry, primary monochromated radiation (Cu, λ = 1.54056 Å). Data were collected in the 2θ range of 4−35° with a 0.015° 2θ step and 1 s/step speed. Reference powder patterns were produced using the Mercury 3.6 (CCDC) software from single crystal data (CSD ref. code OZPN I: UNOGIN01, OZPN DD: AQOMAU, OZPN DB: AQOMAU03, dihydrate ethanoate OZPN:EtOH:H_2O (2:1:2): WEXQEW).

3.6 Single crystal face indexing

All crystal faces were indexed using a Bruker D8 Venture diffractometer equipped with a CCD detector and using graphite-monochromated Cu Kα radiation (λ=1.54056 Å) and an APEX-3 face indexing plug-in.

3.7 Atomic force microscopy

*AFM experiment in controlled relative humidity***.** OZPN I crystals were analysed at ambient (35 %) and higher (75 %) RH, with the latter achieved from ambient humidity using a saturated solution of NaCl and monitored throughout using a humidity sensor (Fisher Scientific). OZPN I crystals were mounted using double sided tape. Crystals were stored in a desiccator before analysis with no additional modification of crystal surfaces carried out before the measurements. AFM data were collected with a Dimension Icon AFM (Bruker) using PeakForce Tapping® mode at RT and a ScanAsyst Air probe (Bruker) with nominal spring constant k =0.4 N/m and a nominal tip radius of 2 nm.

AFM experiments in water. OZPN I crystals were mounted with epoxy glue to a cover slip and were placed in a crystallisation dish, which was submerged in 5 mL of deionized water with no applied solution flow. Images were acquired with a Dimension Icon AFM (Bruker) using PeakForce Tapping® mode at RT using a ScanAsyst Fluid probe (Bruker) with nominal spring constant k = 0.7 N/m and a nominal tip radius of 2 nm.

AFM growth studies in EtOH/H_2O. Washed crystals attached to a glass cover slip (*see Crystallisation of dihydrate ethanoate OZPN:EtOH:H_2O*) were imaged with AFM

FastScan (Bruker) using FastScan D SS probe (k=0.25 N/m and tip radius 1 nm) in OZPN supersaturated solutions with C_{OZPN} -C_e between 0.20 and 2.55 mM

AFM Image Processing. All AFM data was analysed using NanoScope Analysis 1.5 software (Bruker). Height images were corrected by a first order flattening function.

3.8 Simulations.

Morphology predictions. Crystal structures were geometrically optimized using the COMPASS force field in the Forcite module in Materials Studio 7.0 (Accelrys Software Inc.). The Quasi-Newton algorithm was used with convergence tolerance for energy of 2.0 x 10^{-5} kcal/mol, a force of 0.001 kcal/mol/Å, and the displacement of 1.0 x 10^{-5} Å. Growth morphology models of OZPN I, OZPN DD, OZPN DB were calculated using the Morphology Module (COMPASS force field with the Ewald summation method for electrostatic and van der Waals interactions with accuracy of 1.0 x 10^{-5} kcal/mol with a buffer width 0.5 Å). The BFDH morphology models were generated using the Morphology Module with minimum interplanar distance d_{hkl} = 0.8 Å.

Raman spectra calculations. OZPN monomer and dimer were directly copied from OZPN I crystal structure. The structures were geometrically optimized using DMol^3 module in Materials Studio 7.0 (Accelrys Software Inc.). The GGA PBE functional was used with convergence tolerance for energy of 1.0 x 10^{-4} H, a maximum force of 0.02 H/Å, maximum displacement of 5.0 x 10^{-2} Å, maximum iterations 50, maximum step size 0.3 Å, and 4.4 DN. The Raman spectra were generated based on frequency calculations using the COSMO[121] model for ethanol, water and chloroform solvents.

Adsorption locator calculations: Stepped OZPN HE surface were created from OZPN:EtOH:H_2O (2:1:2) crystal structure, CCDC code: WEXQEW. First, the unit cell was optimised with Forcite. The Quasi-Newton algorithm was used with convergence tolerance for energy of 2.0 x 10^{-5} kcal/mol, a force of 0.001 kcal/mol/Å, and the displacement of 1.0 x 10^{-5} Å. $(001)_{OZPNHE}$ surfaces were created by cleaving the OZPN HE unit cell to a fractional depth of 1 unit cell and constructing a 6 × 6 supercell. Rows of surface molecules were manually deleted to create steps with {110} orientations. A vacuum slab of 100 Å was inserted above the surface structure. The monomer and dimer structure were cut from the same crystal structure and optimised in the same way using Forcite and were chosen as adsorbate structures for the calculations. The COMPASS forcefield was used and the adsorbate structures were kept rigid. Five different adsorption configurations of monomer and dimer were investigated and the lowest energy configuration is reported. The binding energies calculated using the following equation: $U_{Ads} = U_{total} - (U_{surface} + U_{Adsorbate})$, where E_{total} is the total energy of the surface and adsorbate, $E_{surface}$ is the energy OZPN HE surface without the adsorbate, and $E_{adsorbate}$ is the energy of the adsorbate without the surface.

Epitaxial Matching Calculations. Epitaxial matching calculations were implemented using the GRACE (Geometric Real-space Analysis of Crystal Epitaxy)[52] software package version 4.1. Epitaxial scores (*E*) between $(100)_{OZPNI}$ and $(001)_{OZPNDD}$ or $(100)_{OZPNDB}$ were calculated by the summation of near coinciding lattice points between $(100)_{OZPNI}$ substrate and an overlayer of dihydrate as a function of the azimuthal angle between the two lattices[36] for various search areas. Gaussian

functions were used on lattice sites with the recommended[14] default parameters dc=0.5 Å, and d_0=0.3 Å.

3.9 Oblique illumination microscopy.

A Nanosight LM10-HS microscope (Nanosight Ltd) equipped with a green laser (532 nm) illuminating a 500 μm solution layer at an oblique angle was used to produce the trajectories of particles present in solution. The temperature was set T = 297.65 K. The viscosity of the solvent, η was determined from the dynamics of Fluoro-Max Dyed Red fluorescent polystyrene spheres, with diameter 1 μm, diffusing in the tested solutions.[50,52] The viscosities of all solutions employed are plotted in Figure 12. The concentration $N_{cluster}$ of clusters of different sizes was determined from the number n (Equation 9) in the monitored solution volume of V = 48,000 μm^3, [50, 52-53]

$$N_{cluster} = n/V \tag{9}$$

The volume fraction occupied by the cluster population was calculated based on equation 10:

$$\phi = 4\pi(\sum R_c^3 n_c)/3V \tag{10}$$

where V is the monitored solution volume. Each characterization of the cluster populations was repeated five times from distinct solution volumes within the same sample and averaged R, $N_{cluster}$, and ϕ over the five measurements; the error bars in all plots represent the standard deviation of this determination.

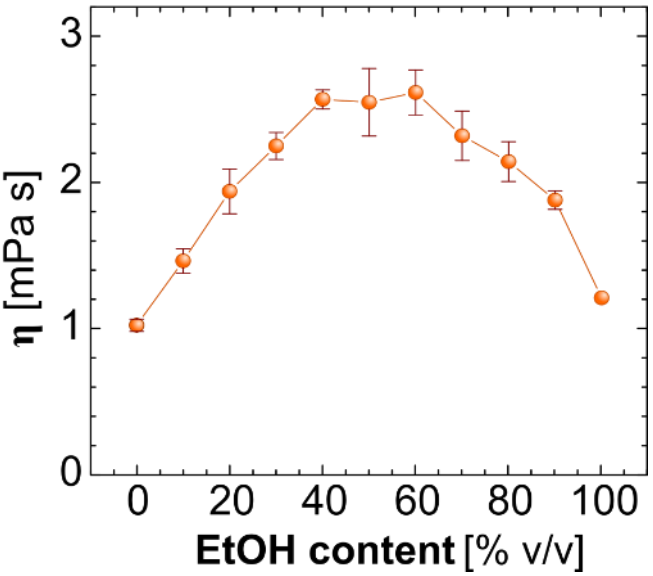

Figure 12 The viscosity of 5 mM solutions of OZPN in solvents with different EtOH concentrations. Error bars represent the standard deviation calculated from 500 particles (n=500).

3.10 Determination of the optical extinction coefficient of OZPN in water-ethanol solvents.

The ethanol concentration varied from 20 to 90 % v/v, with, correspondingly, 80 to 10 % water. Weighed OZPN amounts were dissolved in these solvents with concentrations between 0 and 40 μM. The completeness of dissolution was verified by the lack of scattered light using a UV-Vis spectrophotometerfrom ALV-GmbH, Langen, Germany. UV-Vis absorbance spectra were recorded in the range 200-800 nm using a 1 nm slit. (Figure 13). The wavelength of maximum absorbance varied between 252 nm, for 20% ethanol, to 270 nm, for 90% ethanol. The correlations between the optical density at the wavelength of maximum absorbance and the concentration were linear, Figure 13. The extinction coefficients ε for each ethanol concentration were determined from the respective slopes and are summarized in Table 2.

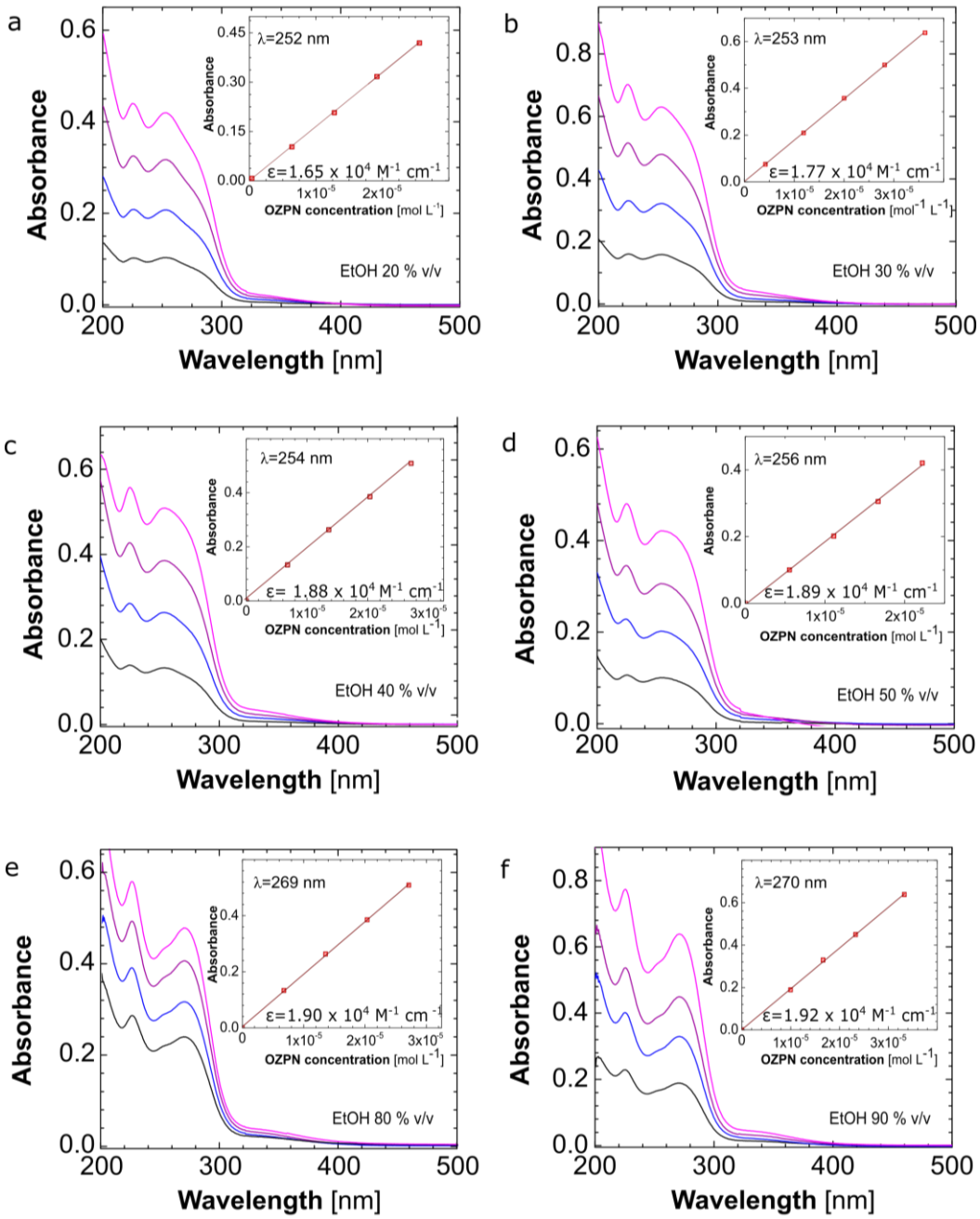

Figure 13 Determination of OZPN extinction coefficient ε in EtOH/H_2O mixtures. OZPN concentration was evaluated from the weight of dissolved powder. EtOH content in each solvent is indicated in the plots. UV-Vis spectra were employed to identify the wavelength λ of absorbance maximum. The correlation between the absorbance at this wavelength and the OZPN concentration, in the insets, was used to determine ε in each solvent.

Table 2 The extinction coefficient ε (± the standard error determined from the slop of the linear regression) of OZPN in solvents of different EtOH concentrations at the wavelength λ of maximum absorbance.

EtOH content [% v/v]	**ε [10^4 M^{-1} cm^{-1}]**	**λ [nm]**
20	1.645±0.001	252
30	1.765±0.005	253
40	1.878± 0.005	254
50	1.885±0.003	256
80	1.900±0.001	269
90	1.924± 0.001	270

3.11 Determination of the temperature dependence of the OZPN solubility in water-ethanol solvents.

Aliquots of OZPN:EtOH:H_2O (2:1:2) crystals were added to 5 mL solution with one of the tested compositions held in 20 mL capped glass vials. For experimental statistics, sets of three vials with identical compositions were stored at each of five temperatures: 277, 288, 297, 310, 318 K. A 300 μL aliquot was removed after a preset time from each vial, filtered through a 0.22 μm PES filter, and diluted with the respective solvent, and the concentration of dissolved OZPN was determined spectrophotometrically. This procedure was repeated until the concentrations in each vial reached a plateau, defined by three consecutive concentrations of consistent value, Figure 14. The final steady-state concentrations were averaged over the three samples for each temperature. The resulting mean was used as the solubility C_e.

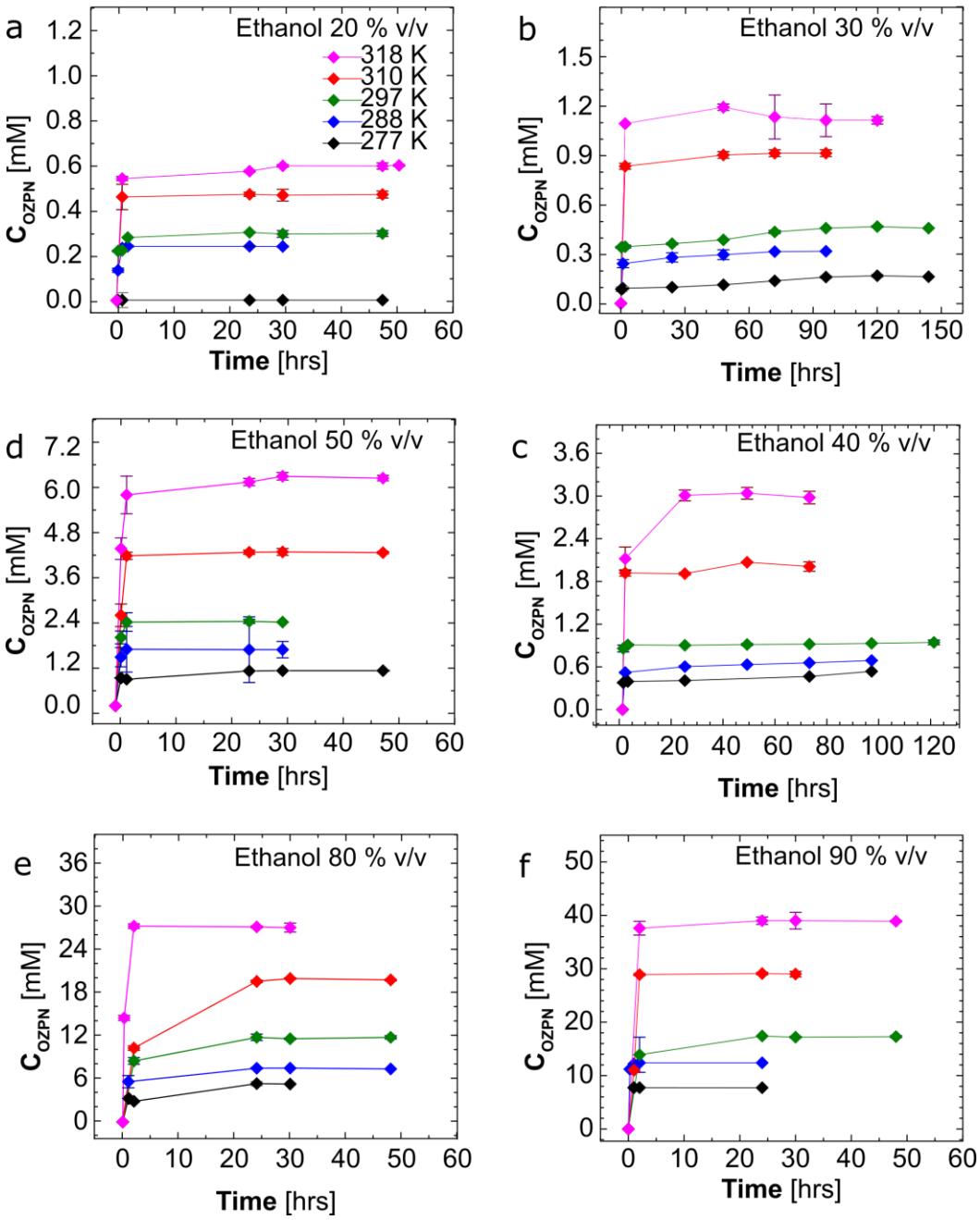

Figure 14 Determination of the OZPN solubility. Evolution of OZPN concentration at five different temperatures 277, 288, 297, 310, 318 K, for six different EtOH concentrations, a) 20 %, b) 30 %, c) 40 %, d) 50 %, e) 80 %, f) 90 % [v/v]. Error bars represent the standard deviation determined from three independent samples (n=3).

4 Direct observation of templated two-step nucleation during OZPN I to OZPN dihydrate transition

4.1 Introduction

Despite the widespread application of crystallisation in industrial processes crystal nucleation and growth remain poorly understood. These processes are difficult to monitor experimentally at the molecular level due to the short length and timescales typically involved. However considerable efforts continue to be devoted to understanding nucleation processes,[134] including the use of dynamic simulations.[82,135,136] Classical nucleation theory[24–28] is widely applied to describe crystal nucleation kinetics from solution, but cannot faithfully explain all observed phenomena. Recent studies have shown evidence of a two-step nucleation process in which the initial formation of clusters of a dense, disordered, liquid-like phase precedes the formation of an ordered solid nucleus inside the clusters.[29,30,37,38,78] The increasing evidence for two-step nucleation in organic, protein and inorganic systems suggests it may play a significant role in the formation of crystals under many different situations. A two-step nucleation mechanism was proposed during the heterogeneous nucleation of organic molecules on carbon nanohorns.[83] The impurity surface may have the ability to induce order within the dense pre-nucleation clusters and lower the surface free energy for nucleation as well as effectively template the resultant crystal form. There is therefore also considerable interest in the mechanisms controlling heterogeneous nucleation templating with surface topography,[11,12] lattice matching,[8,14,15,137] and molecular functionality[16–23] factors influencing the process.

4.2 Surface as a tool to control polymorphism

Understanding the mechanisms of ordering on the surfaces is fundamental to controlling the final properties of crystalline materials. Surfaces promoting

nucleation of a targeted polymorph are often chosen based on epitaxial interactions between a nucleation-promoting surface and crystallizing material. To date three major factors have been described as being responsible for successful polymorph selection on crystalline template- crystalline lattice matching, (two-dimensional epitaxy, 2−D),[8,14,15,137] molecular functionality of the substrate,[16–23] and substrate topography (Ledge-directed epitaxy-LDE).[11,12]

Crystallisation on ordered organic substrates involves the design of a substrate that resembles a particular crystal plane of the desired material. This strategy was presented as a robust method to target new polymorphs of pharmaceutical molecules (carbamazepine V, cyheptamide III templated on the surface of dihydrocarbamazepine II) that were not available through standard crystallisation approaches.[8,15] When targeted crystal polymorphs and crystalline substrate are isostructural, templating effect is not face specific (Figure 15 a).[8] However, in most cases only specific crystal faces of organic single crystals can be used to selectively nucleate targeted polymorphic forms.[13,14] Ward and co-workers designed a tool to predict the epitaxial match based on a lattice parameter of a substrate and overlayer - GRACE (Geometric Real-space Analysis of Crystal Epitaxy)[14] which is software that can be used to calculate the epitaxial match between lattices. GRACE does not show exact match between lattices, but rather 'epitaxy score, *E*', which takes into account both exact and near-coinciding points of two crystal lattices according to Equation 11:[14]

$$E = \frac{1}{n}\sum_i exp(-d_i^2/d_0^2)x100 \qquad (11)$$

where:

d_i- is the distance between the *i*th substrate lattice point and a nearby overlayer lattice point

d_0- is an adjustable parameter that governs the sensitivity of E to lattice mismatch

GRACE calculates the epitaxy score *E* based on given crystal cell parameters (crystal face, crystallographic vectors, angle between the vectors). Even though GRACE calculation does not take into account several kinetic factors, polymorph transformation, solvent effect, Oswald's rule of stages or relative growth rates of different planes it was able to successfully predict the observed epitaxial configuration of the (111) plane of NH_4I on the (001) plane of mica,[138] with $\theta = 0°$ and E = 46%, or orientation of ROY Yellow Needle polymorph on pimelic acid.[14] In case where intermolecular interactions have much stronger effects on the crystallising polymorph than the lattice registry, GRACE is not able to correctly predict the crystallisation outcomes (polymorph or orientation).[139]

The nucleation of particular polymorphic form can also occur on the surface of specific faces of the organic single crystal because shape-fitting contact with a well-defined ledge site and close-packed planes of a crystallising polymorph (Figure 15 b).[11] This approach was first used for crystalline substrates with ledges geometry defined by the crystal structure of the substrates[11] and was next applied to amorphous substrates where wider range of imprinted nanoscale geometrical features.[12] The nanoscale fabrication approach allows better control of matching the angle of the features present on the substrate and those existing between the faces of a specific polymorphs. This enables crystallisation of this polymorph on such

designed substrates. Additionally, specific intermolecular interactions between the substrate and crystallizing compound can be tailored by different substrate chemistry was proven to decrease nucleation induction time.[12]

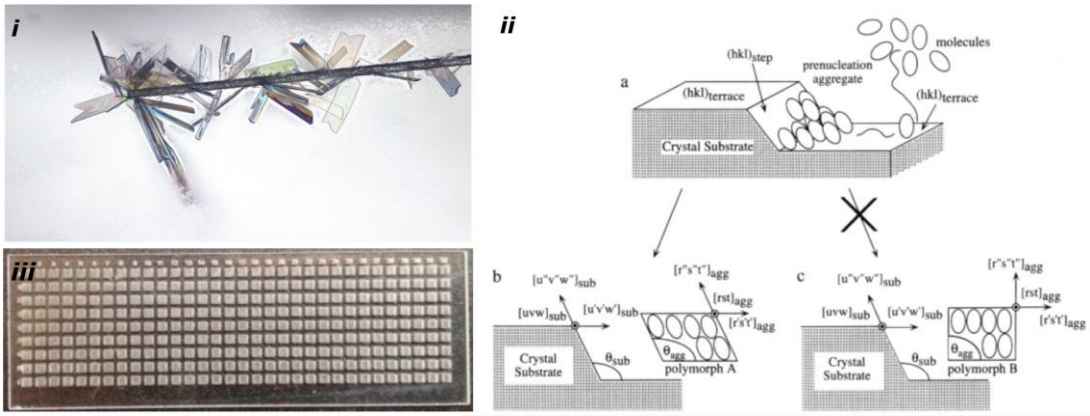

Figure 15 Examples of different properties of the substrate used to crystallize desired polymorphs, i) isostructural substrate dihydrocarbamazepine II for crystallisation of carbamazepine form V, copied from reference,[15] ii) concept of LDE, (a) molecules aggregate on the crystal terrace and diffuse to the ledge defined by the intersection of a $(hkl)_{step}$, and a $(hkl)_{plane}$ (b) showing the match between the ledge angle (θ_{sub}) of the substrate defined by crystallographic planes $[uvw]_{agg}$ and the angle between the crystal faces (θ_{agg}) of polymorph A, defined by crystallographic planes $[rst]_{agg}$. In contrast (c) showing mismatch between the ledge angle and the angle between crystal faces ($\theta_{sub} \neq \theta_{agg}$), copied from reference,[11] iii) plate with 288 polymer applied for polymer induced heteronucleation for polymorph screening.[23]

Adjusting surface chemistry is another strategy that can be effectively applied in control of polymorphic form due to subtle interactions between a substrate and the nucleating crystal. The molecular functionality of the substrate was proven to have much stronger templating effect than epitaxial match.[19,139] Using this approach a much wider range of substrates can be designed by adjusting the surface chemistry by e.g. using a wide range of polymers[20,21] or self-assembled monolayers.[22,140,141] Pfund and Matzger[23] presented a substrate containing 288 distinct polymers (Figure 15 c) for

polymorph screening of paracetamol, tolfenamic acid, ROY, and curcumin with a high yield in crystallising different polymorphic forms.

A better understanding of how surfaces can influence the structure of prenucleation aggregates could provide a basis to select or design surfaces that specifically template crystalline materials with desirable solid-state properties.[8,15]

4.3 Influence of water on olanzapine solid forms

Hydrate formation is of particular importance due to the widespread exposure of APIs to water, whether in solution or vapour form, since the incorporation of water molecules in the crystal lattice can have a dramatic effect on solubility and possibly the bioavailability of an API. OZPN and OZPN hydrates exhibit low aqueous solubility and there is interest in studying the mechanism of anhydrate to hydrate formation given the potential impact on performance and stability of OZPN shown in the study of Paisana *et. al.*[133]

In a stirred aqueous environment, both OZPN form I and form II first transform to kinetic OZPN DB (within 24 hours) and then to the more stable OZPN DD (after 5−7 days, Figure 16 A).[123,133] Structural analysis showed that OZPN I shares 1−D structural similarity with olanzapine OZPN DB, dihydrate E, and the higher hydrate and 2−D structural similarity to OZPN DD.[7,123] In the crystal structure of OZPN I and OZPN DD the dimers are aligned end-to-end and assemble directly on top of one another. In OZPN DD the water molecules occupy the sites between the SC_0 dimers and change the lattice from $P2_1/c$ (OZPN I) to P-1 (OZPN DD). In OZPN II and OZPN DB, the SC_0 dimers adopt a herringbone arrangement, and waters occupy the sites between the

SC_0 dimers. In all of the hydrates, the water molecules are held by two or three hydrogen-bonding interactions with the diazepine N2 and the piperazine N4 acceptors of olanzapine. The structural similarities between OZPN forms and corresponding dihydrates directed the different hydration outcomes under high relative humidity conditions.[133] In 93% relative humidity (RH), form II (containing form III as a phase impurity) converted to OZPN DB. In these conditions, OZPN I was directly converted into the OZPN DD without presence of other hydrates (Figure 16 B), and it is different from its behaviour when stirred in water.

In the case of OZPN, the impact of dissolution properties on drug product performance is critical. Conversion to a more stable, less soluble hydrated form could compromise dissolution. However, transformations limited to the surface of the crystal would be difficult to detect by conventional techniques, e.g. PXRD. For this reason, crystals are typically suspended in aqueous solutions, and stirring is used to drive transformations more or less to completion by continually refreshing the surface. It is generally assumed that transformations at extremely high humidity are the same but slower than those in stirred aqueous suspensions.

Hence, this chapter investigates the heterogeneous nucleation of OZPN hydrates on anhydrous OZPN I crystals in aqueous suspension and on exposure to humidity, using AFM. Following on previous work, this chapter investigates the effects of water activity, local mixing and structure on OZPN hydrate formation on the dominant face of OZPN I and provides evidence for two-step nucleation and surface templating. Extensive lattice matching is used to explain the formation of the disordered phase and templating effect of the $(100)_{OZPNI}$ face for OZPN DD.

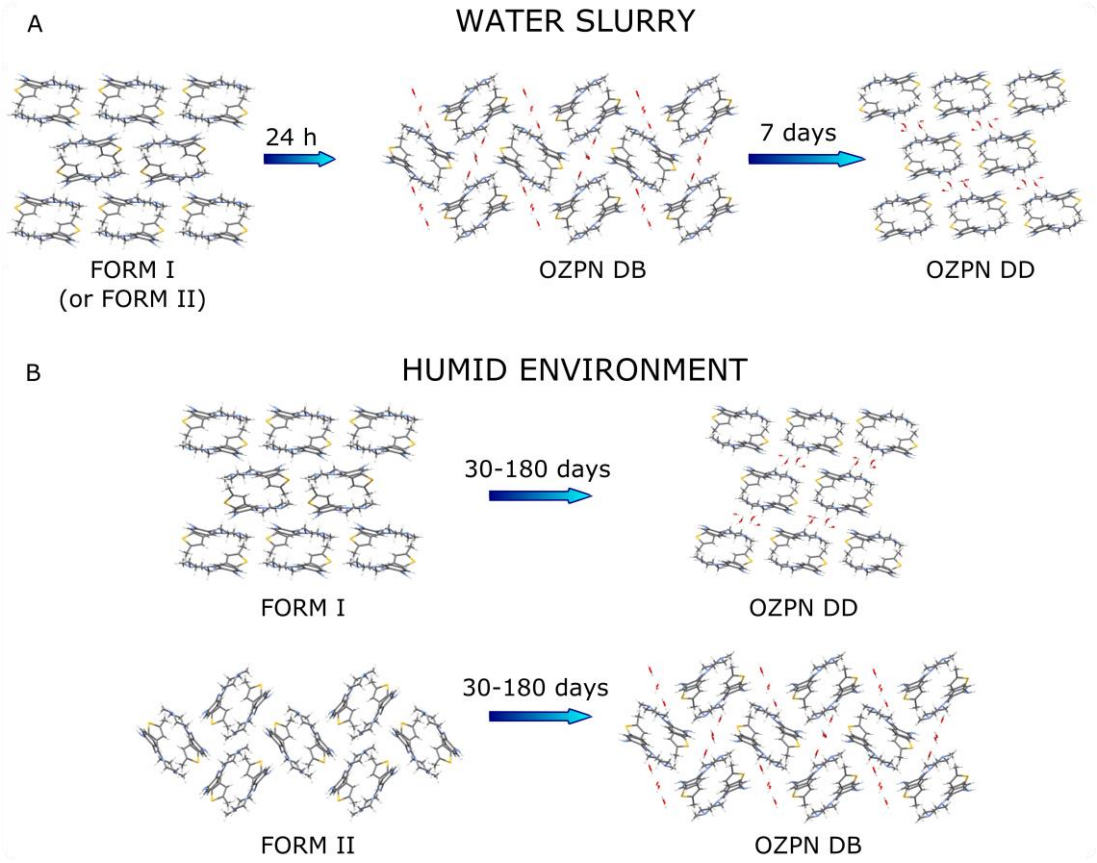

Figure 16 Transformation of OZPN in A) water where both OZPN I and OZPN II transform first to kinetic OZPN DB and later to thermodynamically stable OZPN DD, B) in 95% RH transition outcome depends on the starting form. OZPN I transforms to OZPN DD and OZPN form II transforms to OZPN DB.

4.4 Results and discussion

4.4.1 Characterization of OZPN I crystals

Form I OZPN is the most stable non-solvated crystal form and crystallizes in space group P21/c.[7,123] Single crystals can be obtained from several anhydrous solvents including ethyl acetate, isopropyl acetate, butyl acetate, isobutyl acetate, diethyl ether, diisopropyl ether, toluene, and fluorotoluene.[7] Crystals prepared by slow evaporation of ethyl acetate solution are light yellow in colour and show a rhombohedral morphology with large $\{100\}_{OZPNI}$ faces and other smaller faces (Figure 17 a, e, f, h). Analysis of the crystal structure of OZPN I shows that hydrogen bonds link the centrosymmetric SC_0 OZPN dimers[7] into 2−D layers parallel to $(100)_{OZPNI}$ (the orientation of the dimers on the $(100)_{OZPNI}$ face is shown in Figure 17 b). With only the aromatic and methyl groups of OZPN decorating the $(100)_{OZPNI}$ surface, this face has a decidedly hydrophobic character. The dominant $(100)_{OZPNI}$ face observed from recrystallized samples is also the largest face present in the BFDH predicted morphology (Figure 17 f), and is the face with the smallest attachment energy based on growth morphology calculation (Figure 17 g, Table 3).

Crystals (1 − 1.5 mm in size) grown from ethyl acetate solution were filtered, washed and dried (see Methods section). Optical microscopy shows well-formed facets (Figure 17 b) and nanoscale surface characterization by AFM reveals a detailed ledge and terrace structure on the $(100)_{OZPNI}$ surfaces (Figure 17 c). The steps show a high kink density from the conditions used in their growth and preparation (Figure 17 a), with a considerable number of them being $(020)_{OZPNI}$ steps comprising an $(100)_{OZPNI}$ terrace and $[001]_{OZPNI}$ ledges at an angle $\theta_{OZPNI} = 90°$ (Figure 17 c). The

measured step height (h_{100} = 10.12 ± 0.81 Å) correlates closely to the distance measured between (100) planes in an OZPN I crystal (d_{100} = 10.17 Å).

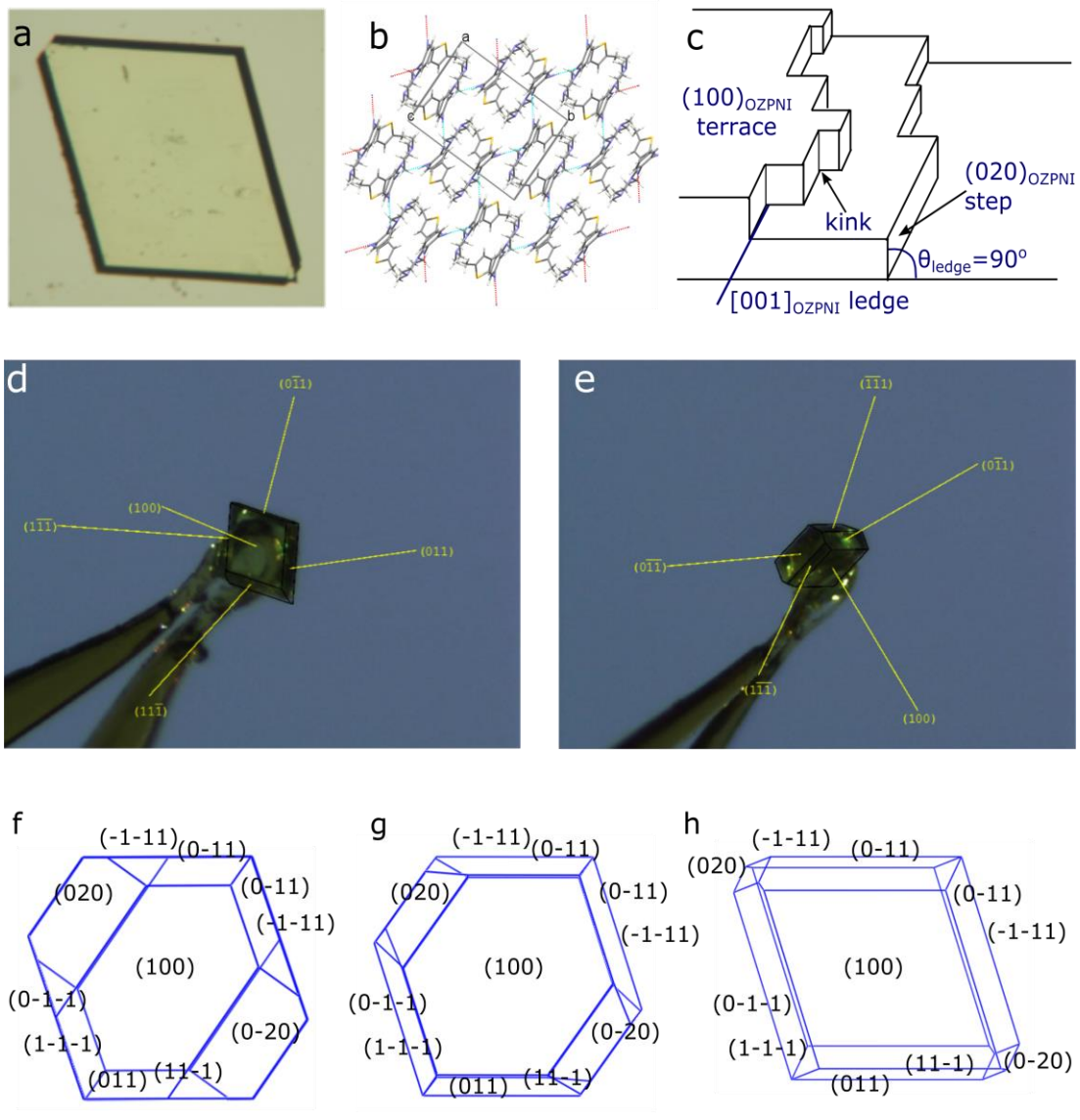

Figure 17 a) Single crystal of OZPN I obtained from slow evaporation of ethyl acetate solution, b) crystal structure of OZPN I (100)$_{OZPNI}$ face, showing SC_0 dimer pairs, c) schematic of (100)$_{OZPNI}$ crystal surface features observed using AFM (see Figure 18), d) and e) Crystal morphology of OZPN with face indices annotated f) BFDH morphology, g) growth morphology, h) observed morphology.

Table 3 Attachment energies per monomer for growth morphology model for OZPN I.

OZPN I (hkl)	**multiplicity**	**d_{hkl} [Å]**	**$E_{att\ (total)}$ [kJ/mol]**	**$E_{att\ (VdW)}$ [kJ/mol]**	**$E_{att(electrostatic)}$ [kJ/mol]**
{ 1 0 0}	2	10.175	-45.843	-44.544	-1.299
{ 0 1 1}	4	8.435	-60.012	-54.552	-5.460
{ 1 1 0}	4	8.333	-65.939	-61.402	-4.537
{ 0 2 0}	2	7.261	-70.167	-68.948	-1.218
{ 1 1 -1}	4	7.014	-70.639	-67.387	-3.252

4.4.2 Nanoscale surface transformation in a humidity-controlled environment

In situ AFM was used to investigate the mechanism of growth of OZPN DD on the surface of $(100)_{OZPNI}$. Imaging was carried out under both ambient (35% RH) and high humidity (75% RH) conditions for 150 min and 6 h respectively. Prior to the measurements, crystals were maintained over a silica desiccant to prevent initiation of hydrate formation and surfaces were analysed without additional cleaning. Upon exposure of the crystal to 35 % RH, multiple dome-shaped nanodroplets formed preferentially at high-energy kinks, steps or defect sites on the $(100)_{OZPNI}$ terrace (Figure 18 a−f). The initial diameter of the nanodroplets after 7 minutes (Figure 18 f) was 39.64 ± 2.37 nm (n = 30 droplets). Under these conditions growth of nanodroplets appears to be associated with slow dissolution of surrounding OZPN layers characterized by pit site formation on the crystal face and recession of step edges (Figure 18 d). It is assumed that the nanodroplets contain both OZPN and water molecules as a disordered dense phase. Over time, droplet coalescence is observed with those > 80 nm in diameter growing whereas smaller nanodroplets (< 60 nm in diameter) reduce in size and disappear over time. Within 150 min, droplets grew to an average diameter of 139.84 ± 31.42 nm (n= 30, Figure 18 f).

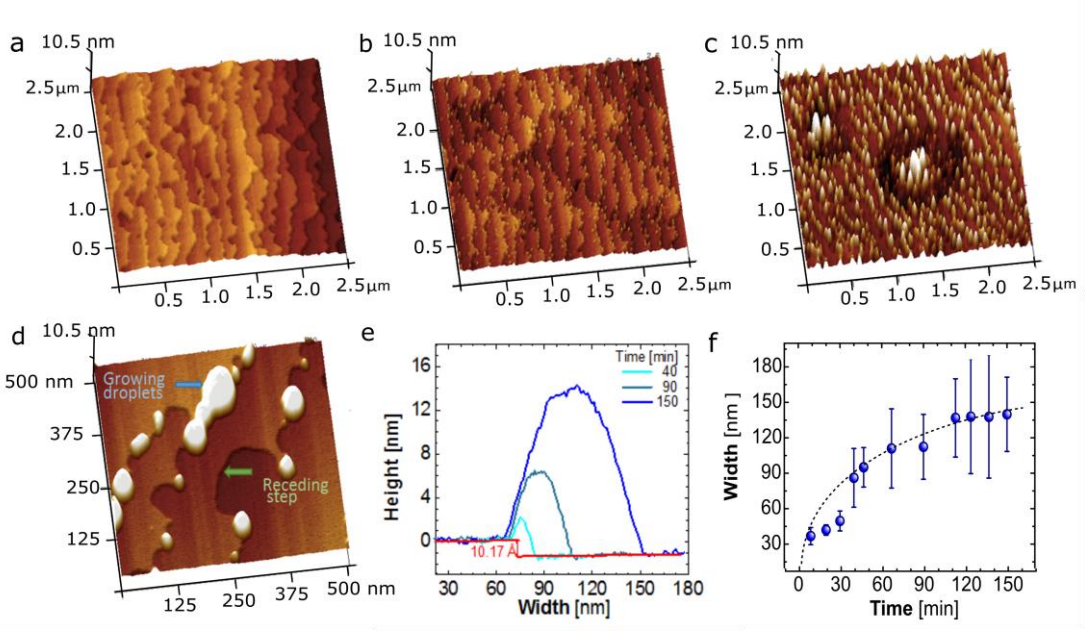

Figure 18 Growth of droplets on the surface of (100)$_{OZPNI}$ at 35 % RH, AFM micrographs of (100)$_{OZPNI}$ showing surface changes (scan size 2.5 µm, z scale bar 10 nm) at: a) 0 min, b) 30 min, c) 113 min, d) magnification of droplets after 113 min showing pit site form, (e) cross sections of the droplets during various times, and (f) growth of nanodroplets diameter over time, dash line is a guide to the eye. Each point is an average of n = 30 droplets

When OZPNI was subjected to 75 % RH (Figure 19) similar processes were observed, with coalescence of smaller droplets to form larger nanodroplets (102.77 ± 39.90 nm, n=30). When the crystal was held at 75 % RH for 14 days and re-analyzed, the (100)$_{OZPNI}$ surface was entirely covered with droplets (125.50 ± 23.27 nm, n=25) (Figure 19 e). Notably, no evidence of transformation of the nanodroplets to a new hydrated crystalline layer was observed. A previous report[133] showed OZPN I gained very little moisture below 53 % RH (< 0.1 % w/w), increasing only slightly after 180 days at 75 % RH (0.27 ± 0.07 % w/w), indicating that complete bulk transformation of OZPN I to dihydrate did not occur under these conditions even after prolonged exposure. Raman microspectroscopy of the OZPN I single crystal stored for 14 days in 75 % RH was unable to detect changes in the surface of OZPN I, most likely due to

the very low thickness of the nanodroplet layer. However, based on the consistent droplet morphology there is no evidence to suggest that a transformation of the nanodroplets to a hydrated crystalline phase had initiated at 75 % RH within 2 weeks.

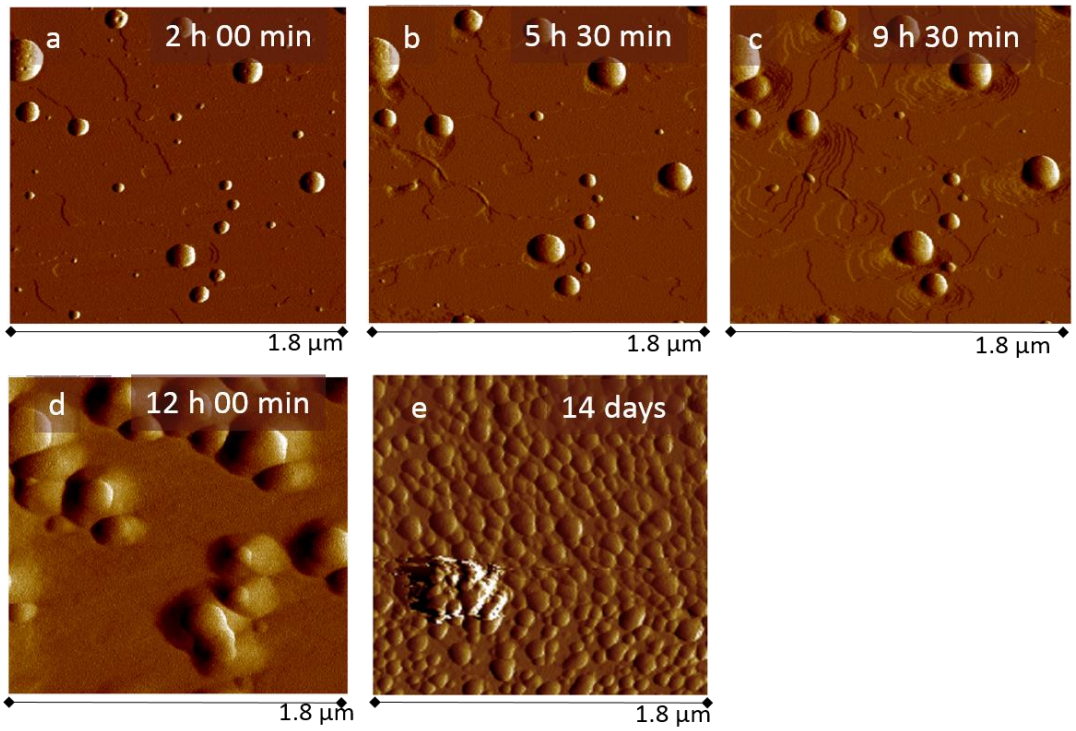

Figure 19 AFM micrographs of OZPN I (100) face under 75 % RH humidity conditions: a) droplets formed on the surface of (100)$_{OZPNI}$, b) and c) a clear demonstration of (dense) droplets growing by "feeding" from local ledges and multiple terraces, which presumably provides migrating SC_0 dimers, d) surface of (100)$_{OZPNI}$ covered with dense droplets after 12 h, e) surface of (100)$_{OZPNI}$ covered with dense droplets after 14 days.

4.4.3 *Effect of stirring on OZPN dihydrate formation at the $(100)_{OZPNI}$ solution interface*

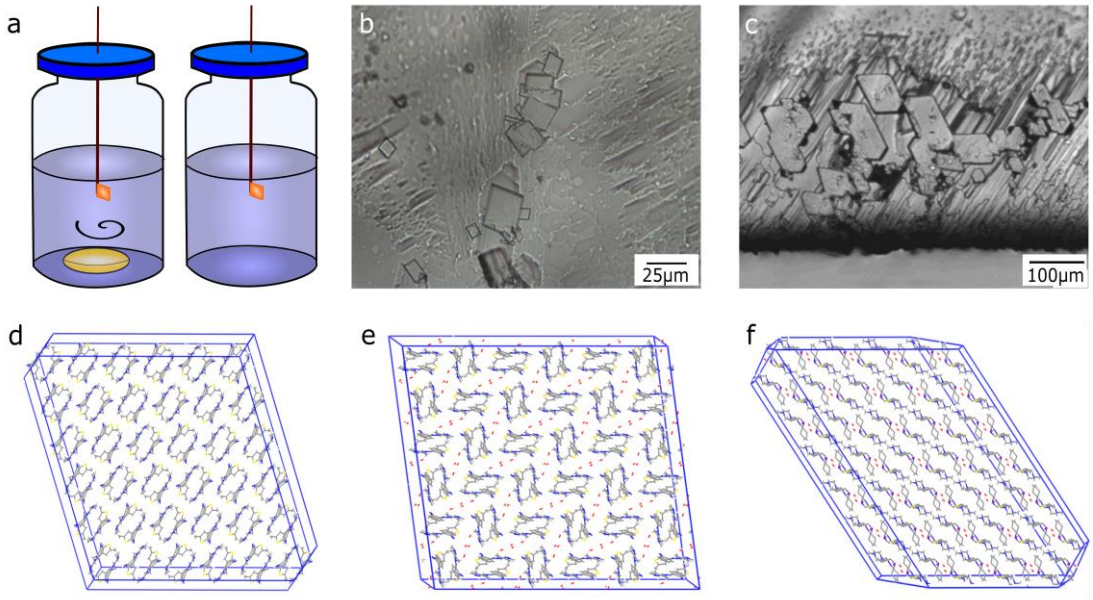

Figure 20 Effect of stirring on anhydrate to dihydrate transition. a) experimental set up: crystals attached to glass capillaries were placed in sealed vials and kept for 48 h in two different stirring conditions: gentle stirring (left; 100 rpm) and unstirred conditions (right). b) Optical image of the stirred $(100)_{OZPNI}$ surface of an OZPN I crystal with visible OZPN DB microcrystals after 6 h, c) image showing OZPN DD microcrystals on OZPN I after 48 h in unstirred solution. Observed crystal morphologies of d) OZPN I with dimeric motif on $(100)_{OZPNI}$ and e) OZPN DB microcrystallites and molecular arrangement on $(100)_{OZPNDB}$ face, f) OZPN DD microcrystallites and molecular arrangement on $(001)_{OZPNDD}$ face.

In a stirred aqueous suspension of crystals, OZPN I transforms first to the kinetic OZPN DB within hours, followed by transformation to the most stable OZPN DD within days.[123,133] To better understand these processes, immobilized single crystals of OZPN I were suspended in water in vials with either gentle stirring (100 rpm) or quiescent, unstirred conditions for 48 h (Figure 20 a). These different mixing environments for a suspended single crystal resulted in notable differences in the outcomes, and can be contrasted with conventional slurrying. In contrast to the OZPN humidity experiments, small plate-like crystallites ware observed on the

$(100)_{OZPNI}$ surface in water under all conditions. However, the orientation of the crystallites relative to the substrate crystal showed a dependence on stirring. When stirring was applied the microcrystallites did not exhibit significant preferential orientation relative to the substrate and were observed to be only loosely attached to the OZPN crystal surface (Figure 20 b). In contrast, microcrystallites grown under quiescent conditions were strongly bound to the $(100)_{OZPNI}$ crystal face and showed a significant and uniform degree of preferential orientation (Figure 20 c).

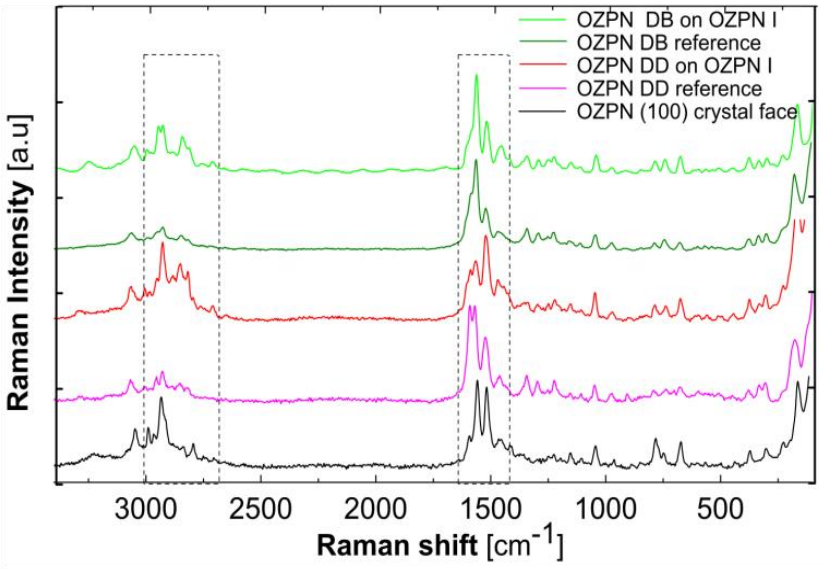

Figure 21 Raman spectra from the bottom: OZPN I, OZPN DD obtained from water slurry, OZPN DD microcrystals formed on OZPN I crystal, OZPN DB obtained from water slurry, OZPN DB crystal on surface of OZPN I with marked area of interest. Detailed description of the observed Raman spectra can be found in reference.[130]

Raman microspectroscopy was used to determine the solid-state form of the observed crystallites formed under both conditions and the resultant spectra were compared to reference spectra for OZPN DB, OZPN DD, and OZPN I (Figure 21). The loosely bound crystallites obtained under stirred conditions were identified as OZPN DB,

whilst the well-aligned, bound crystals produced under unstirred conditions were the thermodynamically stable dihydrate polymorph, OZPN DD.

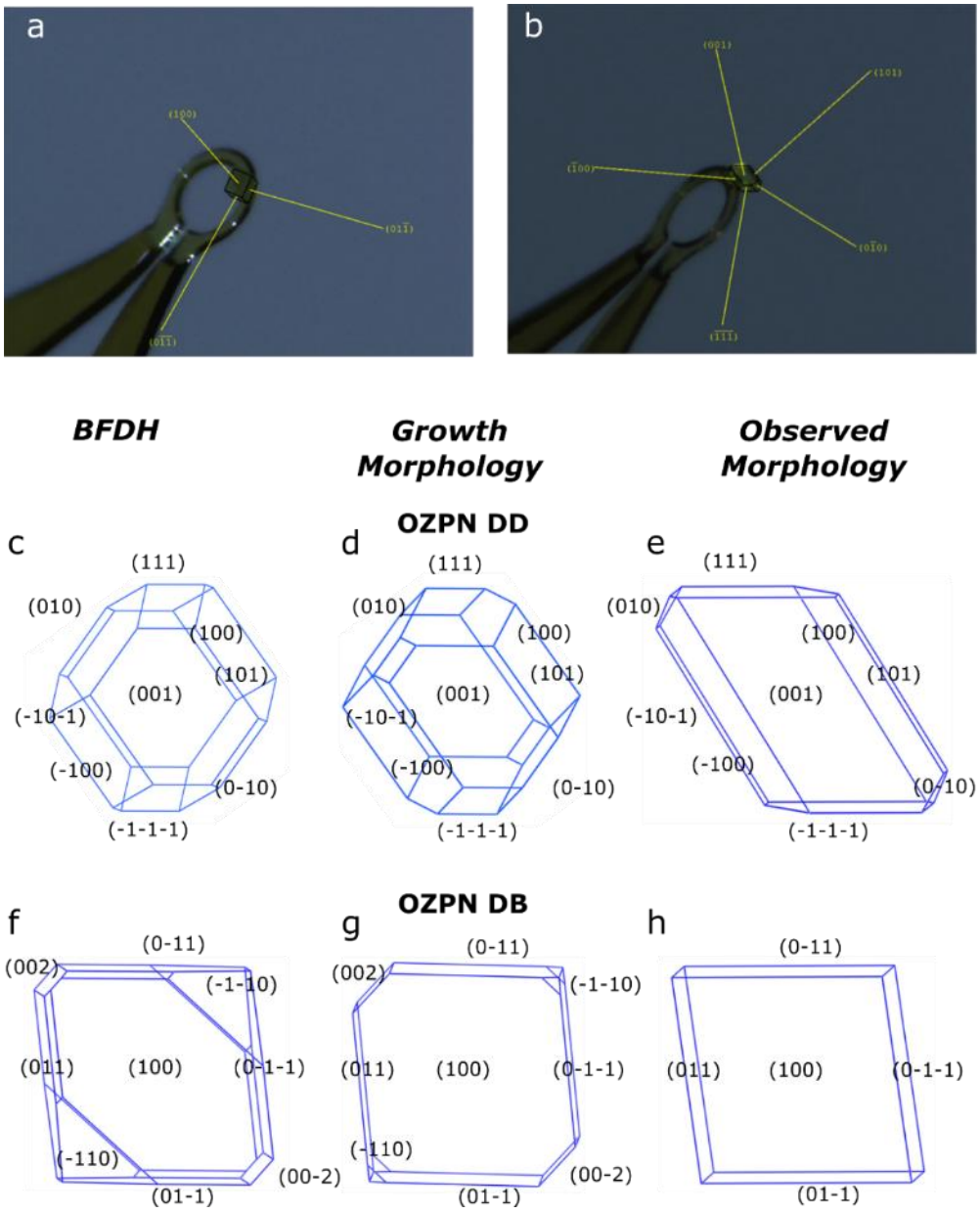

Figure 22 a) OZPN DB removed from the (100)$_{OZPNI}$ surface after 2 days in stirring conditions; b) OZPN DD removed from (100)$_{OZPNI}$ surface after 3 days of crystal being stored in quiescent water, c) BFDH morphology for OZPN DD, d) growth morphology for OZPN DD, e) observed morphology for OZPN DD, f) BFDH morphology for OZPN DB, g) growth morphology for OZPN DB, h) observed morphology for OZPN DB

Table 4 Attachment energies per monomer for growth morphology model for OZPN DD.

OZPN DD (hkl)	**multiplicity**	**d_{hkl} [Å]**	**$E_{att\ (total)}$ [kJ/mol]**	**$E_{att\ (VdW)}$ [kJ/mol]**	**$E_{att(electrostatic)}$ [kJ/mol]**
{ 0 1 0}	2	9.534	-36.066	-24.510	-11.556
{ 0 0 1}	2	9.319	-35.905	-17.348	-18.558
{ 1 0 1}	2	8.417	-33.200	-31.858	-1.342
{ 1 0 0}	2	8.364	-35.817	-27.687	-8.130
{ 1 1 0}	2	7.592	-36.563	-27.800	-8.764
{ 1 1 1}	2	7.319	-42.077	-28.065	-14.011
{ 0 1 -1}	2	6.898	-48.096	-33.671	-14.425

Table 5 Attachment energies per monomer for growth morphology model for OZPN DB

OZPN DB (hkl)	**multiplicity**	**d_{hkl} [Å]**	**$E_{att\ (total)}$ [kJ/mol]**	**$E_{att\ (VdW)}$ [kJ/mol]**	**$E_{att(electrostatic)}$ [kJ/mol]**
{ 1 0 0}	2	9.856	-44.644	-39.351	-5.294
{ 0 1 1}	4	9.523	-67.445	-38.563	-28.882
{ 1 1 0}	4	7.790	-85.965	-59.703	-26.262
{ 0 0 2}	2	7.183	-82.065	-68.288	-13.777

This was confirmed by single crystal X-ray analysis of crystallites carefully removed from the OZPN I samples surface. Face indexing of the dihydrate crystals (Figure 22 a, b) allowed the relative orientation of OZPN DD and OZPN DB on the surface of $(100)_{OZPNI}$ to be determined. Morphological analysis of the OZPN DD (Figure 22 c, d, e and Table 4) and OZPN DB (Figure 22 f, g, h and Table 5) crystals identified that crystals grew with $(001)_{OZPNDD}$ and $(100)_{OZPNDB}$ parallel to $(100)_{OZPNI}$ respectively.

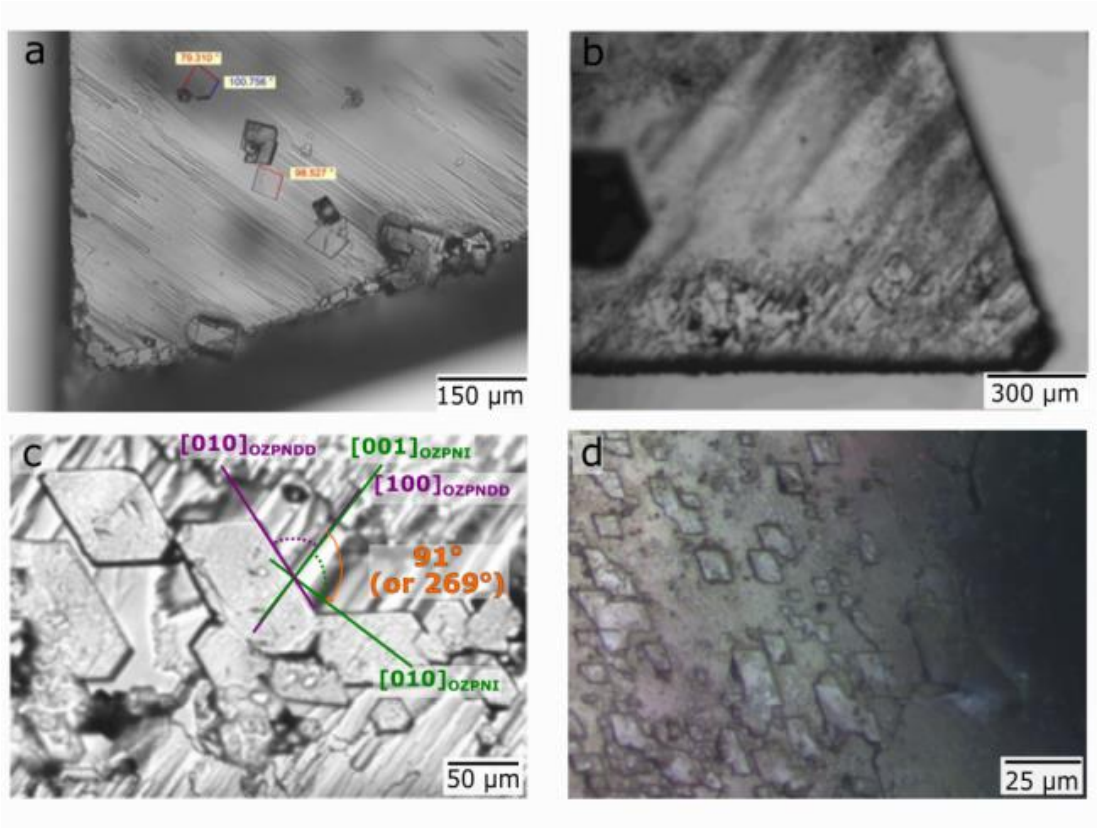

Figure 23 Orientation of OZPN DB and OZPN DD microcrystallites on OZPN I (100)$_{OZPNI}$: a) OZPN DB microcrystallites from stirred conditions show no preferred alignment with OZPN I axis; all OZPN DB microcrystallites show (100)$_{OZPNDB}$ as a dominant face; b) the consistent orientation of microcrystallites of OZPN DD on (100)$_{OZPNI}$, from unstirred experiments with (001)$_{OZPNDD}$ as a dominant face; c) relationship between the orientation of OZPN DD microcrystallites on OZPN I (100) face; d) OZPN DD microcrystallites obtained from AFM interval experiment, the orientation of the OZPN DD microcrystallites is the same as observed in unstirred conditions.

The OZPN DB microcrystallites are randomly oriented on the surface of OZPN I (Figure 23 a), and so loosely adhered that they could be readily removed for analysis. This appears to be the result of crystallites forming close to the OZPN I surface rather in direct contact and remaining in close proximity rather than being cleared from the surface by shear and deposited elsewhere in the reactor. In contrast, OZPN DD crystallites were surface bound and oriented with the $[100]_{OZPNDD}$ axis at 91° ± 2° with respect to $[010]_{OZPNI}$ direction (Figure 23 b, c, d).

4.4.4 AFM studies on $(100)_{OZPNI}$ in water.

The OZPN I to dihydrate transformation in water is clearly influenced by the applied stirring/shearing conditions. To further investigate this, several OZPN I crystals were suspended in water and the $(100)_{OZPNI}$ face was visualized by in situ AFM. Direct observation of the transforming surface using the scanning AFM probe can influence the surface.[142] Therefore, in addition to continuous in situ monitoring over 24 h, periodic monitoring of OZPN I samples stored under water was carried out to assess any influence of localized perturbations from the moving AFM probe.

Using longer scan intervals (2 h, 24 h, 24.5 h, 25 h and 48 h) the formation of the first nanodroplets occurred preferentially at the surface ledge together with local dissolution of OZPN (100) layers (Figure 24 a). The fact that these nanodroplets can be visualized in the aqueous environment, suggests that they are significantly denser than liquid water and are OZPN-rich. The initial nanodroplet-like structures (lateral average diameter after 2 hours: 34 ± 6 nm, n=30) are shown in (Figure 24 and Figure 25 a). There is also evidence of the dynamic nature of nanodroplets movement across the surface, with partial coalescence observed between neighbouring nanodroplets (two and many nanodroplets coalescing marked yellow arrow and with dashed circle respectively on Figure 24 and Figure 25 a). After 24 h, three scans with 30 min intervals were performed revealing a striking sequence of dynamic changes on the $(100)_{OZPNI}$ face. Coalescence of the nanodroplets progressively led to the formation of larger rounded rhombus-shaped features (Figure 25 c, with height 127 ± 34.20 nm and diameter 10.51 ± 0.60 μm). In the periodic monitoring experiments after 24 h, continued growth of the feature in all three dimensions was observed (587.25 ± 24.60 nm, 15.94 ± 0.16 μm).

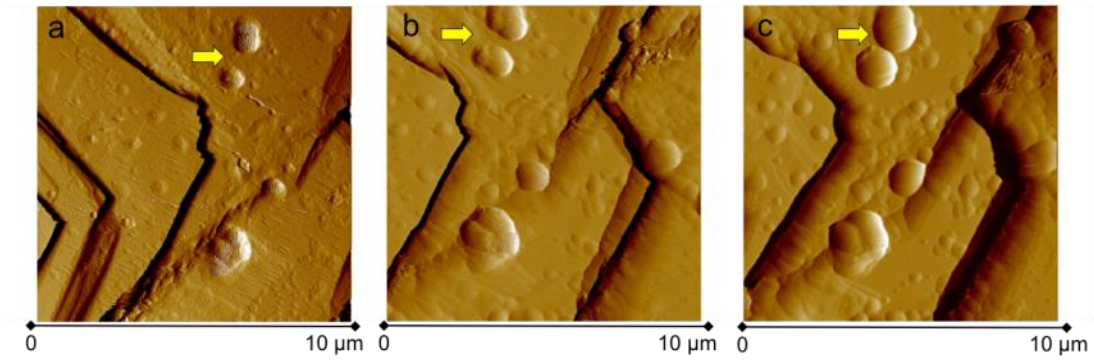

Figure 24 Example of aggregation of two dense droplets in water marked with yellow arrow. a) 0 min, b) 8 min, c) 16 min.

Whilst the nanodroplet retains significant curvature (cross section Figure 25c) some partial ordering is apparent (e.g. emergence of more linear droplet edges) that may be a result of close association of the nanodroplet to the underlying crystal lattice of $(100)_{OZPNI}$. Strikingly, after 48 h well-developed crystals are observed with the same morphology and orientation as described above for OZPN DD on the $(100)_{OZPNI}$ (Figure 25 d, Figure 23 d).

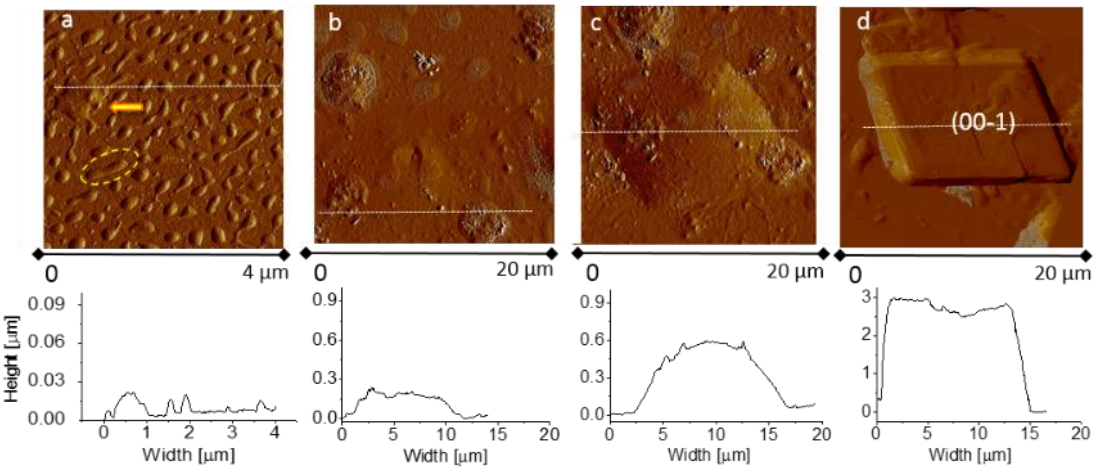

Figure 25 AFM micrographs with the corresponding cross section of height (area marked with dotted white line) of the surface of $(100)_{OZPNI}$ in water showing the evolution of size and ordered features after a) 2 h- visible droplets on the surface, droplet coalescence marked with yellow arrow and two droplets coalescing marked with dashed circle b) 24 h- coalescence of the droplets,

c) 25 h- large coalesced droplet rearranging into rhombus shape, d) 48 h- fully developed OZPN DD crystal.

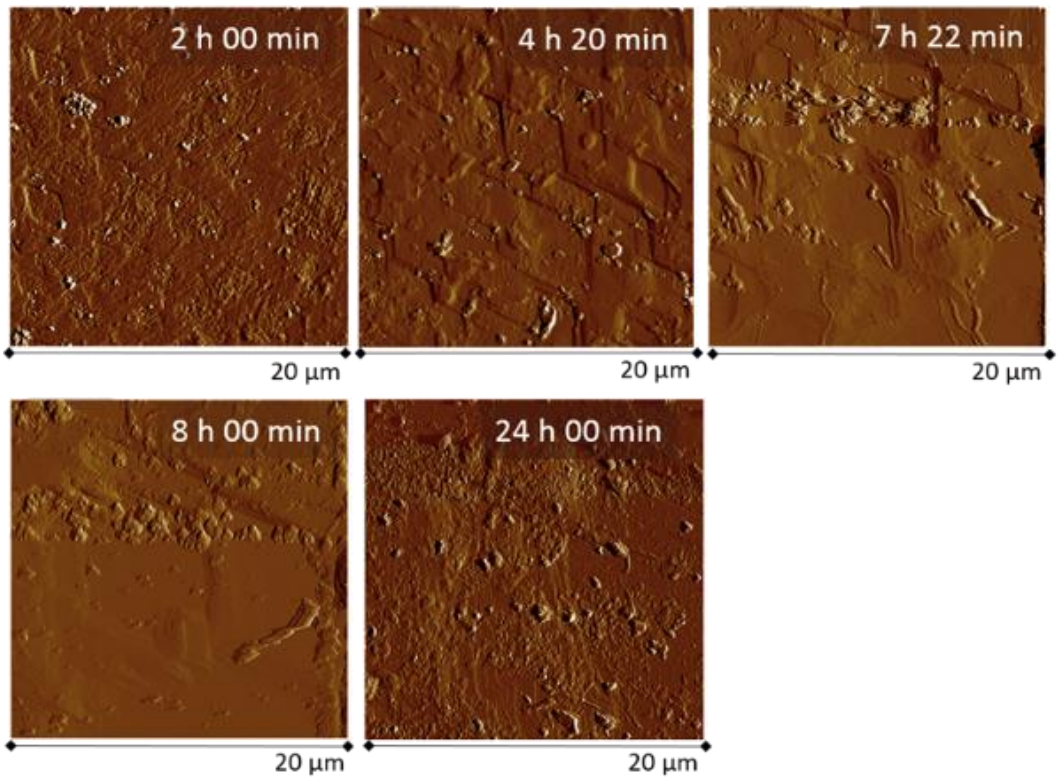

Figure 26 AFM micrographs of (100) face of OZPN I crystal in water scanned continuously for 24 h.

After 2 h of continuous scanning, the formation of nanodroplets was also observed. The nanodroplets could be easily moved, dragged or even torn off by lateral shear forces of the probe and continued development of larger features was not observed, possibly due to disruption of the process by the AFM tip (Figure 26). Whilst nanodroplets are still observed to coalesce, the continuous movement of the probe apparently interferes with the association of the nanodroplets with the $(100)_{OZPNI}$ face. Notably, no transformation to OZPN DD crystal was observed under continuous scanning. Thus the induction time for nucleation of crystals of OZPN DD from undisturbed nanodroplets, templated on the OZPN I surface, is significantly longer

than the time to form the droplets. Disruption of the droplets during this period inhibits templated nucleation of OZPN by the underlying surface from the droplets.

4.5 Discussion

4.5.1 Two-step nucleation process

When OZPN I is exposed to humidity (93 % RH and above) or to an aqueous environment it undergoes transformation to the more stable OZPN dihydrate.[7,123,133] The relatively slow rate of transformation of OZPN I to OZPN DD, with only partial surface transformation occurring after 48 h allows detailed study of the process using AFM. Building on a previous report,[133] the transformation of OZPN I in water is strongly dependent upon stirring, with quiescent conditions leading to direct growth of OZPN DD. Whilst the oriented growth of the resultant OZPN DD on $(100)_{OZPNI}$ is itself a striking finding, the details of the dynamic changes at the surface that precede the formation of these crystals is particularly unexpected. The formation, coalescence and growth of dense droplets preceding the nucleation of OZPN DD is not consistent with CNT and it is therefore proposed that OZPN DD nucleation on the surface of OZPN I is actually a two-step nucleation process (Figure 25). Formation of dense liquid domains in the range of several hundred nanometers leads to an unstable liquid phase that undergoes reorganization in a later stage into an ordered crystalline structure via a two-step nucleation process,[29,30,37,38,44,45,78] with the fundamental assumption of an increase in density prior to and separated from the development of crystallinity.[30]

AFM studies show that, when OZPN I single crystals are exposed to humidity (35 % RH), numerous nanodroplets form at high-energy kinks, ledges or defects on $(100)_{OZPNI}$ terraces (Figure 27 A). Condensation of water on the surface, presumably

leads to localized dissolution of OZPN and nanodroplets increase in size by short-range molecular diffusion of OZPN molecules from adjacent crystal ledges, further water condensation and coalescence (Figure 27 B). However, the transformation from OZPN I to the hydrated form under this condition (35 % RH) was not observed, consistent with reports that it can only occur to a significant extent at above 93 % RH.[133]

When suspended in aqueous solution, the aqueous OZPN nanodroplets can be visualised by AFM as a separate, solute rich dense liquid phase. Under quiescent conditions, the nanodroplets coalesce and transform to a mesoscopic feature with a rhombus shape (Figure 25 c, and Figure 27 C). The shape of this feature is intriguing, evidently develops from the coalescence of smaller droplets and whilst no well-developed crystal facets are observed, the edges of the feature are approximately straight. The lateral profile of the observed mesodroplet (Figure 25 c, bottom) suggests that the nucleation process starts at the interface between $(100)_{OZPNI}$ and the droplet, and appears to be strongly influenced by the crystal alignment of that face. The apparent evolution of ordering in the droplet suggests that nucleation occurs at the base of the drop in contact with the $(100)_{OZPNI}$ face and crystal growth progresses until the OZPN supersaturation has been consumed to form OZPN DD. The preferred orientation of OZPN DD microcrystallites on the OZPN substrate suggests that $(100)_{OZPNI}$ plays a significant role in this process, templating the nucleation of OZPN DD from aggregated droplets (Figure 27 D).

Based on the unexpected formation of OZPN DB and DD microcrystals under stirred and unstirred conditions respectively (Figure 20), it can be concluded that the nanodroplets do not exhibit encoded structural information corresponding to either

specific crystalline polymorph.[38] Recent molecular simulations by Anwar et. al.[136] showed that in situations where a crystal surface is present in a supersaturated solution, weakly bound spherical clusters of solute molecules immediately nucleate, when these clusters are in close contact with the surface. Nucleated clusters could be easily removed from the surface by agitation, leaving the surface able to seed further secondary nucleation. Taking into consideration the soft properties of nanodroplets observed in aqueous OZPN, and the relative ease by which they can be relocated (such as by a moving AFM probe), it is proposed that when exposed to shear through stirring, droplets are removed from the templating $(100)_{OZPNI}$ surface (Figure 27 E). These solute rich droplets then coalesce and nucleate the kinetically-favoured form OZPN DB in free solution (Figure 27 F and G), with no direct influence of $(100)_{OZPNI}$. Further work to confirm the presence of OZPN rich droplets in water solution, for example using light scattering techniques, is a subject of a next chapter. Nevertheless, similar behaviour has been reported for the dependence of the magnitude of the contact force used during microattrition on the polymorphic outcome of glycine: α–glycine was found to be more likely to nucleate at low forces due to removal of glycine rich clusters from the γ-glycine crystals, while using high forces led to secondary nucleation of the γ form.[143] Complete transformation of the OZPN I substrate crystal to OZPN DD was not observed, during these experiments due to slow transformation kinetics combined with reduced driving force from partial surface coverage.

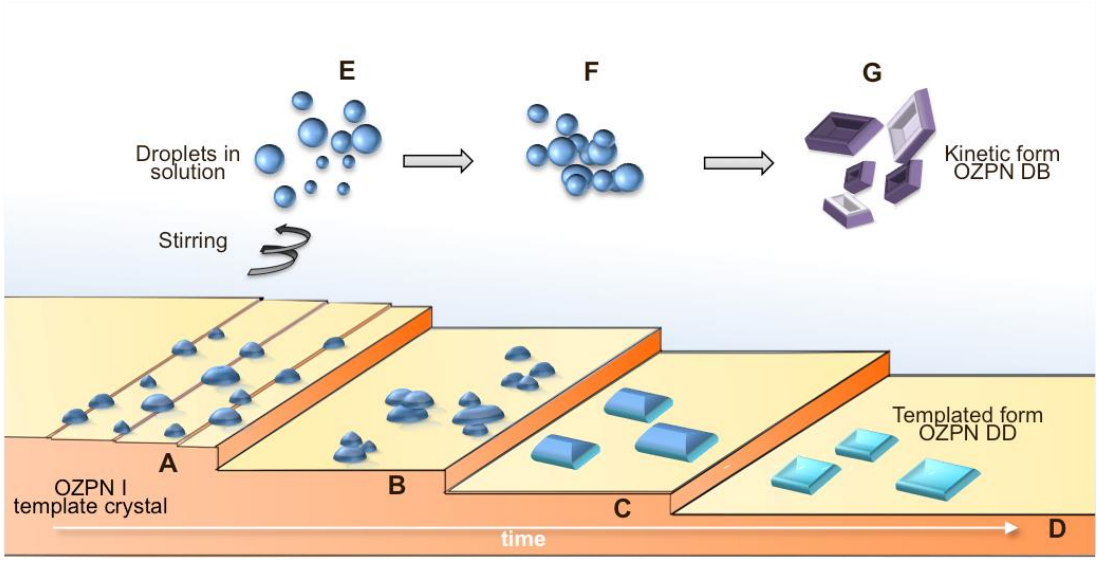

Figure 27 Schematic of the proposed nucleation process of OZPN DD on the surface of an OZPN I crystal and OZPN DB in solution. Large steps (labelled A−D) represent major stages. In unstirred conditions nucleation follows A → D path resulting in formation of templated OZPN DD where A) shows formation of the droplets at steps, B) coalescence of the droplets, C) formation of mesoscale droplets with emergence of crystalline features and D) fully developed OZPN DD crystal aligned on (100)$_{OZPNI}$. Under stirred conditions, nucleation follows path E → G where E) static layer around the crystal is disturbed and droplets transfer into bulk solution, F) droplets coalesce in solution and G) the kinetic form (OZPN DB) crystals nucleate and grow in free solution.

4.5.2 Role of OZPN I as a template

Heterogeneous nucleation is widespread, where with containers, stirrers, impurities, particles/dust act as the surface enhancing nucleation rates and possibly influencing resultant crystalline properties of the resultant materials. It is known that nucleation of a crystal is favourable on surfaces, as the interface promotes nucleation by lowering the nucleation free energy barrier.[144] Indeed, well-chosen crystal surfaces can work as templates to crystallize novel polymorphs of organic molecules.[8,15] To date, three major factors have been described as responsible for successful polymorph selection on crystalline templates: lattice matching (2−D epitaxy),[8,14,15,137] molecular

functionality of the substrate,[16–23] and the substrate topography (ledge-directed epitaxy or LDE).[11,12]

4.5.3 Geometric real-space analysis of crystal epitaxy - GRACE calculations

The highly consistent orientation of OZPN DD microcrystals on OZPN I suggests a significant influence of the underlying OZPN I crystal structure on OZPN DD nucleation and growth under quiescent conditions. The strong dependence of the orientation between the substrate crystal and grown crystals is generally presumed to be controlled by an epitaxial mechanism. However GRACE analysis[11,14,139] shows that there is no long range epitaxial match between the lattices of either dihydrate and the OZPN (100) face. Geometric real-space analysis of crystal epitaxy (GRACE)[10,13] was used to examine underlying epitaxy between the $(100)_{OZPNI}$ face and the dominant faces of the two OZPN dihydrates which have been observed growing on $(100)_{OZPNI}$, using experimental crystal structures Gaussian functions were used on lattice sites with the recommended[10,13] default parameters d_c=0.5 Å, and d_0=0.3 Å. For each face, GRACE analysis was carried out for a series of increasingly larger square search area, with the length of the square side given in Table 3. Based on GRACE calculations main peak at θ=10° with *E*=2.42 and another lower intensity peak at 50° with *E*=1.5 (Figure 28, Table 6). Either of measured angles do not correspond to observed angle between $[110]_{OZPNDD}$ and $[001]_{OZPNI}$ vectors. Considering the score for a perfect epitaxial matching is 100, it is clear from Table 3 that epitaxial matching is rather poor for either OZPN dihydrate face on the $(100)_{OZPNI}$ face. Roughly speaking, an epitaxial score shows how many of 100 lattice points of the overlayer match those on the substrate. Thus a score of well less than 10 for even the smallest nanocrystal shows very little matching, which decreases rapidly with size of overlayer.

Table 6 GRACE search between OZPN I (100) face and (001)$_{OZPNDD}$ and (100)$_{OZPNDB}$

Epitaxy Score	100x100	200x200	400x400	600x600
OZPN DD (001)	3.88	3.12	2.59	2.42
OZPN DB (100)	4.93	3.25	0.99	0.51

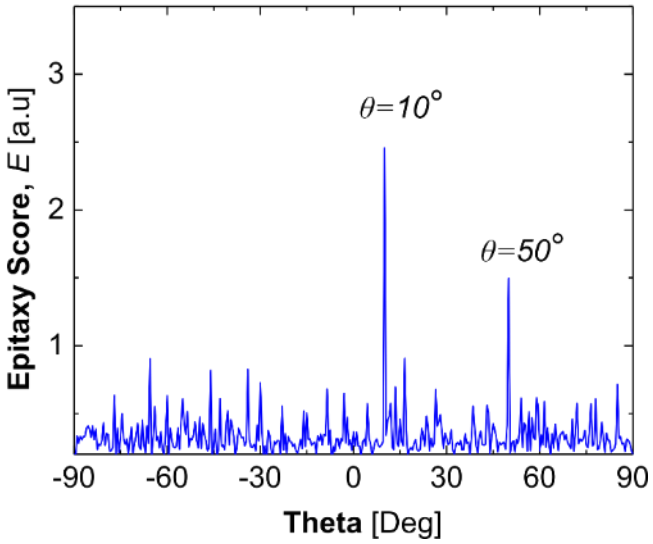

Figure 28 Epitaxy score between (100)$_{OZPNI}$ plane and (001)$_{OZPNDD}$ for search area 600x600 Å.

The overall conclusion is that epitaxy between dominant faces of the two dihydrates with (100)$_{OZPNI}$ are similarly poor over large areas and cannot explain why OZPN DD nanocrystals with (001)$_{OZPNDD}$ face were observed to nucleate from (100)$_{OZPNI}$ face.

4.5.4 Ledge Directed Epitaxy (LDE)

Ledge-directed epitaxy, or LDE[11] requires the misfit between the ledge angle and the cell angle to be < 1°. The [001]$_{OZPNI}$ ledge makes a 90° angle with the (100)$_{OZPNI}$ face, and OZPN DD is triclinic, with a largest angle of 85° (Figure 29 a). Although OZPN DB crystals possess dihedral angle θ=90º (Figure 29 b), random orientation of microcrystallites on (100)$_{OZPNI}$ surface indicates that their nucleation and growth are not templated in any way by the underlying substrate.

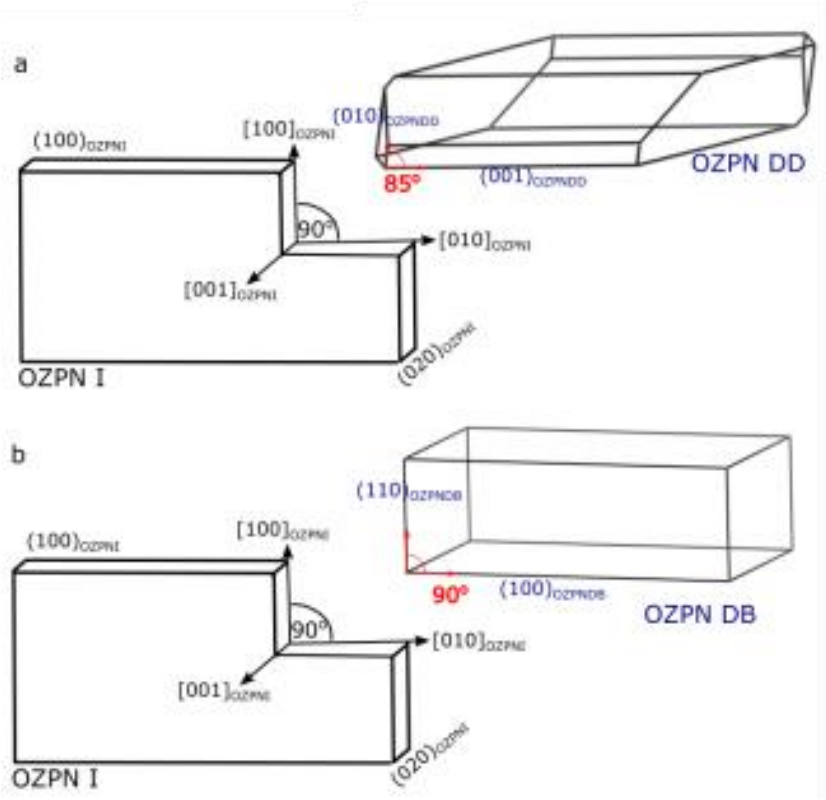

Figure 29 Examination of possible LDE of OZPN dihydrates on $[001]_{OPZNI}$ ledge. The $[001]_{OZPNI}$ ledge of OZPN I crystal has a ledge angle of $\theta_{ledge}=90^{o}$. LDE epitaxy postulates that nucleation is favoured when a nucleating polymorph possesses two planes that form a dihedral angle matching the substrate ledge: a) showing OZPN DD dihedral angle $\theta=85^{o}$ composed of $(010)_{OZPNDD}$ and $(001)_{OZPNDD}$ face; b) OZPN DB crystals with a dihedral angle $\theta=90^{o}$.

Lattice matching and surface topography did not show sufficiently strong agreement between the substrate and the emergent form to suggest that these were significant mechanisms for OZPN.

4.5.5 The influence of OZPN I on the growth of OZPN DD and OZPN DB

All calculations included in this subchapter has been performed using ORIENT[145] *by Dr Rui Guo and Prof. Sally Price form UCL and are a part of a publication: Warzecha, M.; Guo, R.; Bhardwaj, R. M.; Reutzel-Edens, S. M.; Price, S. L.; Lamprou, D.; Florence, A. J. Direct Observation of Templated Two-Step Nucleation Mechanism during Olanzapine Hydration. Cryst. Growth Des.* ***2017****, 17 (12), 6382–6393 and there are included since in this thesis as a essential part of the discussion and conclusions.*

To investigate why OZPN DD microcrystallites were observed with their $(001)_{OZPNDD}$ face firmly attached to the $(100)_{OZPNI}$ face, in contrast to the loosely attached $(100)_{OZPNDB}$, nanocrystal models of both faces were constructed. These represent a small nucleating cluster that is large enough to establish the distinct hydrate crystal structures. The two nanocrystal constructs and the OZPN I surface are shown in Figure 30. This reveals that the $(100)_{OZPNI}$ face is hydrophobic and has a complex local topography, corrugated with large oval shaped peaks and pits. On the other hand different functional groups are exposed on the two dihydrate faces, presenting distinct chemical environments to the $(100)_{OZPNI}$ substrate face. The hydrophobic surface chemistry is also consistent with the observed resistance of OZPN I to wetting.

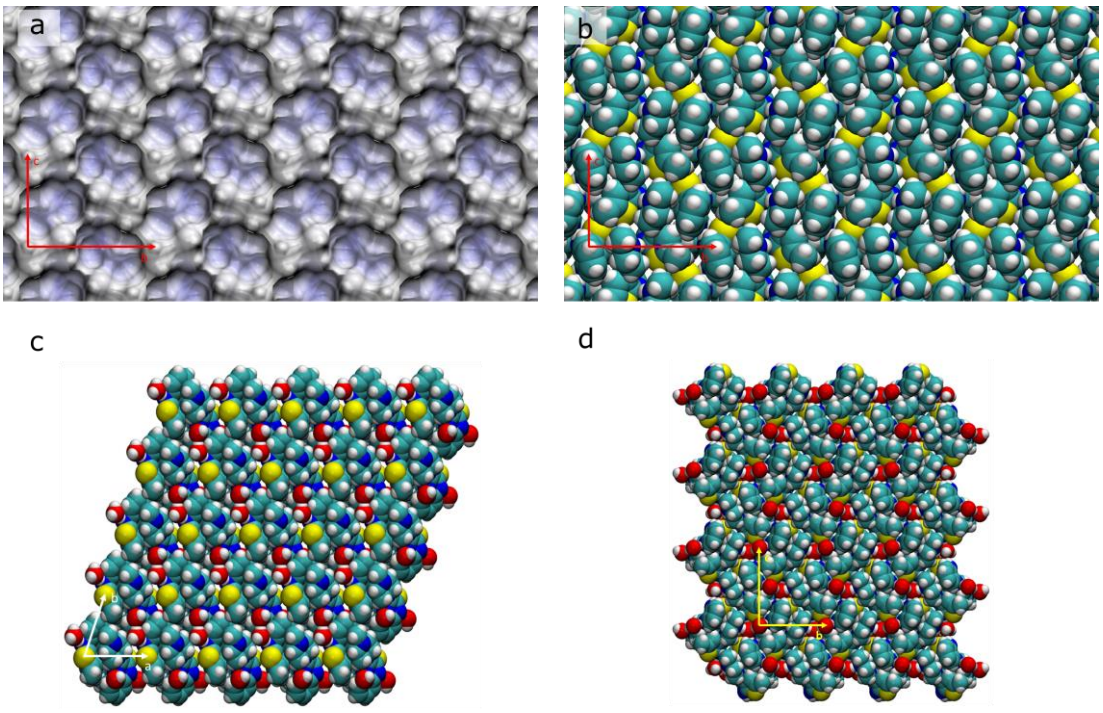

Figure 30 a) Top view of OZPN form I (100) face in a surface representation (white for surface bumps to blue pits, height difference ca. 3 Å) and b) VdW atomic representation (atoms are colour coded: carbon- green, hydrogen- white, sulphur- yellow, oxygen- red, nitrogen- blue); c) bottom view of OZPN DD nanocrystal (5x5) showing $(001)_{OZPNDD}$ face; d) bottom view of a OZPN DB nanocrystal (4x4) showing $(100)_{OZPNDB}$ face.

ORIENT was used to find the optimum binding energy of each nanocrystal with the $(100)_{OZPNI}$ face (normalized to one SC_0 dimer), as a function of the relative orientation and height of the two faces (Figure 30). The OZPN DD nanocrystal has a significantly stronger binding energy than OZPN DB for any orientation, with the average differing by 7 kJ/mol per dimer. The weak binding between the OZPN DB nanocrystal and OZPN I is fairly independent of their relative orientations, consistent with the DB crystallites adhering to $(100)_{OZPNI}$. The most favourable orientations of the OZPN DD nanocrystals are for 90-95° (Figure 30), which is consistent with the observed value of 91° ± 2° (Figure 22 d). The cause of this difference in the interactions

between the two nanocrystals with $(100)_{OZPNI}$ is apparent from the molecular structure in the most favourable orientation (Figure 30).

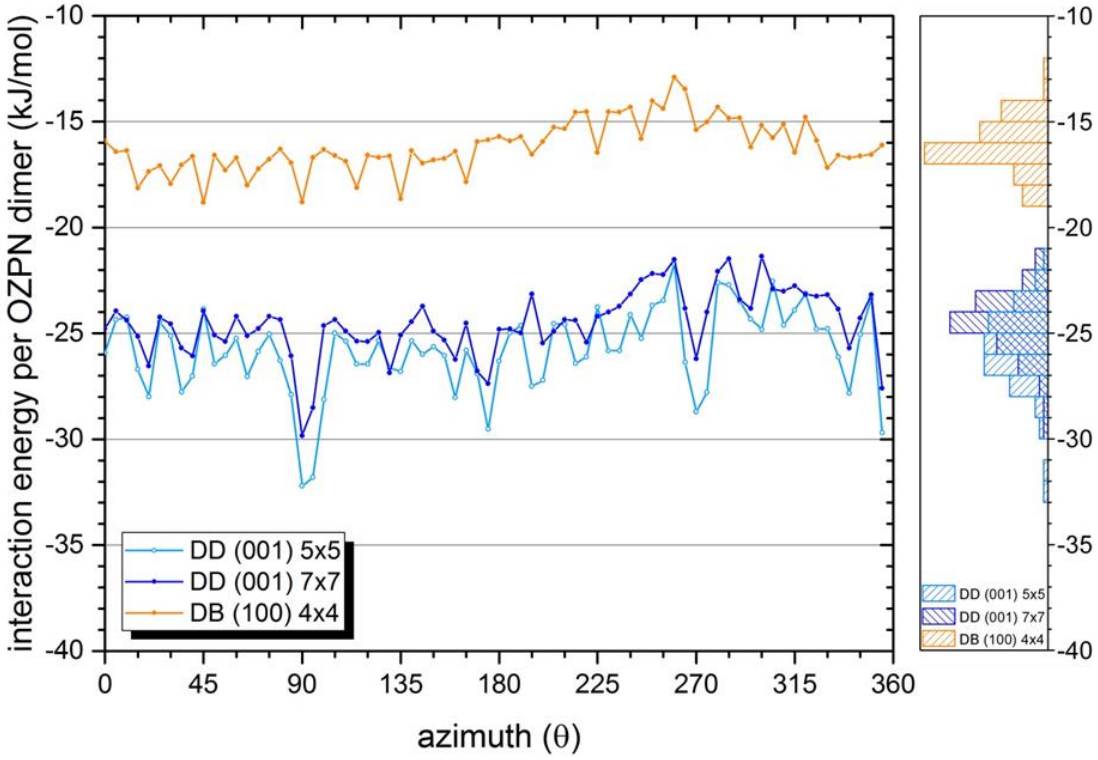

Figure 31 Interaction energies of $(001)_{OZPNDD}$ and $(100)_{OZPNDB}$ nanocrystals with OZPN I (100) face, normalized to be per OZPN dimer. Two different-sized nanocrystals are used for OZPN DD, which span the size of the OZPN DB nanocrystal, as a test of size dependence. Azimuthal angle θ=0° corresponds to the angle between the $[010]_{OZPNI}$ and the $[100]_{OZPNDD}$ or $[010]_{OZPNDB}$.

In the most favourable orientation, the OZPN DD nanocrystal has the piperazine rings of OZPN DD in contact with the aromatic and alkyl CH_n groups of $(100)_{OZPNI}$ surface, though water molecules are also close (Figure 31 a). The top view of the attached nanocrystal shows that along $[100]_{OZPNDD}$ of the nanocrystal, there is a repeating pattern of close contacts between the bottom of the nanocrystals and the surface bumps. These are largely CH_2/CH_3 groups of piperazine rings and CH from aromatic rings on the substrate. This pattern of close contacts can be seen to shift gradually along $[010]_{OZPNDD}$. However, the size of surface bumps means that nearly all

OZPN DD unit cells maintain close contact with them. Hence, there are close interactions between the molecules over a significant fraction of the surface, with quite a good degree of periodic repeats over this small area. There is a considerable area of van der Waals contact between the two surfaces, which increases the favourable dispersion interactions accounting for the larger binding energy. There are still significant void spaces between the two crystal structures. However, if the only favourable water binding site on $(100)_{OZPNI}$ is occupied, then further water molecules could fill the void and hydrogen bond to the water molecules within the DD structure. Some relaxation of the nanocrystal could further enhance the binding, but such distortions will only be small. Hence, the nanocrystal calculations support the observation that $(100)_{OZPNI}$ templates the nucleation of OZPN DD, by favouring the formation of a sufficiently large nucleus with the OZPN DD structure to establish the growth of this phase.

In contrast, the $(100)_{OZPNDB}$ face has less van der Waals contact with the $(100)_{OZPNI}$ surface, with only aromatic CH groups in contact with the hydrophobic OZPN surface, giving a smaller binding energy in all orientations. These aromatic⋯aromatic contacts are still approximately periodically repeated, but there are significantly fewer close contacts between the other atoms in the two surfaces than in OZPN DD, providing less dispersion-stabilized binding (Figure 10 c). The hydrophobic void space is much larger than for the OZPN DD nanocrystal, requiring a much larger cluster of water molecules to make any hydrogen bonding chain between $(100)_{OZPNI}$ N4 sites and the water molecules in the DB nanocrystal.

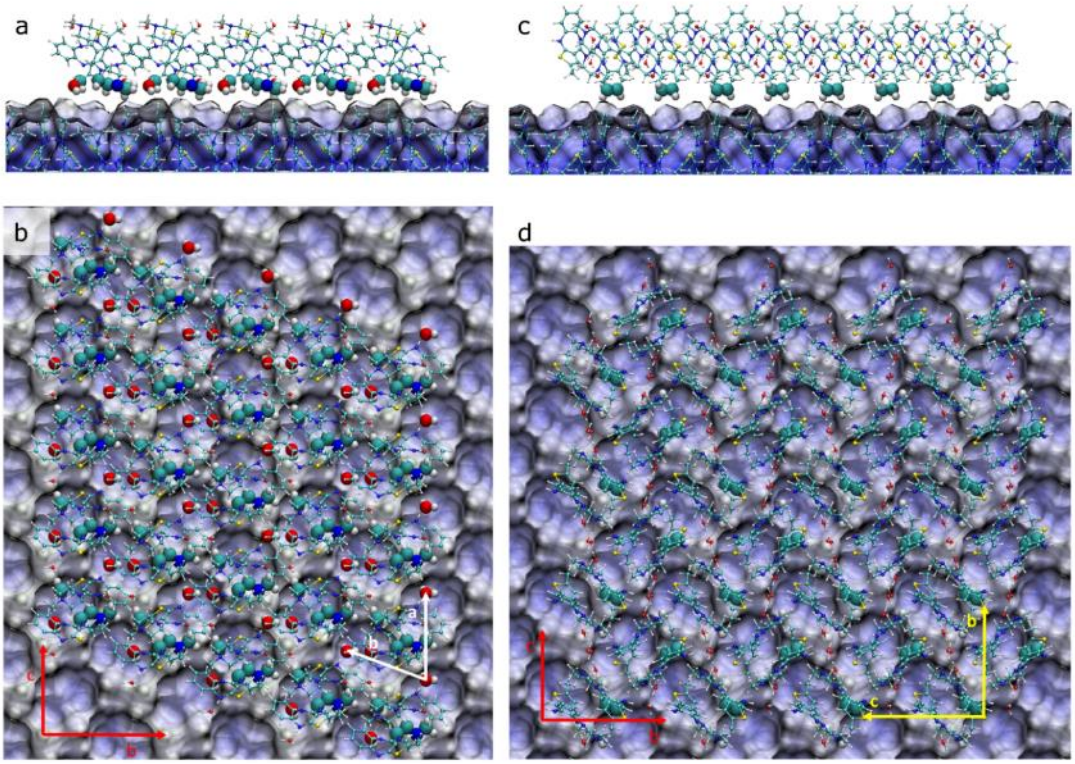

Figure 32 a) Side-view and b) top-view of the optimal attachment geometry at θ=90° for (001)$_{OZPNDD}$ nanocrystal on (100)$_{OZPNI}$ face, with interaction energy of -32.20 kJ/mol per OZPN dimer; (c) Side-view and d) top-view of the optimal attachment geometry at θ=90° for (100)$_{OZPNDB}$ nanocrystal on (100)$_{OZPNI}$ face, with interaction energy of -18.79 kJ/mol per OZPN dimer. θ=0° corresponds to the angle between the [010]$_{OZPNI}$ and the [100]$_{OZPNDD}$ or [010]$_{OZPNDB}$. Atoms in nanocrystals within a vertical distance of 3 Å of the substrate were shown as CPK model. Surface representation colour scheme depicts surface height from blue low (pits) to white high (bumps). Unit cell vectors are shown in red for (100)$_{OZPNI}$, white for (001)$_{OZPNDD}$ and yellow for (100)$_{OZPNDB}$.

Once the prenucleation dense phase is present and nanodroplet coalescence has occurred, (100)$_{OZPNI}$ face is a better match, in terms of functional group interactions, with the (001)$_{OZPNDD}$ face structure than (100)$_{OZPNDB}$. This is only apparent from explicitly modelling the intermolecular interactions, as the interaction between OZPN molecules are dominated by dispersion interactions. As either dihydrate crystal grows, the registry with the underlying surface will gradually decrease, but the nanocrystal models used are of a sufficient size to show the difference in the interactions and

possibly to establish an effective nucleus for growth. The $(100)_{OZPNI}$ face has only one buried water binding site, being otherwise hydrophobic, so other waters are only bound by forming a water network. There is a stronger binding energy to encourage the formation of a OZPN DD nucleus, displacing some of the water network on this surface, and for it to be more firmly attached than any crystallites of OZPN DB.

4.6 Conclusions

The experimental and simulation approaches have shown a two-step nucleation mechanism in the formation of OZPN DD on the surface of the dominant face of OZPN I. Significant differences in the polymorphic outcome were observed with different stirring conditions owing to the reduced influence of the OZPN I surface on nucleation from droplets that have been removed from direct contact by shear. In quiescent conditions, only the presence of the thermodynamic form OZPN DD was observed on the surface of $(100)_{OZPNI}$ and AFM directly visualizes the formation of dense nanodroplets at steps that are able to grow and coalesce until nucleation occurs. This two-step nucleation process results in a crystal that is closely bound to the OZPN I surface. The crystal form produced is templated by the $(100)_{OZPNI}$ surface which shows a structural similarity and energetic preference for OZPN DD over the metastable OZPN DB. Under stirred conditions, nanodroplets can be detached from the surface, resulting in the nucleation and formation of OZPN DB without any templating effect from the $(100)_{OZPNI}$ surface.

Examination of OZPN I surface properties, i.e. geometry, molecular functionality and crystal structure, showed that nucleation of OZPN DD occurs due to stronger intermolecular interactions between $(100)_{OZPNI}$ and $(001)_{OZPNDD}$ than with the largest face of OZPN DB. Even though a ledge-driven epitaxy mechanism was not observed, ledges play an important role in the nucleation process, by providing a site for the formation of dense droplets of OZPN and water molecules in prenucleation clusters, where the variety of stronger binding sites allows more OZPN SC_0 dimers to accumulate, faster than onto the terraced surfaces.

This hydration study is limited to a specific surface of a specific form of OZPN and in specific conditions which differ critically from a slurry conversion, in that there are no particle collisions that would refresh or produce different crystal surfaces. The kinetics are ideal for the application of AFM and are related to the low solubility of OZPN. However, the slow kinetics leading to surface hydrate formation at levels below those which are detected by conventional methods are highly relevant to long-term material storage behaviour. In this regard, this surface characterization approach complements traditional methods of establishing phase stability over the shelf-life of the drug product. The epitaxial formation of hydrates is not widely reported,[146] though this probably contributed to the common observation that API dissolution rates may decrease with time on storage. This example shows that more work on surface chemistry should unravel the complexity of the possible hydration and polymorph transformation pathways of pharmaceuticals such as OZPN.

5 Mesoscopic clusters in olanzapine solution

5.1 Introduction

The origin of mesoscopic clusters observed during crystallisation of organic,[43,45] inorganic[37,38] and protein[29,30,78] systems is poorly understood. A two-step nucleation model for protein crystallisation has been widely studied mainly due to undesired aggregation of proteins causing pathologies such as sickle cell anaemia,[147] but also increasing manufacturing of proteins as medications.[148]

Mesoscopic clusters observed in saturated and undersaturated protein solutions are of interest since they are the locum of crystal nucleation.[29,78,80,149] The mechanism of cluster formation based on nucleation and crystallisation of lysozyme proteins assumes that these clusters are not micelles since the protein concentration in the bulk solution continues to increase upon adding more protein even after clusters appear. Mesoscopic clusters have been observed in solutions of proteins that do not form any permanent oligomers which indicates that covalently bound complexes or other permanent oligomers are not responsible for cluster formation. Mesoscopic clusters are also not gel-like objects and their size is not determined by the particle charge and short range attraction.[77] These prenucleation species are rather considered to be a spatially inhomogeneous mixture of protein monomers and transient complexes of proteins that is in equilibrium with the bulk solution. There is no net exchange of protein monomers or protein complexes between clusters and the solution and this results in a decoupled behaviour between the cluster radius and the volume fraction upon concentration changes. The cluster radius is stable over wide range of concentrations, solution ionic strength and pH,[148,150] while volume fraction increases with the concentration. Water ordering also has a significant influence on crystal formation.[77] These findings suggests that the cluster population could be controlled by

tailoring a subtle interaction that can enhance or suppress weak oligomerisation of molecules in solution.

As presented in Chapter 4, the transformation of OZPN I to OZPN DD in unstirred solution is facilitated by an intermediate, liquid-like phase, that deposits as liquid clusters on {100} faces of OZPN I, and serves as a nucleation medium for OZPN DD. When introduced into the bulk solution, the liquid clusters give rise to a metastable dihydrate polymorph, OZPN DB. Both observations starkly diverge from the generally envisioned polymorph transition pathways. Nucleation of OZPN DD and OZPN DB hosted by the dense liquid droplets contradicts the tenets of classical nucleation theory, according to which crystal embryos emerge in the solution by ordered assembly of solute molecules.[24–27] On the other hand, it appears in accord with the two-step nucleation mechanism, according to which crystal nucleation is facilitated by dense liquid precursors.[29,32,106,151] This mechanism has been observed with protein,[29,30,78,80] inorganic,[37,38,152] and organic[43,45,83] molecules. Macroscopic dense liquid, appearing after "oiling out" and stable with respect to the solution, has been observed with organic molecules.[153] The OZPN dense liquid clusters, however, *do not* represent a stable phase: they form a relatively monodisperse population with dimeter of ca. 80 nanometers and their growth upon deposition on the crystal surface appears to be not by association of monomers from the solution, but by coalescence with other clusters.

This chapter aims to characterise OZPN mesoscopic liquid clusters in terms of solution composition. The cluster formation mechanism is deducted from the properties of the cluster population and its evolution. OZPN clusters exhibit similar behaviour to

protein-rich clusters of comparable size, which assemble owing to the dynamics of formation and decay of transient dimers.[77] This chapter compares the cluster behaviour in solvents that contain varying amount of ethanol and demonstrate that the fraction of OZPN, captured in the clusters, is dictated by the thermodynamic parameters of the solutions. On the other hand, the cluster size is decoupled form the volume of the cluster population and is likely determined by the dynamics of cluster assembly.

5.2 Results and Discussion

5.2.1 Detection of mesoscopic clusters in OZPN water solution

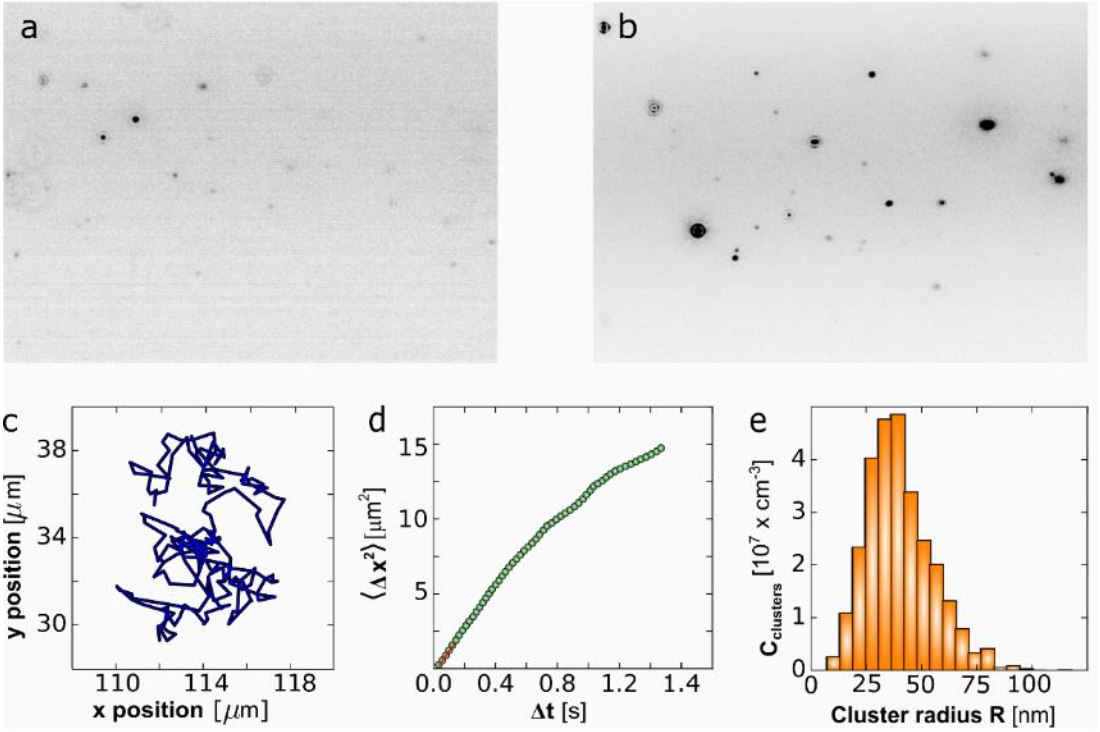

Figure 33 Characterization of the mesoscopic OZPN-rich clusters by oblique illumination microscopy (OIM). (a) A typical image, shown as a negative, in which the clusters appear as dark speckles, of OZPN clusters in H_2O. The observed volume is 120 × 80 × 5 μm^3 (L × W × H). (b) A typical image of clusters in 3 mM OZPN solution in EtOH/H_2O 80/20 (v/v). (c) A typical cluster trajectory obtained from the position of a cluster in a sequence of images. (d) Determination of the diffusion coefficient D of a cluster from the correlation of its mean squared displacement $\langle \Delta x^2 \rangle$ and the lag time Δt. First five data points are highlighted with a red line. (e) The distribution of cluster sizes obtained from five OIM movies recorded at distinct solution volumes.

Undersaturated solutions of OZPN are expected to be homogeneous at all lengthscales, including the molecular. The extinction coefficient of OZPN in water is not available in the literature, and the low solubility in this solvent hampered its determination. Hence, to obtain an undersaturated OZPN solution.a solution saturated with respect to OZPN DB was prepared by incubating overnight OZPN I crystals in water under constant stirring; under these conditions, OZPN I transforms to OZPN DB.[123] The most

stable crystal form in aqueous solutions is OZPN DD. However, the transition to OZPN DD takes from five to seven days.[123] The saturated solution (against OZPN DB) was separated from the crystals by filtration and diluted with 20 % additional water by volume. The concentration of the diluted solution was below the solubility of OZPN DB. Surprisingly, observations of the undersaturated solution with OIM revealed the presence of particles that randomly migrate, driven by Brownian collisions with the solvent molecules, Figure 33 a. Careful examination of all steps in the solution preparation excluded the possibility that these heterogeneities are dust particles or gas bubbles.[154]

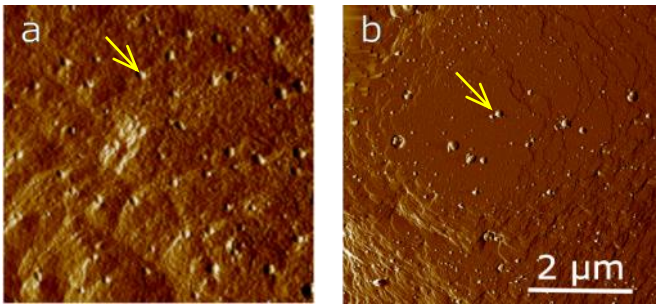

Figure 34 Dense OZPN-rich clusters (indicated with yellow arrows) on the surface of OZPN crystals imaged by atomic force microscopy. (a) Clusters on (100) face of OZPN I after incubation in water for 4 h, (b) Clusters on the surface of OZPN:EtOH:H_2O after incubation for 1 h in saturated solution in EtOH/H_2O 1/1 (v/v).

To test if the particles are crystals, the OIM setup was equipped with a polarizer at the optical entrance of the cuvette and an analyser at the optical exit, in front of the objective lens. If the polarizer and analyser are perpendicular to each other, crystals, which rotate the plane of light polarization would produce bright speckles. In this situation the field of view was completely dark, disproving the hypothesis that the speckles seen without the polarizer in Figure 33 a represent crystals and indicating that these particles are disordered.

The size of each particle was determined from its Brownian trajectory (Figure 33 c). The average was ca. 35 nm in water. This size is similar to the clusters observed on (100) surfaces of OZPN crystals in aqueous solutions, Figure 34 a. The cluster concentration in the pure water was low, likely owing to the very poor aqueous OZPN solubility. This challenged the further characterization of the clusters.

As ethanol (EtOH) is known to significantly increase OZPN solubility,[124] the presence of OZPN clusters in 1/1 EtOH/H_2O on the surface of OZPN hydrate ethanoate in a saturated solution was confirmed using AFM (Figure 34 b). The size of the clusters observed in 1/1 EtOH/H_2O was similar to the size of OZPN clusters observed in water. OIM characterization of OZPN solution in 80 % v/v EtOH (C_{OZPN} = 3 mM) revealed a higher cluster concentration, (Figure 33 b) with relatively narrow size distribution, (Figure 33 e), between 15 and 80 nm, and a mean radius of ca. 35 nm.

5.2.2 Identification and reversibility of the mesoscopic OZPN-rich clusters.

To further characterize the mesoscopic OZPN-rich clusters, the time evolution of the cluster population was monitored and tested the consequences of varying C_{OZPN}.

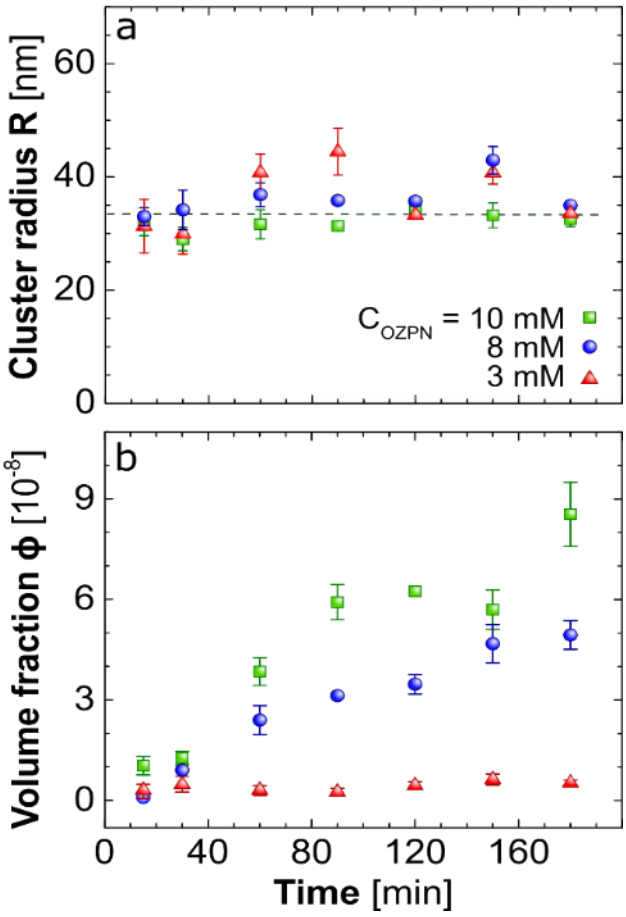

Figure 35 Evolution of the OZPN cluster population in 80 % v/v EtOH solution. (a) The average cluster radius R. (b) The volume fraction ϕ in solutions with OZPN concentrations shown in (a). The averages of five determinations in distinct solution volumes are shown. The error bars represent the standard deviation.

The cluster radius is independent of the solution concentration and was steady in time for up to three hours, Figure 35 a. In contrast, the fraction of the solution volume occupied by the cluster population ϕ increases with C_{OZPN} and solution age, Figure 35 b. The evolution of ϕ was verified as not due to OZPN precipitation or any other process in the solution hosting the clusters. The OZPN concentration, determined spectrophotometrically, remained steady. No changes in the solution UV-Vis spectra, illustrated in Figure 13, were recorded, suggesting that the ϕ growth may be induced

by processes occurring in the liquid comprising the clusters, which stabilize the clusters and increase the cluster population by spawning additional clusters of consistent size. The slow growth of ϕ is consistent with slow maturation of the cluster phase. The high refractive index of this liquid, evidenced by the scattered intensity, suggests that the OZPN concentration in the clusters is higher than in the solution. The associated higher viscosity is conducive of slow dynamics.

A crucial issue in understanding the cluster mechanism is whether the clusters adjust to the parameters of the solution, or represent irreversibly aggregated matter. As a test of cluster reversibility, the response of ϕ to higher C_{OZPN} is noted to be disproportional: as C_{OZPN} is raised by about three-fold, from 3 to 10 mM, ϕ increases from 0.5×10^{-8} to 8.5×10^{-8}, i.e., ca. 17-fold, Figure 35 b; the latter ratio is consistent at all times, at which ϕ is sufficiently large for accurate distinction between the three concentrations. The exaggerated increase of ϕ driven by higher C_{OZPN} contradicts expectations for irreversible aggregates, whose concentration would increase proportionally to C_{OZPN}. This increase indicates that the cluster population adjusts to the solution conditions and the clusters do not represent irreversibly aggregated material.

The characteristics of the cluster population revealed in Figure 34 and Figure 35 are unusual for both disordered aggregates and emerging domains of a new phase, such as OZPN dense liquid. The narrow size distribution is inconsistent with both types of aggregation. The decoupled behaviour of R and ϕ are in contrast with classical phase transitions, in which the number of nucleated domains and the volume that they occupy increase concurrently. The mesoscopic size of the clusters is steady over extended

times, in sharp contrast to expectations for newly formed phases in which the domain size grows in time.[155]

This size is much larger than the prediction of colloid clustering models[46] that are often applied to aggregation in solution.[156–163] As the cluster population captures a minor fraction of the dissolved OZPN, the concentration of the solution in contact with the clusters is close to the initial 3, 8, or 10 mM. This observation is beyond the catalogued behaviours of micelles, which equilibrate with solutions of constant critical micelle concentration (CMC). Thus, the OZPN clusters observed in Figures 33 – 35 are not micelles.

On the other hand, these characteristics are typical of the mesoscopic solute-rich clusters, found in solutions of numerous proteins at varying conditions[31,35,77–79,109,164] Similar to OZPN clusters, the protein cluster size is steady and independent of the parameters that define the solution thermodynamics, such as pH, ionic strength, and protein concentration.[35,78,79,109] By contrast, the volume fraction of the clusters is determined by the solute intermolecular interactions.[35,77,106,109] A recent theory explained a range of puzzling cluster behaviors;[77,165] several of the model assumptions and resulting predictions have been supported by experimental evidence. [106,109,166] This model posits that the mesoscopic clusters consist of a concentrated mixture of intact monomers and transient dimers. The dimer lifetime determines the cluster radius *R*. On the other hand, in agreement with the experimental data,[35,77,106,109] the cluster volume fraction ϕ is dictated by the solution thermodynamics.[77,109] ϕ is related to the solute fraction ν held in the clusters. Indeed,

$$\nu = n_{cl}/n_{OZPN} = C_{cl}V_{cl}/C_{OZPN}V = (C_{cl}/C_{OZPN})\phi \quad (12)$$

where n_{cl} and n_{OZPN} are the amounts of OZPN in the clusters and solution, respectively, V_{cl} and V are the corresponding volumes, [35] and

$$\phi = V_{cl}/V. \quad (13)$$

The OZPN concentration in the dense liquid comprising the clusters, C_{cl}, is significantly greater than C_{OZPN}, so that choosing a constant ratio C_{cl}/C_{OZPN} in the range 10 – 100 is reasonable. Furthermore, direct application of the Boltzmann distribution suggests that

$$\nu \approx \exp(-\Delta G_{cl}/k_BT) \quad (14)$$

where ΔG_{cl} is the free energy excess of a molecule in a cluster over that in the solution.[48] Thus, ϕ is determined by the free energy balance of clusters formation and the decoupled behaviours of R and ϕ emerge naturally from the model.[77]

5.2.3 The response of the cluster population to varying EtOH concentration.

The applicability of the transient dimer model to the OZPN clusters was tested by monitoring the response of the cluster population (cluster radius, R and volume fraction, ϕ to varying concentration of EtOH. The cluster radius R is independent of the EtOH concentration in the range 20 – 90 %, Figure 36 a. On the other hand, ϕ depends on C_{EtOH} in a complicated non-monotonic fashion, Figure 36 b. Concurrent with observations of mesoscopic clusters in protein solutions and in compliance with the predictions of the transient dimer model,[77] R and ϕ are decoupled.

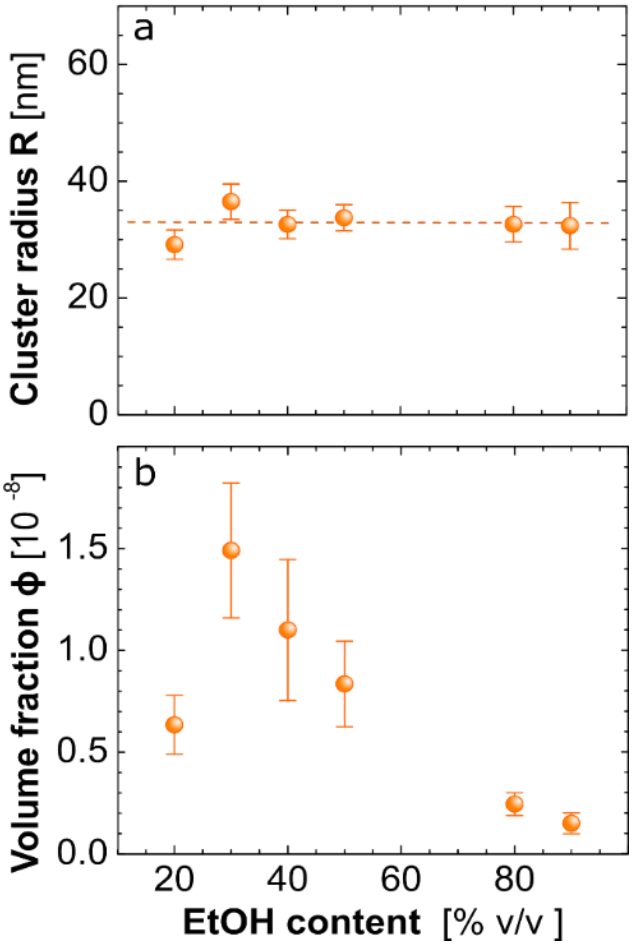

Figure 36 The cluster population in EtOH/H_2O solvents of different composition. (a) The average cluster radius R. (b) The volume fraction occupied by the cluster population ϕ on EtOH concentration. The OZPN concentration was 5 mM in all experiments. The averages of five determinations in distinct solution volumes are shown. The error bars represent the standard deviation.

5.2.4 The thermodynamics parameters of OZPN crystallisation from EtOH/water mixtures.

To understand if the variations of ϕ in response to increasing C_{EtOH} are driven by the thermodynamic parameters of the solution, the thermodynamics of OZPN solutions were characterized in mixed EtOH/water solvents. OZPN crystals were chosen as a reference state. X-ray powder diffraction patterns of crystals grown at different EtOH/water ratios (Figure 37 a) reveal that OZPN crystallizes from all

solvents as the OZPN dihydrate ethanoate, depicted in Figure 37. The crystallisation enthalpy ΔH^o_{cryst}, entropy ΔS^o_{cryst}, and free energy ΔG^o_{cryst} characterize the difference between the crystals and the solution. Since the crystals grown in all tested solvents belong to the same polymorphic form, the disparities of ΔH^o_{cryst}, ΔS^o_{cryst}, and ΔG^o_{cryst} in different solvents distinguish the state of the OZPN solute in each solvent. The crystallisation enthalpy ΔH^o_{cryst} can be measured calorimetrically by scaling the heat released during crystallisation (at constant temperature and pressure *p*) with the crystallized mass. This determination can be distorted by solution trapped between crystals and mislabeled as crystalline mass. An alternative method is to determine the solubility C_e of the crystals at different temperatures and to employ standard thermodynamics relations and $C_e(T)$ to determine ΔG^o_{cryst}, ΔH^o_{cryst}, and ΔS^o_{cryst}.[113,167] The solubilities of OZPN with respect to the OZPN dihydrate ethanoate crystals in six C_{EtOH} follow the expected quasi-exponential dependence on temperature, Figure 6a. The equilibrium constant for the reaction OZPN(solution) ⇆ OZPN(crystals) is $K = C_e^{-1}$.

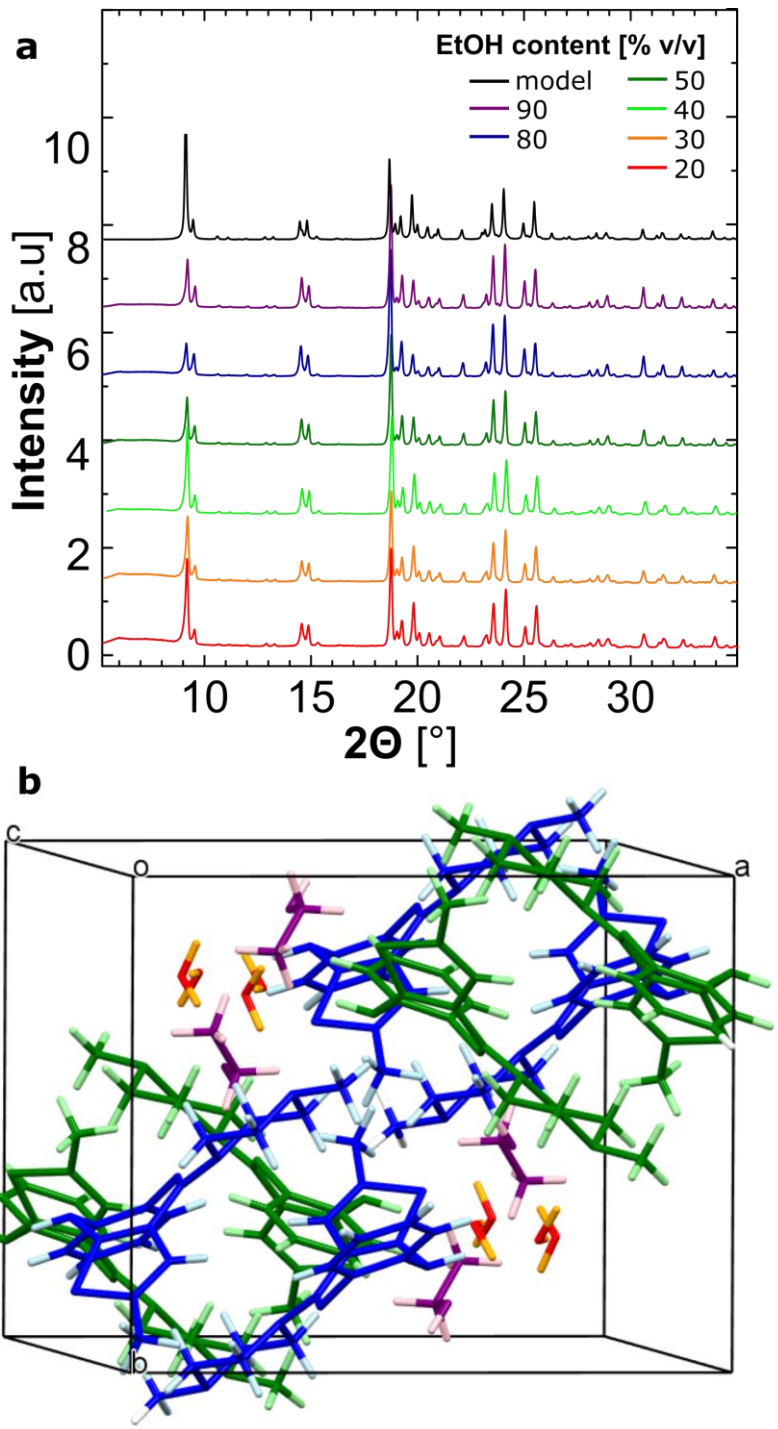

Figure 37 a) X-ray powder diffraction patterns of crystals grown in EtOH/H_2O solvents with composition listed in the legend. Top: a model pattern computed using the software package Mercury and structure coordinates for the crystals of OZPN dihydrate ethanoate with Cambridge Structural

Database entry WEXQEW, b) crystal structure of OZPN hydrate ethanoate crystallising in space group $P2_1/c$[124]

The product, OZPN(crystals), represents a distinct phase and their activity is assigned to be one by thermodynamic convention. Furthermore, owing to the low C_e, the respective activity coefficients are assumed to be close to one. Hence,

$$\Delta G^o_{cryst} = -RTln\,K = RTln\,C_e. \tag{15}$$

To determine ΔH^o_{cryst}, the van't Hoff relation written as:

$$\left[\frac{\partial ln C_e}{\partial(1/T)}\right]_{p,n_j} = \frac{\Delta H^0_{cryst}}{R} \tag{16}$$

where n_j designates the concentrations of the other solution components, EtOH and water. The van 't Hoff relation suggests that the slope of the correlation $\ln C_e(T^{-1})$ is proportional to ΔH^o_{cryst}. The data on OZPN solubility, plotted in van 't Hoff coordinates, Figure 38 b, indicate that ΔH^o_{cryst} is constant in the studied temperature range. Finally, $\Delta S^o_{cryst} = (\Delta H^o_{cryst} - \Delta G^o_{cryst})/T$ and is proportional to the intercept of the $\ln C_e(T^{-1})$ plots, Figure 38 b.

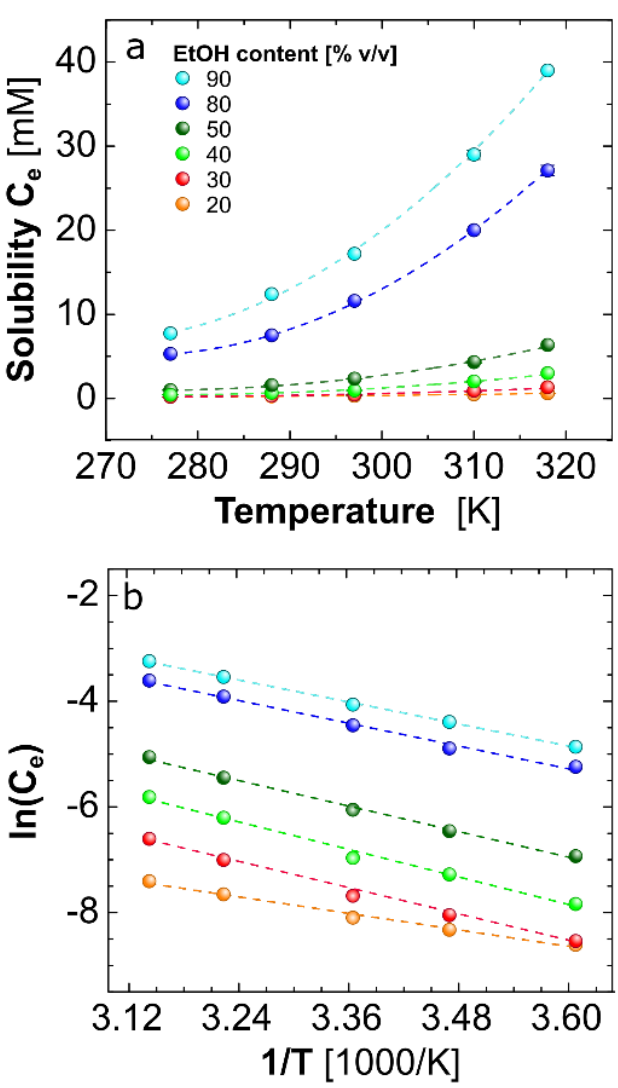

Figure 38 The solubility of OZPN with respect to the crystals of OZPN ethanol hydrate in EtOH/H_2O solvents of composition shown the legend in (a). (a) The temperature dependence of the solubility C_e in the range 277 – 318 K, dashed lines are polynomial fits. The standard deviation of three independent determinations carried out in parallel is smaller than the symbol size, (b) OZPN solubility plotted in van't Hoff coordinates, dashed lines are linear regression fits.

ΔS^o_{cryst} is a sensitive probe of the molecular-level processes that accompany crystallisation. An OZPN molecule in the solution is surrounded by solvent molecules, some of which may be associated with OZPN.[168–170] For instance, water molecules exposed to the non-polar OZPN moieties would form a structured shell, surrendering their mobility.[171] Recent modelling suggests that five water molecules are tightly

associated with each OZPN in the solution and are positioned in a way that preserves their bond when dimers form.[145] When an OZPN molecule incorporates in the crystal, some of the associated solvent molecules may be released and in this way regain their translational and rotational degrees of freedom. ΔS^o_{cryst} has a negative component due to the lost degrees of freedom as one OZPN, one EtOH, and two water molecules are confined to the crystal lattice. A positive component accounts for the gained freedom of solvent molecules attached to OZPN in the solution and released upon crystallisation. ΔS^o_{cryst} represents the balance between the two. The entropy loss corresponding to the incorporation of water molecules in ice is ca. –22 J $mol^{-1}K^{-1}$, consistent with water entrapped in clathrates, crystal hydrates, or other ice-like structures.[171–175] For the larger EtOH, the corresponding number, evaluated from the entropy of fusion, is –31 J $mol^{-1}K^{-1}$.[176] The relevant parameter for OZPN would be the entropy of crystallisation from the melt, which is not available in the literature. As OZPN is significantly larger than EtOH, the entropy lost upon entrapment should have greater magnitude than –31 J $mol^{-1}K^{-1}$.

The dependence of ΔS^o_{cryst} on the EtOH content in the solvent transitions sharply from –3 to –62 J $mol^{-1}K^{-1}$ as the C_{EtOH} increases from 20 to 30 % v/v and stays constant for C_{EtOH} between 30 and 90 % v/v, Figure 39 a. The values of ΔS^o_{cryst} at both sides of the transition result from the balance of confined OZPN, EtOH, and water and released solvent molecules and cannot be interpreted in the absence of data on the structure of the solute – solvent complexes. The magnitude of the transition, however, ca. 60 J $mol^{-1}K^{-1}$, suggests that three water molecules may be associated with OZPN in the 20 % EtOH solution and set free upon incorporation of OZPN into the crystal. This number

is consistent with the five waters predicted to tightly bind to OZPN[145] and the two water molecules trapped in the lattice. In solutions with EtOH content of 30 % v/v and higher, these water molecules are displaced from the vicinity of OZPN and do not affect the entropy balance of crystallisation. The constant value of ΔS^{o}_{cryst} in the EtOH range from 30 to 90 % v/v suggest that no additional water molecules are dissociated from solute OZPN by higher EtOH concentrations.

Table 7 The entropy ΔS_{cryst}, enthalpy ΔH_{cryst}, and free energy ΔG_{cryst} at 298 K of OZPN crystallisation from solutions with different EtOH content.

EtOH content [% v/v]	**ΔS° [J mol^{-1}K^{-1}]**	**ΔH° [kJ mol^{-1}]**	**ΔG° [kJ mol^{-1}]**
20	-5.72±0.69	-21.53±2.59	-19.82±0.21
30	-61.52±7.40	-37.03±4.46	-18.70±0.06
40	-63.02±7.58	-35.60±4.29	-16.82±0.09
50	-62.88±7.56	-33.56±4.03	-14.82±0.01
80	-63.72±7.66	-29.87±3.59	-10.89±0.03
90	-63.68±7.66	-28.87±3.47	-9.89±0.02

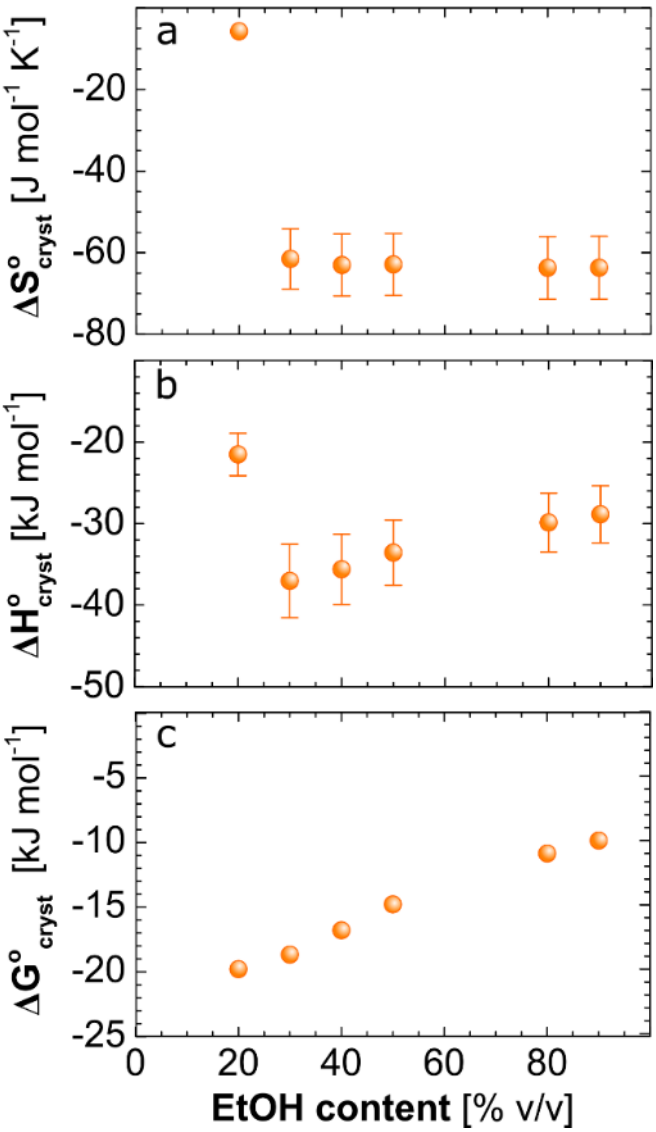

Figure 39 The thermodynamic parameters of crystallisation of OZPN ethanol hydrate in EtOH/H_2O solvents of different, a) Crystallisation entropy ΔS^{o}_{cryst}, b) Crystallisation enthalpy ΔH^{o}_{cryst}, c) Gibbs free energy ΔG^{o}_{cryst} at 298 K. The error bars in a) and b) represent the standard deviation of the

intercept and slope, respectively, of the linear correlations in Figure 38b. The standard deviation for ΔG° was determined from that of C_e and is smaller than the symbol size.

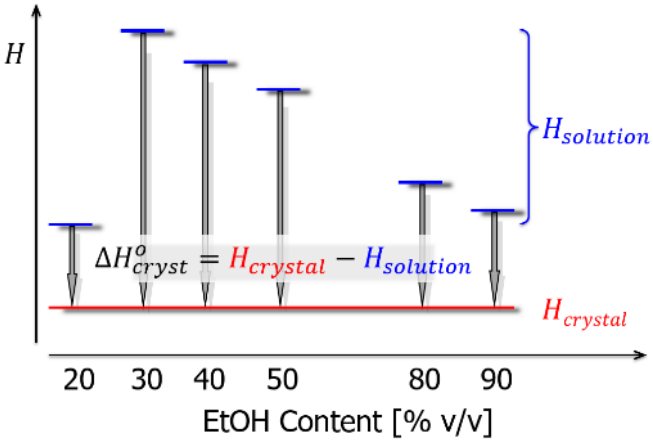

Figure 40 The enthalpies of the solution and crystal emerging from the ΔH^o_{cryst} data in Figure 39 b. The arrows indicate the transition from solution to crystals and their negative direction corresponds to the sign of ΔH^o_{cryst}. $H_{solution}$ varies with the EtOH content antisymmetrically to ΔH^o_{cryst}.

ΔH^o_{cryst} denotes the difference of the enthalpies of OZPN in the crystal and solution, $\Delta H^o_{cryst} = H_{crystal} - H_{solution}$. Since the crystals forming at different C_{EtOH} are identical, $H_{crystal}$ does not depend on the EtOH content and the variations of ΔH^o_{cryst} are determined by $H_{solution}$, Figure 40. $H_{solution}$ is a measure of solution non-ideality due to intermolecular attractions and repulsions, with higher $H_{solution}$ implying stronger repulsion.[177] Thus, the low magnitude of ΔH^o_{cryst} at 20 % EtOH, Figure 7b, suggests a small $H_{solution}$, corresponding to mild repulsion between the OZPN molecules in the solution. The likely moderating force is the hydrophobic attraction induced by the structured water, indicated by the ΔS^o_{cryst} datum for this solvent in Figure 39 a. As the structured water molecules are stripped at C_{EtOH} equal or greater than 30 %, $H_{solution}$, Figure 40, suggests stronger intermolecular repulsion that may be due to the hydration shells of the polar nitrogen groups of OZPN,

Figure 37 b; note that in contrast to non-polar moieties, water structured at polar groups induces repulsion due to its strong association with the solute.[168,178] The attenuated repulsion at higher C_{EtOH} may be due to the lower dielectric constant of these solutions, conducive of stronger van der Waals attraction.[179] ΔG^{o}_{cryst} is a convolution of ΔH^{o}_{cryst} and ΔS^{o}_{cryst}.

5.2.5 Solution thermodynamics dictates the cluster volume fraction.

To understand the non-monotonic dependence of ϕ on the EtOH content, Figure 36 b, direct application of the relation between ϕ and ΔG_{cl}, derived above, is not feasible since data on ΔG_{cl} are unavailable. $H_{solution}$ in solvents of different composition, Figure 40, is used as an indicator for the intermolecular interactions between the solute molecules. The variations of $H_{solution}$ parallel those of ϕ. This synchronous behavior suggests that stronger repulsion between the solute OZPN molecules, indicated by higher $H_{solution}$, drives the fraction ν and the correlated volume ϕ. In agreement with the transient dimer model of cluster formation, the cluster population volume and the fraction of solute captures in the clusters are determined by the solution thermodynamics.

The dimer identity is the final step in the application of the transient dimer model to the OZPN-rich clusters. The known experimental crystal structures of neutral OZPN are comprised of the so-called SC_0 dimer, a centrosymmetric motif depicted in Figure 11 and Figure 37 b.[7,123,133] The transient dimer may be akin to that structure. This hypothesis is tested in Chapter 6.

The finding of the thermodynamic control of the cluster phase volume and the suggested dimer identity imply a thermodynamic and a structural pathway to control the cluster population and hence the nucleation and polymorph transformation pathways directed by the clusters, in Chapter 4. The thermodynamic parameters of the solution may be modified by low-concentration additives that act on the intermolecular interactions. The dimer may be suppressed by a subtle structural modification of the molecule, compatible with its biological activity.

5.3 Conclusions

Solutions of the antipsychotic drug OZPN in purely aqueous and mixed EtOH/aqueous solvents exhibit solute-rich clusters of radius *R* ca. 35 nm. The clusters occupy ca. 10^{-8} – 10^{-7} of the solution volume and capture ca. 10^{-7} – 10^{-5} of the OZPN in the solution. The clusters are disordered and likely liquid and do not represent any of the known OZPN condensed phases. The clusters are of interest since OZPN I to OZPN dihydrates transition suggests that they may be crucial sites for the nucleation of emerging crystal forms in the course of OZPN polymorph transitions.

Cluster radius *R* is steady in time and independent of the OZPN concentration and the solvent composition. On the other hand, the volume of the cluster population ϕ, related to the fraction of OZPN molecules captured in the clusters ν, is a sensitive function of both parameters. The results suggest that ϕ and ν are dictated by the thermodynamics of the OZPN solution. The steady mesoscopic *R*, decoupled from the volume of the clusters phase, contradicts predictions of classical theories of phase transformation and recent aggregation models. These discrepancies suggest that the OZPN-rich clusters represent a unique condensed phase and unusual cluster behaviors are consistent with the predictions of a model that assumes the formation of OZPN dimers and their decay upon exiting the clusters. A transient dimer, akin to the centrosymmetric motif present in most of the 60 known OZPN crystal structures, may be the oligomer underlying cluster formation. The cluster population and the nucleation and polymorph transformation pathways, mediated by the clusters, can be controlled by modifying the thermodynamic parameters of the solution and suppressing the formation of dimers or other oligomers.

6 Growth of olanzapine crystals from preformed precursors.

6.1 Introduction

Studying the process of crystal growth from solution is an important across a wide range of fields, including pharmaceuticals,[73,180] biomolecules,[112,181,182] proteins,[183–185] minerals[81,186] and colloids.[187,188] The classical terrace-ledge-kink model[85] assumes a crystal grows by incorporation of monomers from solution to the crystal layers originating from either two-dimensional (2D) nucleation on the crystal terraces or steps originating from screw dislocations that form hillocks. There is now significant evidence that crystal growth processes may also occur via non-classical routes involving more complex precursors varying from molecular oligomers to amorphous and nanocrystalline species preformed in solution.

In solution, the intermolecular interactions between the molecules, dictated by the nature of the solute and the solvent may lead to self-association of solute molecules to dimers, trimers or larger clusters. There is a limited understanding how these self-associated clusters affect the nucleation and growth of a specific polymorph, despite numerous studies linking the structure of oligomers present in solution with synthons present in a crystal structure.[67–69,100,105] Several types of solution spectroscopies including IR, Raman and NMR are used to provide information about the nature of the intermolecular interactions especially with H-bonding involved. NMR can provide a self-association constant and with assistance from molecular modelling also the structure of the complex. Along with many other examples, structures of self-associates of isonicotinamide,[101] sulfamerizine[65] and tetrolic acid[69,100,103] were proven to have direct correlation with the synthon observed in the crystal structures. It was confirmed that the properties of the solvent can change the nature of solute interactions e.g. form dimers to chains and hence favour another polymorphic form to crystallise.

The presence of hydrogen bonded cyclic dimers of glycine in aqueous solution was proposed based on analysis of diffusion coefficients[103] and there were suggested as a basic building block for α-glycine crystals based on surface x-ray diffraction.[189] Further measurement of freezing-point depression suggested that contrary to these assumptions glycine mostly exist as monomers in aqueous solution.[190] Molecular dynamic calculations suggested that the open chain dimer is actually more stable than both the cyclic dimer and the monomer in aqueous solution.[191] Further MD studies showed that only 15% of glycine molecules form dimers and that these are mostly short lived (less than 1 ps) and that the number of hydrogen bonds with lifetimes higher than 5 ps was negligible. A further examination of glycine structures in aqueous solutions shows that only 10% of dimers are head-to-tail, cyclic dimers, while 90% of them are single hydrogen bonded dimers, contrary to the assumption that the crystallisation of α-glycine over other polymorphic forms in aqueous solution is dictated by cyclic dimers in water.[191,192]

Extended studies show that the solution-phase associates do not always match the synthon present in the crystal structure e.g. benzoic acid in methanol,[193] mandelic acid in nitromethane, acetonititrile, and methanol,[69] and inosine dihydrate in water.[194] For these systems the dimer structures present in the crystal structure were not detected in solutions and there was no direct correspondence between solution species and structural synthons. Even though the correlation between solution-phase associates and the crystal structure exists for some systems, there is no clear evidence that these associates directly contribute to the growth of the crystal layers.

More complex solute aggregates such as prenucleation clusters are a part of non-classical nucleation mechanism for numerous structures[81,99,195] including heteropolyacids,[47] InP quantum dots,[48] polymers,[46] proteins (lysozyme,[35,36] hemoglobin A and S,[77] glucose isomerase,[51] lumazine synthase,[31,78] and insulin) and several amino acids (glycine, aniline and DL-valine[41–45]). Recent results demonstrated the sedimentation of a submicron dense droplet followed by incorporation to the crystal layer was observed during growth of lumazine synthase,[31] and the integration of mesoscopic clusters from solution to a crystal layer during growth of DL-glutamic acid monohydrate[50] suggests non-classical crystal growth mechanism by attachment and structural rearrangement of prenucleation clusters. Other examples of non-classical growth include amorphous particles,[196,197] or nanocrystals.[98,99] Besides its fundamental significance, understanding the growth mechanism is especially valuable from an industrial perspective and for the design of improved crystal engineering tools such as crystal structure[198–200] and crystal morphology[61,63,64,91] predictions.

In the case of olanzapine, extended solvent screening did not result in diverse crystal packing. All crystal structure obtained from 56 solvents and vapour phase contain the SC_0 dimer[7,123,124] (Figure 11 b) suggesting that this dimer may be a building block for OZPN all neat and solvated solid- forms.[62,145] There is no experimental evidence that SC_0 is observed in OZPN solutions and is a part of a growth mechanism. Mesoscopic clusters detected in OZPN solutions (discussed in Chapter 4) exhibit the behaviour similar to protein clusters and their radius is stable with concentration and solvent composition. The fraction of OZPN, captured in the clusters, is dictated by the thermodynamic parameters of the solutions. With this characteristic decoupled behaviour of the cluster size and fraction of the clusters in solutions, OZPN clusters

follow the same mechanism of formation as protein clusters including presence of the transient dimer species. Although the clusters are significant for OZPN anhydrate to hydrate transition, there is no evidence that they are a part of the crystal growth mechanism.

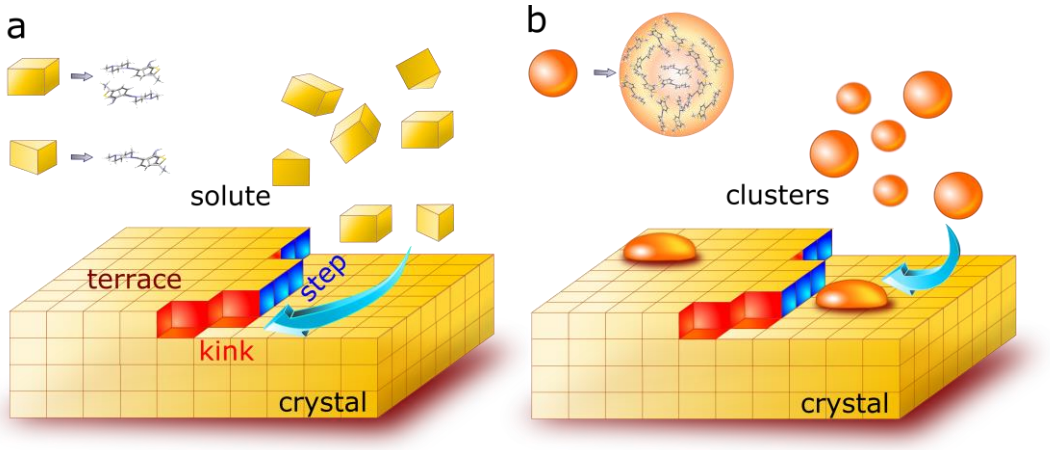

Figure 41 Possible mechanisms of OZPN crystal growth a) growth occurs by incorporation of OZPN monomers or dimers to the kinks, b) growth occurs by incorporation and rearrangement of prenucleation clusters formed in 1/1 EtOH/H_2O solution.

This chapter explores possible growth pathways for olanzapine crystals. Several scenarios are considered (Figure 41): classical growth by monomer-to-monomer addition and non-classical growth by SC_0 dimers or growth by incorporation of prenucleation clusters. The nucleation of OZPN DD on the surface of OZPN I was previously monitored by AFM (chapter 3), although the kinetics of growth were relatively slow due to the low driving force limited by very low solubility of OZPN and its dihydrates in water. Addition of ethanol to water significantly increases the solubility of OZPN (as described in chapter 4), making it possible to study the formation and growth of new OZPN hydrate ethanoate (OZPN HE) layers with AFM in 1/1 EtOH/H_2O at various supersaturations. The formation of OZPN dimer was

studied using NMR and Raman spectroscopies in EtOH/H_2O and several other solvents (acetone and chloroform). It was observed that prenucleation clusters do not take part in the growth mechanism and new OZPN layers are generated by a spiral growth while step velocities show non-linear dependence on supersaturation.

The proposed growth model suggests that new OZPN layers propagate by incorporation of OZPN dimers that are present as a minor species in OZPN 1/1 EtOH/H_2O solution. The surface diffusion mechanism is discussed and adsorption energies (U_{ads}) for OZPN monomer and OZPN dimer reveal that the OZPN dimer has lower adsorption energy. This result indicates that the dominant mechanism for growth is dimer adsorption to the crystal terrace followed by diffusion to the kink. Due to the higher adsorption energy of the monomers their population is much lower on the crystal terrace and the crystal surface serves as a collector of dimers. Therefore incorporation of OZPN dimers is kinetically favoured over incorporation of monomers.

6.2 Results.

6.2.1 Growth and characterisation of olanzapine hydrate ethanoate (OZPN HE) crystals

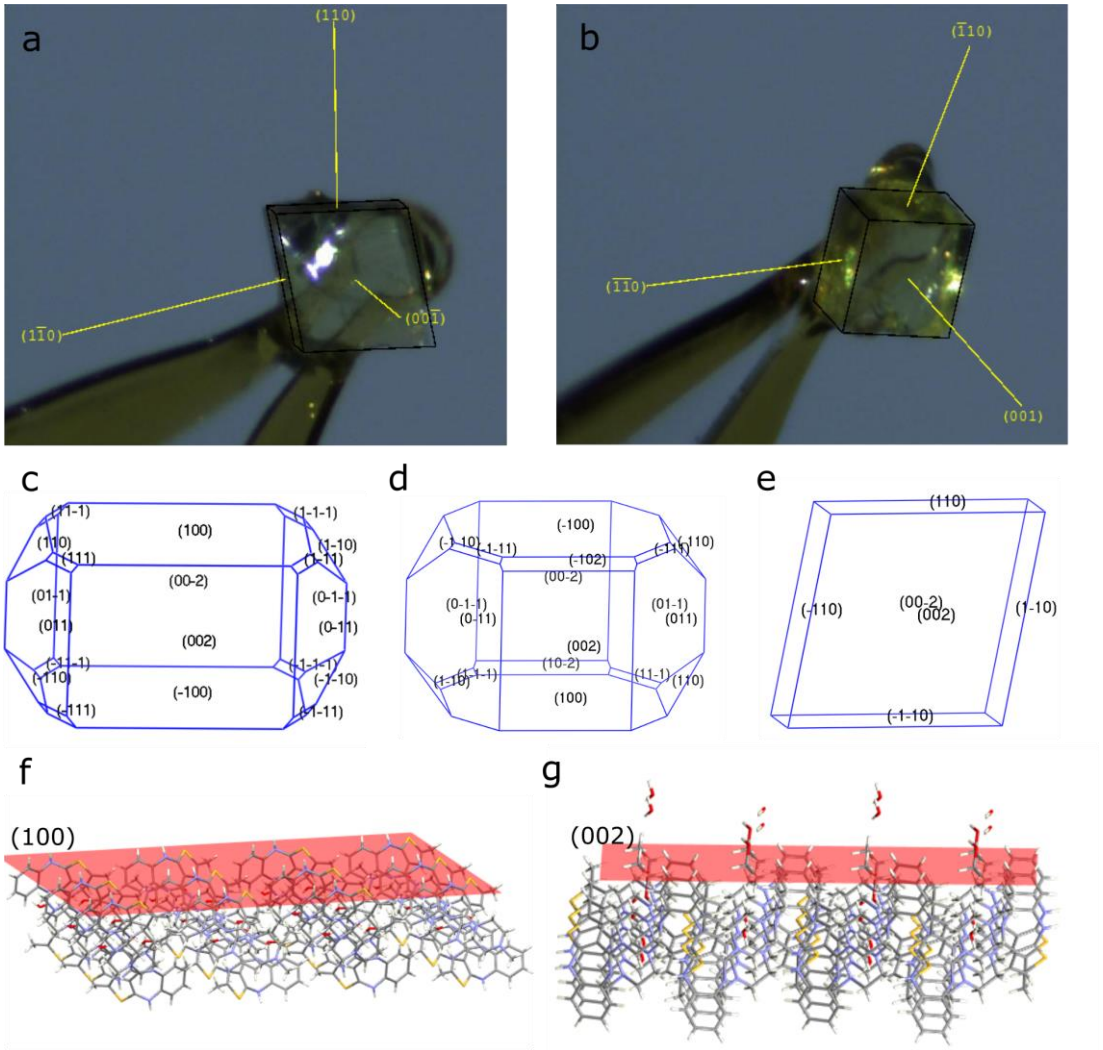

Figure 42 Morphology of OZPN HE crystals, a) and b) single crystal of OZPN HE obtained from cooling crystallisation of EtOH/H_2O solution with face indices annotated, c) BFDH morphology, d) growth morphology, e) observed morphology, f) surface chemistry of (100)$_{OZPNHE}$, g) surface chemistry of (002)$_{OZPNHE}$.

Table 8 Attachment energies per OZPN monomer for growth morphology model for OZPN HE

OZPN HE (hkl)	multiplicity	d_{hkl} [Å]	$E_{att\ (total)}$ [kcal/mol]	$E_{att\ (VdW)}$ [kcal/mol]	$E_{att(electrostatic)}$ [kcal/mol]
{ 1 0 0}	2	15.118	-73.617	-66.735	-6.872
{ 0 1 1}	4	10.551	-125.101	-94.600	-30.501
{ 0 0 2}	2	9.977	-78.962	-78.261	-0.7008
{ 1 1 0}	4	9.600	-133.218	-75.144	-58.063
{ 1 1 -1}	4	8.755	-140.467	-97.319	-43.147
{ 1 1 1}	4	8.550	-138.930	-105.981	-32.949

To explore the growth mechanism of OZPN crystals, time-resolved in situ AFM was employed to image crystals (~500 μm in size) grown from 1/1 EtOH/H_2O solution. In situ AFM was previously used to study the anhydrate to hydrate transition of OZPN I in chapter 4 and was also applied to numerous other system to study classical and non-classical crystallisation mechanisms.[50,87,115,183] OZPN HE was reported to crystallise in two polymorphic forms, where form I crystallises in a space group $P2_1/c$[124] and form II crystallising in space group $C2/c$.[123,128] Hydrate ethanoate form I consists of parallel dimers of olanzapine molecules, whereas form II shows orthogonal arrangement of dimers with ethanol and water molecules occupying the cavity.[128] OZPN HE form I crystals were obtained by cooling crystallisation from mixtures of EtOH (between 10 – 90%) in H_2O. The unit cell dimensions are a = 15.129 Å, b = 12.431 Å, c = 19.977 Å, β = 92.73°. The crystals are light yellow in colour and show a rhombohedral morphology with large $\{002\}_{OZPNHE}$ faces and $\{110\}_{OZPNHE}$ smaller faces (Figure 42 a, b). The dominant $(002)_{OZPNHE}$ face observed from recrystallized samples is the second largest face predicted from BFDH or growth morphology (Figure 42 c, d, Table 8). The largest face predicted by attachment energy calculations is $(100)_{OZPNHE,}$ although this face is not observed in experimentally

obtained crystals. This may be due to the fact that $(002)_{OZPNHE}$ consists of SC_0 OZPN dimers with N4 nitrogens sticking out. These are available for H-bonding with ethanol and water molecules. Significant adsorption of the solvent molecules on that face makes this face the biggest and slowest growing.

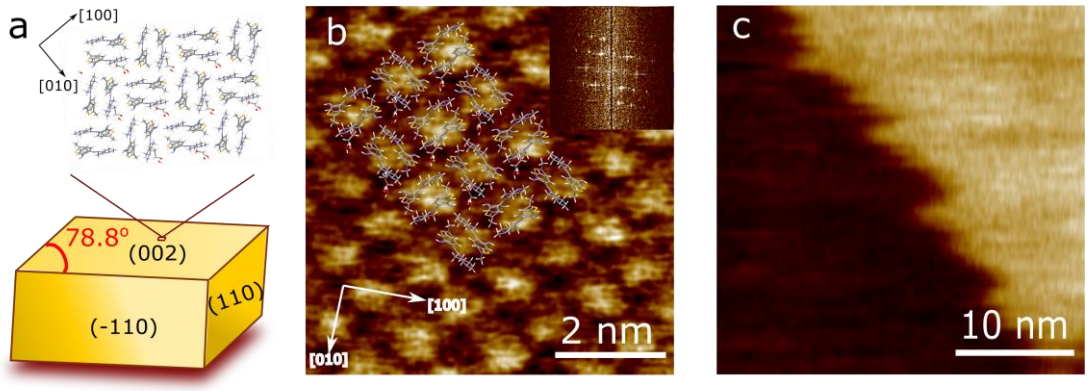

Figure 43 Structure of OZPN $(002)_{OZPNHE}$ surface, a) crystal model showing the arrangement of SC_0 dimers on $(002)_{OZPNHE}$ face, b) AFM lattice resolution image of $(002)_{OZPNHE}$, arrangement of SC_0 dimers is detectable and overlaid with OZPN crystal structure, inset: Fourier transform of obtained image illustrates rhombic symmetry of molecular arrangement in $(002)_{OZPNHE}$: four order peaks, corresponding to resolution 3.78 Å c) structure of the OZPN steps with high kink density.

An AFM image of the $(002)_{OZPNHE}$ surface with molecular resolution showing the packing of SC_0 dimers is given in Figure 43 b. The measured lattice spacing in the [100] and [010] directions and the β angle agree with the crystallographic data for this structure. AFM topographical image of $(002)_{OZPNHE}$ face in Figure 43 c revealed the presence of unfinished layers that are terminated by the steps with heights h = 0.98 ± 0.05 nm, equivalent to a half of a unit cell for OZPN HE form I in c direction and the height of one molecular layer of OZPN. Figure 43 c shows structure of the step at the solubility with very high kink density.

6.2.2 Mechanism of layer generation and step propagation

OZPN is known to form prenucleation clusters in EtOH/H_2O solution and their radius does not depend on the solution composition, although the fraction of a volume that clusters occupy depends on the solvent composition (as showed in chapter 5). A solvent composition of 1/1 EtOH/H_2O was selected due to the good solubility of OZPN and relatively high fraction of OZPN clusters observed at this solvent composition. The volume fraction of clusters increase over time (Figure 35 b). Therefore to explore the crystal growth mechanism in the presence of prenucleation clusters, the supersaturated solution (*C*-*Ce* = 0.640 mM) was filtered through 0.22 μm PTFE membrane and next the solution was then pre-aged for 1 h in order to obtain sufficient fraction of clusters. The clusters are easily imaged by AFM on the surface $(002)_{OZPNHE}$ (Figure 44). The average radius was ca. 35 nm which corresponds with the size previously measured by OIM.

The clusters are dynamic entities and as described in chapter 4, affected by the local stirring from the AFM probe. Clusters that landed on the crystal surface between existing steps, do not contribute to either the generation or propagation of crystal layers at the time of monitoring ~3 h (Figure 44). Clusters adsorbed on the surface act rather as a foreign bodies and when removed from the crystal surface by an AFM probe leave circular cavities with a depth of several crystal layers (Figure 44). Based on that observation it is concluded that new layers of OZPN crystals do not grow by incorporation of prenucleation clusters on the surface of OZPN crystals.

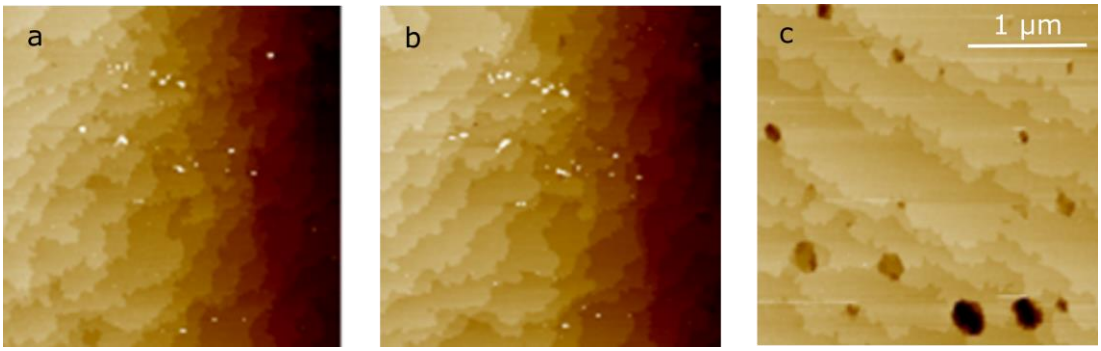

Figure 44 Clusters do not contribute to the growth of OZPN HE layers, a) clusters adsorbed on terraces at time 0 h, b) clusters adsorbed on terraces at time 3 h, c) clusters removed from the surface of the crystal leaving inclusions.

Searching for a source of growth layers at all measured supersaturations 0.02 mM < C-Ce < 2.55 mM, new layers of OZPN HE are generated by the simple and complex screw dislocations shown in Figure 45. The four-sided polygonal spiral hillocks generated by a dislocations show the straight segments that are parallel to the respective crystal edges. When the steps are generated by two screw dislocations with the same starting point, the double spiral forms a hillock (Figure 45 b). Also, more complex hillocks comprising of multiple spirals were observed (Figure 45 c). The dislocation sources on the OZPN HE surface are both left- and right- handed.

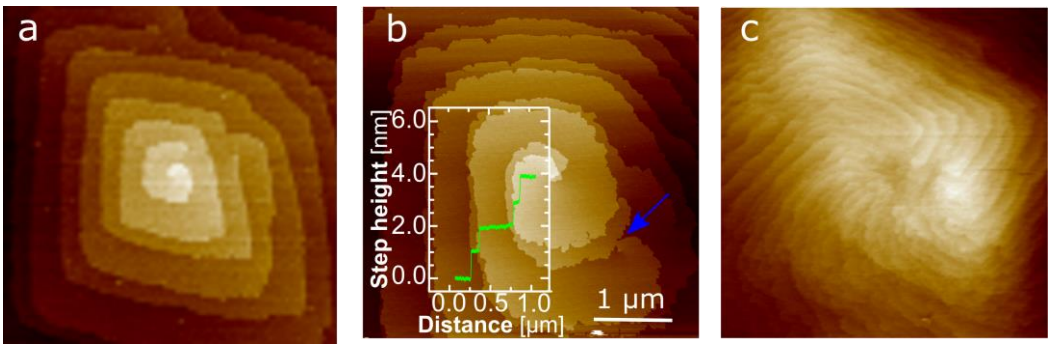

Figure 45 Generation of a new layers by screw dislocations on the surface of a (002)$_{OZPNHE}$ crystal, a) single dislocation produces hillock, b) double dislocation produce hillock, and single dislocation

is present on a lower terrace marked with blue arrow, inset: height profile of generated steps, c) multiple dislocations work in cooperation to produce a hillock.

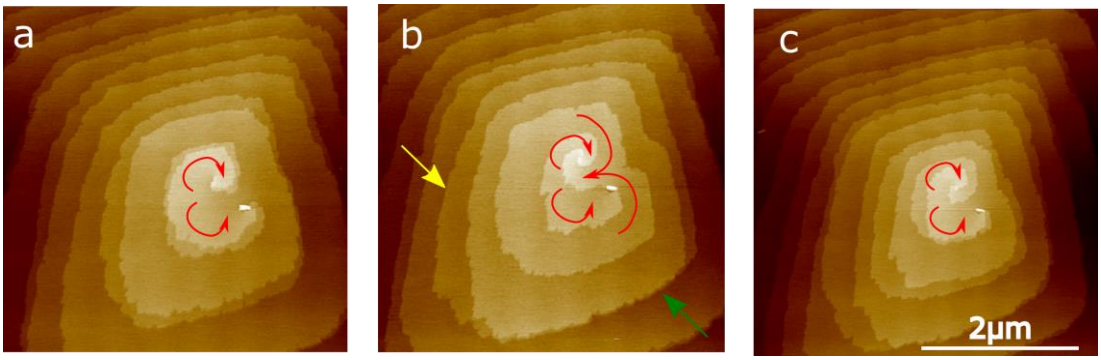

Figure 46 Cooperation of screw dislocations: two double spirals producing a diagonal hillock, a) two double spirals moving in opposite directions, b) only one of each double spirals interacting together causing temporary asymmetric step split (green arrow showing steps travelling together in [110] direction and yellow arrow showing splited steps in [1-10] direction) and producing a Frank-Read dislocation d) reconstruction of two double spirals in opposite direction, the interaction is repeated.

Figure 46 shows the interaction between two double spirals of opposite direction. When two spirals grow in the same direction they produce a hillock and the steps travel in pairs as shown in Figure 46 a. When two spirals of opposite direction produce a Frank-Read source (Figure 46 b) a temporary asymmetric step split occurs. Steps in $[110]_{OZPNHE}$ direction travel together while steps growing in $[1\text{-}10]_{OZPNHE}$ direction split to single steps with a height corresponding of half of a unit cell. Figure 46 c shows the regeneration of two double spiral and the process is repeated.

Typically, there are many active hillocks on a single crystal of OZPN HE. Figure 47 a shows the presence of three single screw dislocations at the supersaturation $C\text{-}Ce$ = 1.54 mM. Smaller spirals present at the lower terraces (marked with blue arrows) are outgrown by the highest dislocation. This suggests that at constant supersaturation steps propagate faster than at the centre of the spiral.

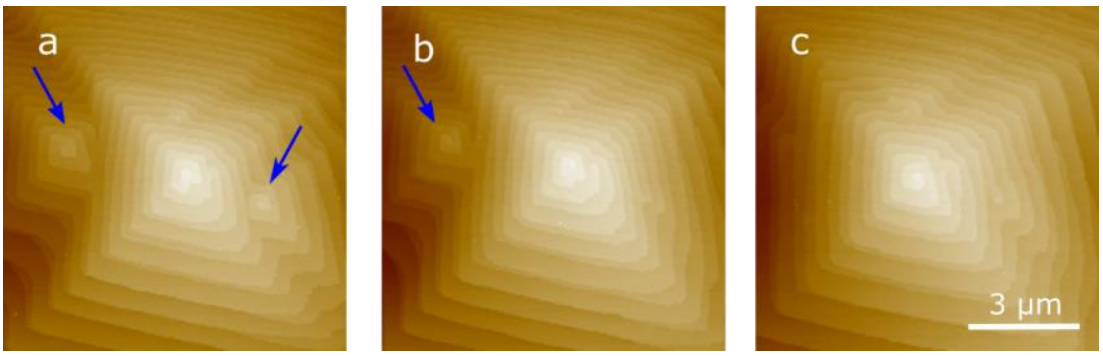

Figure 47 Competition between dislocations, a) two single spirals present on the lower terraces and one single spiral on the highest terrace that dominates the growth, b) one of the smaller spirals overgrown by the dominant spiral, c) second lower spiral overgrown by the dominant spiral. Growth conditions C-Ce = 1.54 mM

6.2.3 Kinetics of the spiral growth in [110] direction

The edges of the generated layers grow by the association of OZPN molecules from the solution. The growth rate, *R*, of a faceted crystal measured in the direction perpendicular to the growing facet is related to step velocity, *v*:[201]

$$R = \left(\frac{h}{l}\right) v \tag{17}$$

Where *h* is step height and *l* is a step length, *(h/l) = p*, *p* is a constant hillock slope. The velocity, *v*, of evolving steps was determined from the slope of step displacement from a reference point measured as a function of time. Step displacement for steps separated $\ell \geq$250 nm was determined from sequential AFM images at constant supersaturation (Figure 48). Analysis of the dependence of the step velocity on OZPN concentration shows a non-linear dependence of the step velocity, *v*, on OZPN concentration Figure 49. This non-linear dependence is a striking observation since the step velocity can be described as:[202]

$$v = a\rho_k u \tag{18}$$

where a is the step propagation length, ρ_k is the kink density (kink sites per step edge site), and u is the kink incorporation rate (net rate of growth unit addition per kink site). The kink incorporation rate, u, represents the difference between opposing fluxes: the attachment rate of solute molecules into kink sites, j_+, and the detachment rates of solute molecules from kink sites, j-.

$$u = j_+ - j_- \tag{19}$$

The rate of incorporation of molecules into kinks j_+ can be treated as monomolecular surface reactions, where expressions are commonly developed from transition state theory.[201–203] The kink attachment rate can be expressed with first order chemical kinetics dependant on solute concentration, C, kinetic constant k^+, a frequency factor, ν_+, and energy barrier, $\Delta U^{\neq}$.[202–204]

$$j_+ = k^+ C = \nu_0 exp\frac{-\Delta U^{\neq}}{k_B T} C_e S \tag{20}$$

While j_- depends only on the energy barrier for detachment ($\Delta U + \Delta W$), ΔW is the work required to detach from kink to solution, k_B is the Boltzmann constant, and T is absolute temperature, C_e is solubility, S is the relative supersaturation based on solute concentration

$$j_- = k^- = \nu_0 exp\frac{-(\Delta U^{\neq} + \Delta W)}{k_B T} \tag{21}$$

$$v = a\rho_k(j_+ - j_-) = a\rho_k\left(\nu_0 exp\frac{-\Delta U^{\neq}}{k_B T}C_e S - \nu_0 exp\frac{-(\Delta U^{\neq} + \Delta W)}{k_B T}\right) =$$

$$a\rho_k\nu_0 exp\frac{-\Delta U^{\neq}}{k_B T}\left(C_e S - exp\frac{\Delta W}{k_B T}\right) \quad (22)$$

At equilibrium, S= 1 $j_+ = j_-, u = 0, exp(\Delta W/k_B T) = C_e$:

$$v = a\rho_k\nu_0 exp\frac{-\Delta U^{\neq}}{k_B T}C_e(S-1) \quad (23)$$

The thermodynamic driving force for OZPN crystallisation is the excess of OZPN chemical potential in the solution over that in the crystal:

$$\Delta\mu = \mu_{solution} - \mu_{crystal} \quad (24)$$

Assuming that OZPN molecules in the solution do not interact with one another and the respective activity coefficient γ is equal to unity at measured concentrations, *a* is activity:

$$\mu_{solution} = \mu^0_{solution} + k_B T ln a, \quad a = \gamma C_{OZPN} \quad (25)$$

$$\mu_{solution} = \mu^0_{solution} + k_B T ln C_{OZPN} \quad (26)$$

$$\mu_{crystal} = \mu^{eq}_{solution} = \mu^0_{solution} + k_B T ln a_{eq}, \; a_{eq} = \gamma C_e \quad (27)$$

$$\mu_{crystal} = \mu^0_{solution} + k_B T ln C_e \quad (28)$$

$$\Delta\mu = exp\frac{\Delta\mu}{k_B T} = \frac{C_{OZPN}}{C_e} = S \quad (29)$$

$$v = a\rho_k \nu_0 exp\frac{-\Delta U^{\neq}}{k_B T} C_e \left[\exp\left(\frac{\Delta\mu}{k_B T}\right) - 1\right] = a\rho_k \nu_0 exp\frac{-\Delta U^{\neq}}{k_B T} C_e \left[\frac{C_{OZPN} - C_e}{C_e}\right] \quad (30)$$

The step kinetic coefficient β introduced by Chernov correlates the step velocity to the driving force $[\exp\left(\frac{\Delta\mu}{k_B T}\right)]$, the step velocity is written as:

$$\beta = a\rho_k \nu_0 exp\frac{-\Delta U^{\neq}}{k_B T} \quad (31)$$

$$v = \beta\Omega C_e \left(\frac{C_{OZPN} - C_e}{C_e}\right) \quad (32)$$

$$v = \beta\Omega(C_{OZPN} - Ce) \quad (33)$$

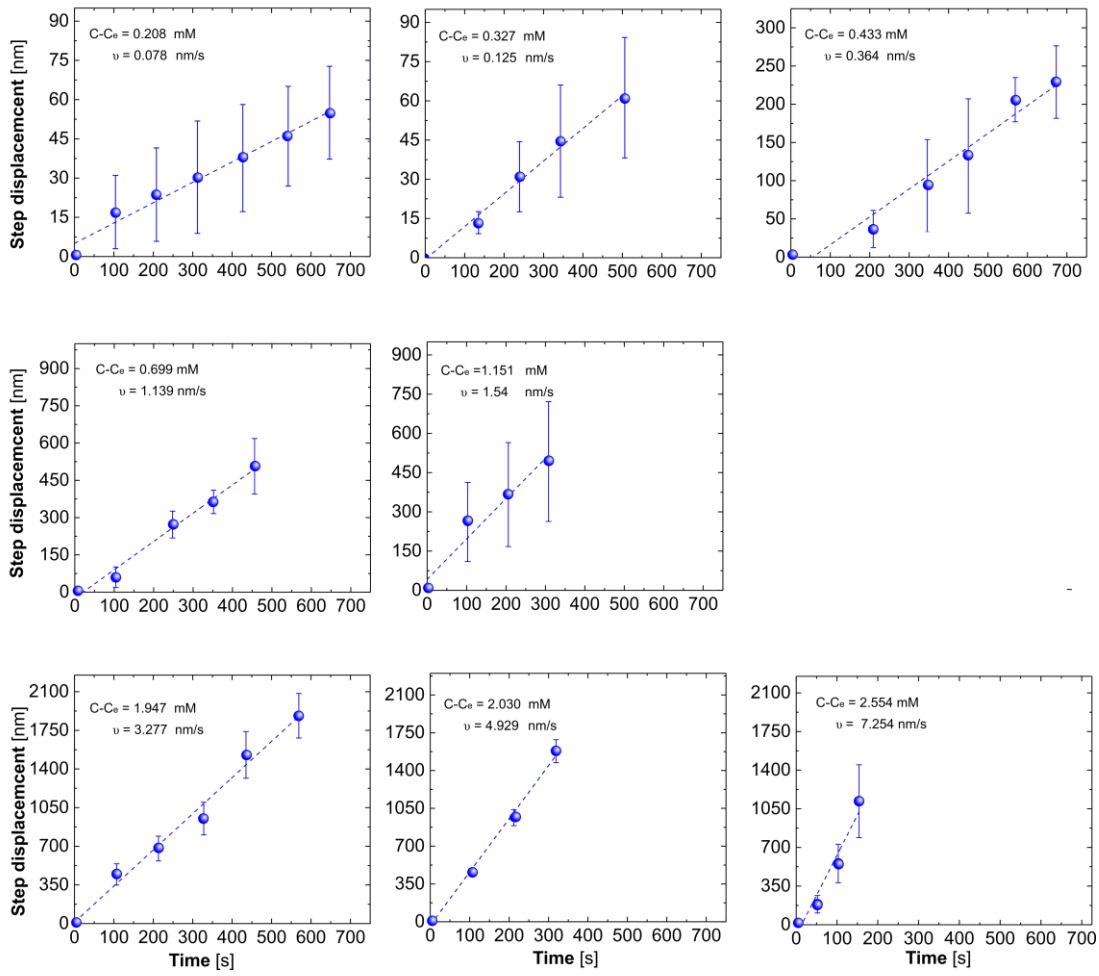

Figure 48. Determination of step velocities at the driving force 0.02 mM < C_{OZPN}-Ce < 2.55 mM. The velocity, v, of evolving steps was determined from the slope of step displacement from a reference point measured as a function of time determined from sequential AFM images at constant supersaturation.

In this expression, Ω is the volume occupied by a OZPN molecule in the crystal and β is the step kinetic coefficient (length/time unit). From equation 33 the linear dependence between step velocity and OZPN concentration is expected. Factors affecting linear dependence of step velocity on OZPN concentration are described below.

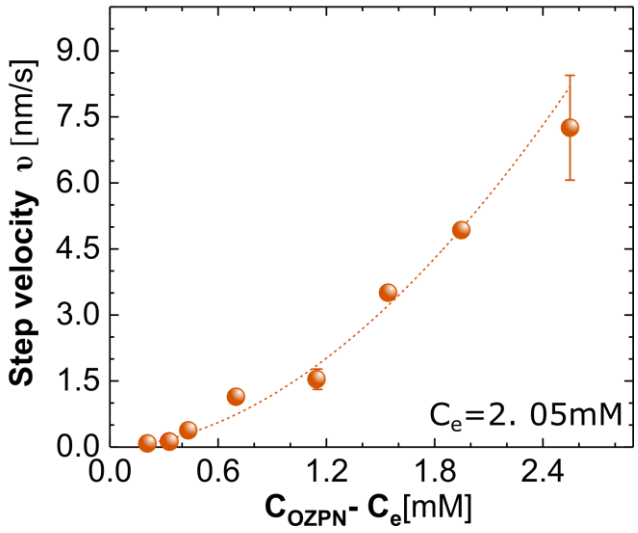

Figure 49 Step velocity v in [110] direction as a function of OZPN concentration in 1/1 EtOH/H_2O concentration for well-separated steps (ℓ ≥250 nm). OZPN solubility in 1/1 EtOH/H_2O is C_e = 2.05 mM at 21°C.

6.2.4 Factors affecting linear dependence of step velocity on OZPN concentration

The step velocity, *v*, may deviate from a linear dependence on C_{OZPN} owing to several factors: (a) competition between the steps for the supply of solute,[85,201,205,206] (b) kink density,[207–209] (c) incorrect solubility measurements, (d) impurity effects,[210,211] and (e) others. To explore which of the above factors affect the kinetics of OZPN HE crystal growth, each of the factors (a-e) is discussed below:

a) *Insufficient supply of solute:*

The are two possible pathways for molecules to be incorporated into the crystal structure: direct incorporation;[86] and surface diffusion.[87–90] When the surface diffusion route dominates, the competition for solute occurs at closely separated steps since they are in competition for supply of molecules from the terrace between them. In this situation there is a strong dependence of step velocity on the interstep distance ℓ. When

direct incorporation of the solute from the bulk solution to the step occurs, the competition for the molecules is negligible at closely packed steps. To determine if surface diffusion is a limiting mechanism for crystal growth, the dependence of the step separation ℓ on supersaturation and the dependence of the step velocity on step separation ℓ were determined.[87–90,212,213] The competition for the solute occurs at steps shorter than ≤ 250 nm (Figure 66) and is discussed in section 6.3.3. Figure 50 a shows that for well-separated steps ≥250 nm the step separation is independent over the range of measured supersaturations. Figure 50 b shows that step separation is independent of step velocity.

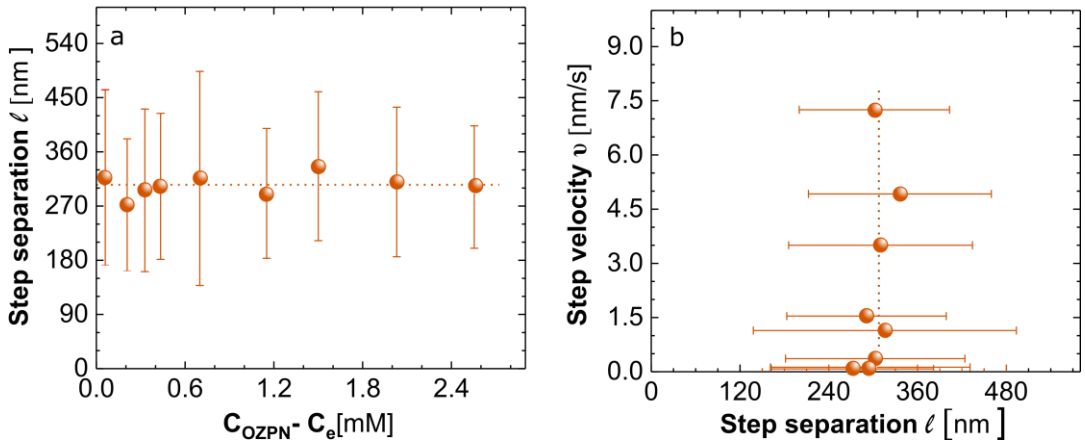

Figure 50 Evidence for no competition for the solute between the steps present on the surface of OZPN HE for steps ≥250 nm, a) step velocity, v, as a function of supersaturation (C_{OZPN} - C_e), b) step velocity, v, as a function of step separation ℓ.

This observation suggests that well-separated (ℓ ≥250 nm) steps are not in the competition for the supply of the solute and ℓ does not increase with supersaturation, so the surface diffusion is not a limiting factor for the OZPN HE crystal growth.

a) *Insufficient kink density.*

The kink density, ρ_k, at the step is one of the most important parameters determining the crystal growth rate and often the growth rates are limited by the availability of kink sites into which growth units can incorporate. The kink generation mechanism has a direct influence on the step velocity, *v* based on equation 18. Kinks can be generated in three ways: 1) by association of two-dimensional clusters to the steps;[207] 2) by one-dimensional nucleation of new crystalline rows;[214] and by 3) thermal fluctuations of the steps.[201] The mechanism by which kinks are generated is easily distinguished at equilibrium concentration. If kinks density is high at equilibrium, kinks are generated by thermal fluctuations; in the opposite situation they are generated by either 2–D cluster formation or 1–D nucleation of new layers. For both mechanism 1 and 2, generation of kinks is a limiting kinetic factor for the incorporation of a new molecule to the steps and shows nonlinear dependence of step velocity, *v*, on supersaturation. To discriminate between the above mechanisms a molecular resolution image of OZPN HE step was acquired at saturation level and determine the kink density. Figure 43 c shows structure of the step with very high kink density, what suggests that the kinks are generated by the thermal fluctuations and more kinks are not generated at higher supersaturation. Kink generation is not a limiting factor for the kinetics of the crystal growth.

b) *Incorrect solubility measurements.*

A dependence of OZPN solubility C_e in 1/1 EtOH/H_2O on temperature is presented in Figure 51. The solubility value for OZPN HE in 1/1 EtOH/H_2O at 21°C was estimated from the solubility curve obtained by bulk crystallisation. In this method aliquots of OZPN EH crystals were added to 5 mL EtOH/H_2O solvent and were stored at each of five temperatures: 4, 15, 25, 37, and 45°C. After a preset time, 300 µL aliquot was removed from each vial, diluted with the respective solvent, and the concentration of dissolved OZPN was determined spectrophotometrically. This procedure was repeated until the concentrations in each vial reached a plateau, defined by three consecutive concentrations of similar value, Figure 14. The final steady-state concentrations were averaged over the three samples for each temperature.

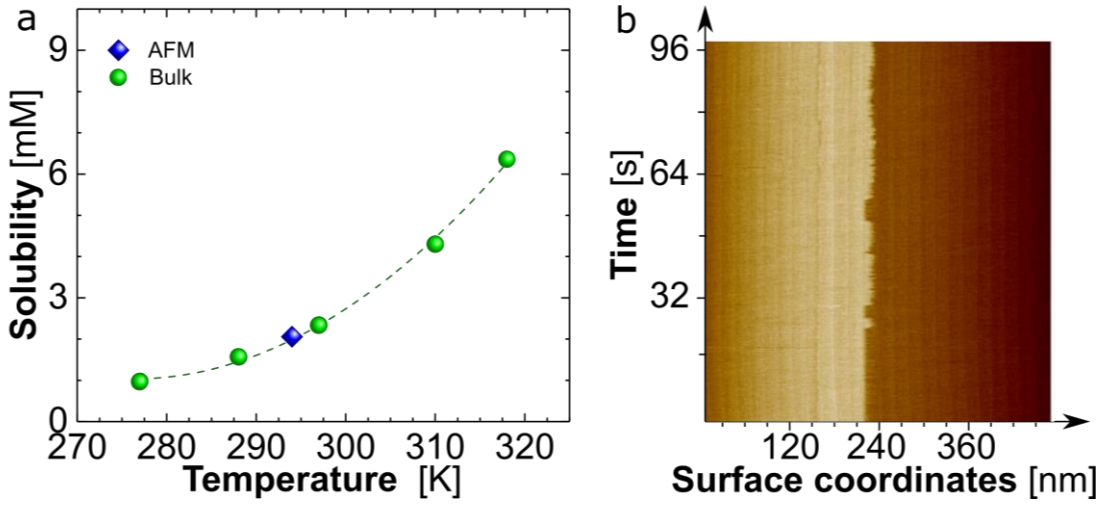

Figure 51 Comparison of the OZPN HE solubility measurements using bulk crystallisation experiment (green circles) and AFM measurements (blue square), b) In situ AFM image collected with a disabled Y axis at concentration 2.08 mM at 21°C In this imaging mode, the vertical axis represents time.

The resulting mean was used as the solubility C_e (Figure 38 a). The solubility measurements using AFM technique involve the observation of the behaviour of the step on the surface of OZPN HE to determine the solubility

concentration. At the solubility concentration, the step is neither growing nor dissolving, although some fluctuations of the molecules to and from the step are observed. To obtain such an image, during data collection the y-axis is disabled and the AFM tip moves only in the *x*-direction while the *y*-coordinate remain fixed and now represents time. Figure 51 shows a pseudoimage obtained in this mode. The image was collected for 100 s at concentration 2.08 mM and the AFM liquid cell of temperature 21°C Several fluctuations of the molecules from and to the step are visible, although no growth or dissolution of the steps take place. The data show good agreement between the solubility measured by two separate techniques: bulk crystallisation (2.05 mM) and in situ AFM (2.08 mM).

c) *Effect of impurities.*

No impurities were detected using NMR techniques and all NMR peaks were assigned to the OZPN structure (Figure 55).

6.2.5 Are preformed solute oligomers part of the incorporation mechanism?

Considering negligible effects of (*a*-*d*) factors described above, the presence of self-associates is considered, mainly OZPN dimers in OZPN solution, and the dependence of the step velocity, *v*, and on concentration, *C*, if dimers are present in the solution. Assume dimerization equilibrium:

$$2M \rightleftarrows D, \quad K_D = \frac{C_D}{C_M^2} \tag{34}$$

Where *M* is OZPN monomer, C_M is monomer concentration, *D* is OZPN dimer, C_D is dimer concentration, and K_D represents dimerization constant. The total concentration of OZPN *C* is equal to:

$$2C_D + C_M = C_{OZPN} \tag{35}$$

The concentration of dimers can be expressed as equation 36 and K_D is represented as in equation 37:

$$C_D = \frac{C_{OZPN} - C_M}{2} \tag{36}$$

$$\frac{C_{OZPN} - C_M}{2C_M^2} = K_D \tag{37}$$

After solving quadratic equation 38 the expression for the concentration of monomers (equation 39) and dimers (equation 40) in OZPN solution is obtained.

$$2K_D C_M^2 + C_M - C_{OZPN} = 0 \tag{38}$$

$$C_M = \frac{\sqrt{1+8K_D C_{OZPN}} - 1}{4K_D} \tag{39}$$

$$C_D = K_D C_M^2 = \frac{1}{16K_D}\left[\sqrt{1 + 8K_D C_{OZPN}} - 1\right]^2 \tag{40}$$

Four analytical models were derived[85,215] and summarised in Table 9 for scenarios where monomer and dimer species are present in solution at various proportions and take part in the growth mechanism. That combination gives us the following scenarios:

(i) monomers dominate in the solution and growth occurs by the presence of monomers;

(ii) monomers dominate in solution, although the growth occurs by OZPN dimers;

(iii) dimers dominate in solution and growth occurs by the dimers;

(iv) dimers dominate in solution but the growth occurs by the monomers.

(i) monomers dominate and growth occurs by incorporation of monomers

Recalling equation 39 and assuming that the concentration of dimers in solution is much lower than the concentration of monomers, i.e. $C_D << C_M$, the dimerization constant is $K_D << 1/C_M$, then $K_D C_M < 1$, applying approximation 42 and 43 $with\ x = 8K_D C_{OZPN}$

$$(1+x)^{1/2} \cong 1 + \frac{1}{2}x - \frac{1}{8}x^2 \tag{42}$$

$$\left[(1+x)^{\frac{1}{2}} - 1\right] \cong \frac{1}{2}\left[x - \left(\frac{x}{2}\right)^2\right] \cong \frac{x}{2} \tag{43}$$

The concentration of monomers is equal:

$$C_M = \frac{1}{8K_D} 8K_D C_{OZPN} = C_{OZPN} \tag{44}$$

A linear relationship is expected between step velocity, *v*, and OZPN concentration, which was described previously with equation 33 and follows trend *i* in Figure 52:

$$v = \beta\Omega_M(C_{OZPN} - C_e)$$

where Ω_M is a volume of a monomer.

(ii) *monomers dominate but growth occurs by incorporation of dimers.*

Recalling equation 40 and assuming that the concentration of dimers is much lower than the concentration of monomers $C_D << C_M$, the dimerization constant is $K_D << 1/C_M$, and $K_D C_M < 1$, $with\ x = 8K_D C_{OZPN}$, with approximation 45 and 46

$$(1+x)^{1/2} \cong 1 + \frac{1}{2}x - \frac{1}{8}x^2 \tag{45}$$

$$\left[(1+x)^{\frac{1}{2}} - 1\right]^2 \cong \frac{1}{4}\left[x - \left(\frac{x}{2}\right)^2\right]^2 \cong \frac{x^2}{4} \tag{46}$$

$$C_D = \frac{1}{16K_D}\frac{64K_D^2 C_{OZPN}^2}{4} = K_D C_{OZPN}^2 \tag{47}$$

This result is expected for $C_D \ll C_M$ since $C_M = C_{OZPN} - 2C_D \cong C_{OZPN}$. Thus,

$$C_D = K_D C_M^2 = K_D (C_{OZPN} - 2C_D)^2 \cong K_D C_{OZPN}^2 \tag{48}$$

The expression for step velocity on OZPN concentration is described by equation 49 and follows trend *ii* in Figure 52:

$$v = \beta \Omega_D K_D (C_{OZPN}^2 - C_e^2) \tag{49}$$

(iii) OZPN dimers dominate in the solution and growth occurs by incorporation of OZPN dimers.

Recalling equation 32 and assuming the concentration of dimers is much higher than concentration of monomers $C_D >> C_M$,

$$C_D = \frac{C_{OZPN}}{2} \tag{52}$$

The expression for step velocity on OZPN concentration is expressed by equation 49 and follows trend *iii* in Figure 52:

$$v = \frac{\beta \Omega_D}{2}(C_{OZPN} - C_e) \tag{49}$$

Since $\Omega_D/2$ is the volume of a monomer, this relationship is qualitatively and quantitatively indistinguishable from that for growth by incorporation of monomers.

(iv) *OZPN dimers dominate in solution, although the growth occurs by the incorporation of monomers,*

Recalling equation 39 and assuming that the concentration of dimers is much higher than the concentration of monomers, i.e. $C_D >> C_M$, then dimerization constant $K_D >> 1/C_M$, which gives $\sqrt{1 + 8K_D C_{OZPN}} > 1$

$$C_M = \frac{\sqrt{8K_D C_{OZPN}}}{4K_D} = \frac{1}{2}\sqrt{\frac{2C_{OZPN}}{K_D}} \tag{50}$$

The expression for step velocity on OZPN concentration is expressed with equation 51 and follows trend *iv* in Figure 52:

$$v = \beta \Omega_M \sqrt{\frac{1}{2K_D}}\left(\sqrt{C_{OZPN}} - \sqrt{C_e}\right) \tag{51}$$

Table 9 Summery table for the analytical models for correlation of step velocity, v, with concentration of monomers and dimers in solution. The equation describing a quadratic dependence between step velocity, v, and OZPN dimers, which are minor species in the solution, is shaded in grey

		Dominant solute species	
		Monomer	Dimer
Incorporating specie	Monomer	$v = \beta\Omega_M(C_{OZPN} - C_e)$	$v = \beta\Omega_M\sqrt{\frac{1}{2K_D}}\left(\sqrt{C}_{OZPN} - \sqrt{C_e}\right)$
	Dimer	$v = \beta\Omega_D K_D(C_{OZPN}^2 - C_e^2)$	$v = \frac{\beta\Omega_D}{2}(C_{OZPN} - C_e) = \beta\Omega_M(C_{OZPN} - C_e)$

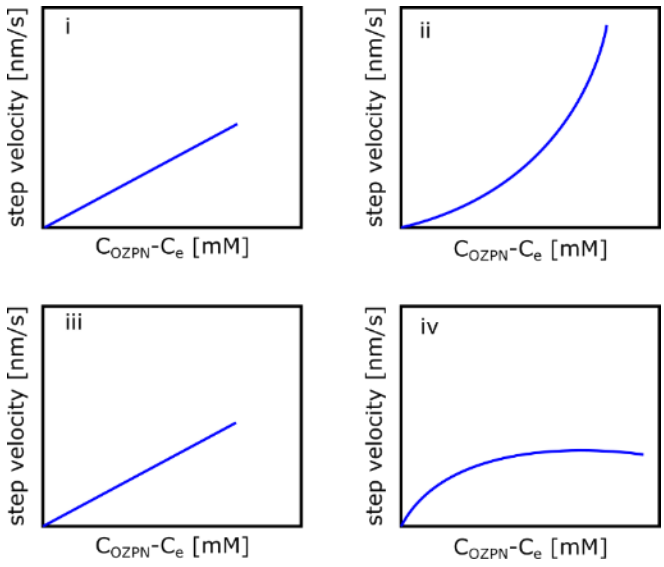

Figure 52 Step velocity dependence on OZPN concentration considering (i) monomers dominate in the solution and growth occurs by presence of monomers; (ii) monomers dominate in solution, the growth occurs by OZPN dimers; (iii) dimers dominate in solution and growth occurs by the dimers; (iv) dimers dominate in solution but the growth occurs by the monomers.

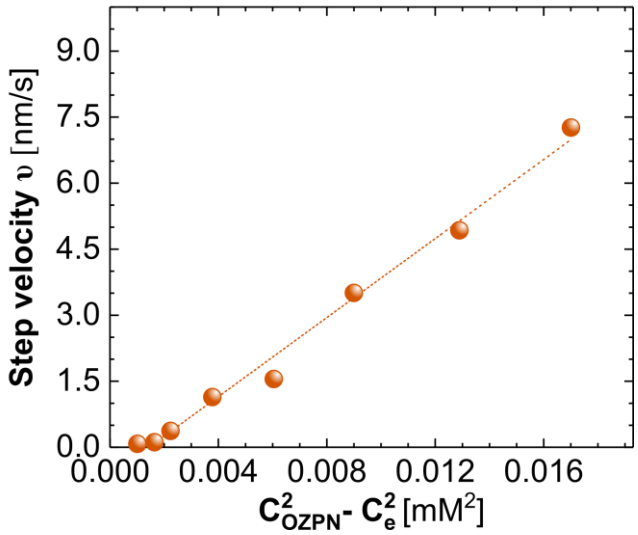

Figure 53 Step velocity, v, plotted in coordinates ($C_{OZPN}^2 - C_e^2$) showing linear dependence.

According to equation 49 incorporation of dimers from a solution rich in monomers results in a quadratic v(C_{OZPN}) dependence. Figure 53 shows a linear dependence on *v* (C_{OZPN}^2 - C_e^2) which is consistent with the model for growth by the incorporation of dimers in the presence of a majority of monomers.

6.2.6 Detection of OZPN dimers in solution.

All neat and solvated solid-forms of OZPN have SC_0 dimer present in the crystal structure, which is a strong indication that this dimer structure is formed in solution. SC_0 dimer is not a H-bonded dimer, however it is stabilized by three types of multiple C−H···π interactions (Figure 54): i) between piperazine C12 and thiophene C1-C2 fragment, ii) between piperazine C13 and thiophene C3-C11, iii) between piperazine C13, C14 and C17 the phenyl ring (multiple H· · ·π interactions)

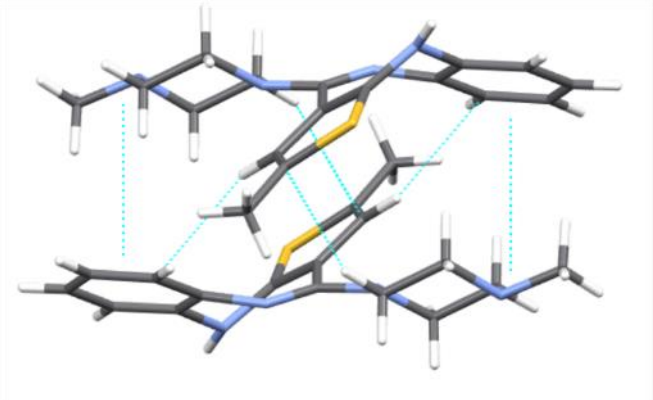

Figure 54 Multiple C-H-π interactions stabilizing SC_0 dimer visualised with Mercury software.

Self-association species can be detected in solution using with various spectroscopy methods including NMR, IR, and Raman. [65–67,100–102,105] The structure of OZPN self-associates was examined in three solvents of different polarity 1/1 EtOD/D_2O, Acetone-d_6, and $CDCl_3$, Figure 55 presents the OZPN NMR spectra in these solvents with assigned NMR signals.

Crystallisation of OZPN from 1/1 EtOH/H_2O, acetone and chloroform gives crystal structures with various arrangement of SC_0 dimers,[7,62] ^{1}H NMR concentration dependent studies of OZPN in 1/1 EtOD/D_2O and acetone-d_6 did not show any changes in chemical shifts (Figure 56 and Figure 57). The accessible concentration range is narrower due to low OZPN I solubility in these solvents (exact data not available). This does not exclude the possibility that OZPN dimers may form in supersaturated solutions in these solvents. A much wider range of concentrations is accessible for OZPN chloroform solutions.

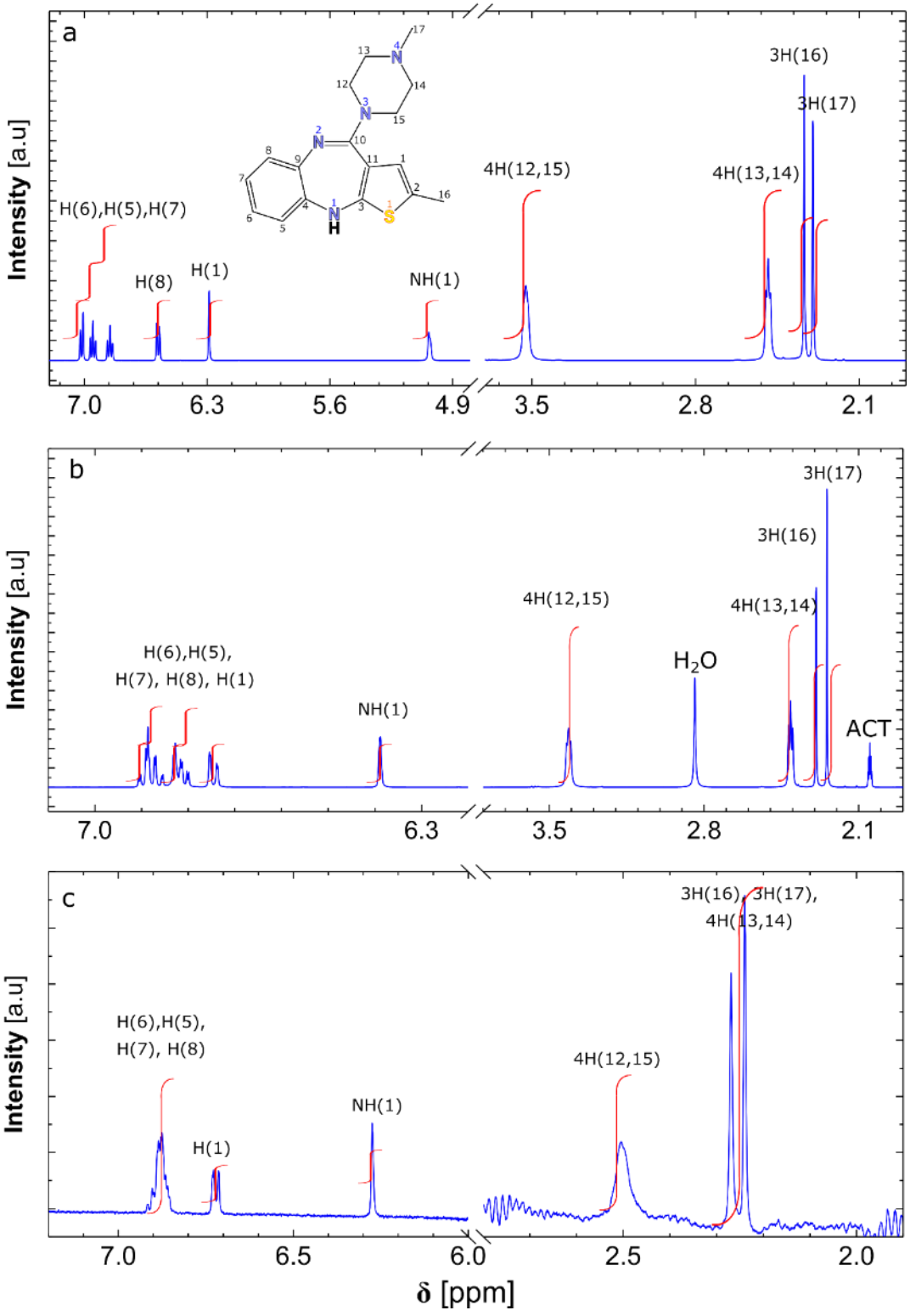

Figure 55 NMR spectra with assigned protons for OZPN molecule in a) chloroform-d, inset OZPN molecule with numbered protons, b) acetone-d_6, and c) 1/1 EtOD/D_2O.

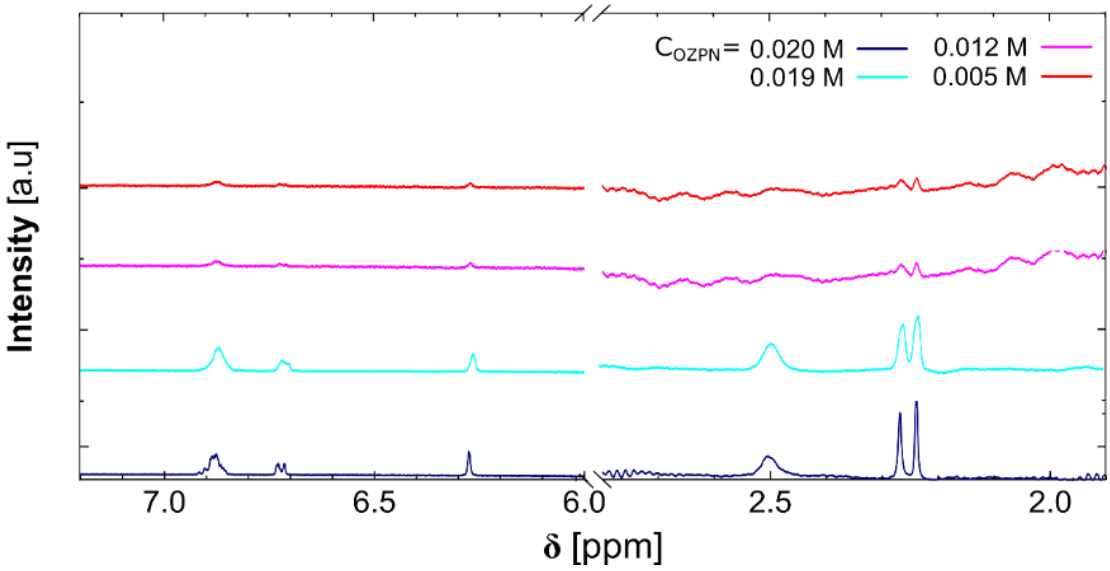

Figure 56 Concentration dependent ^{1}H NMR spectra for OZPN in 1/1 EtOH/D_2O at RT.

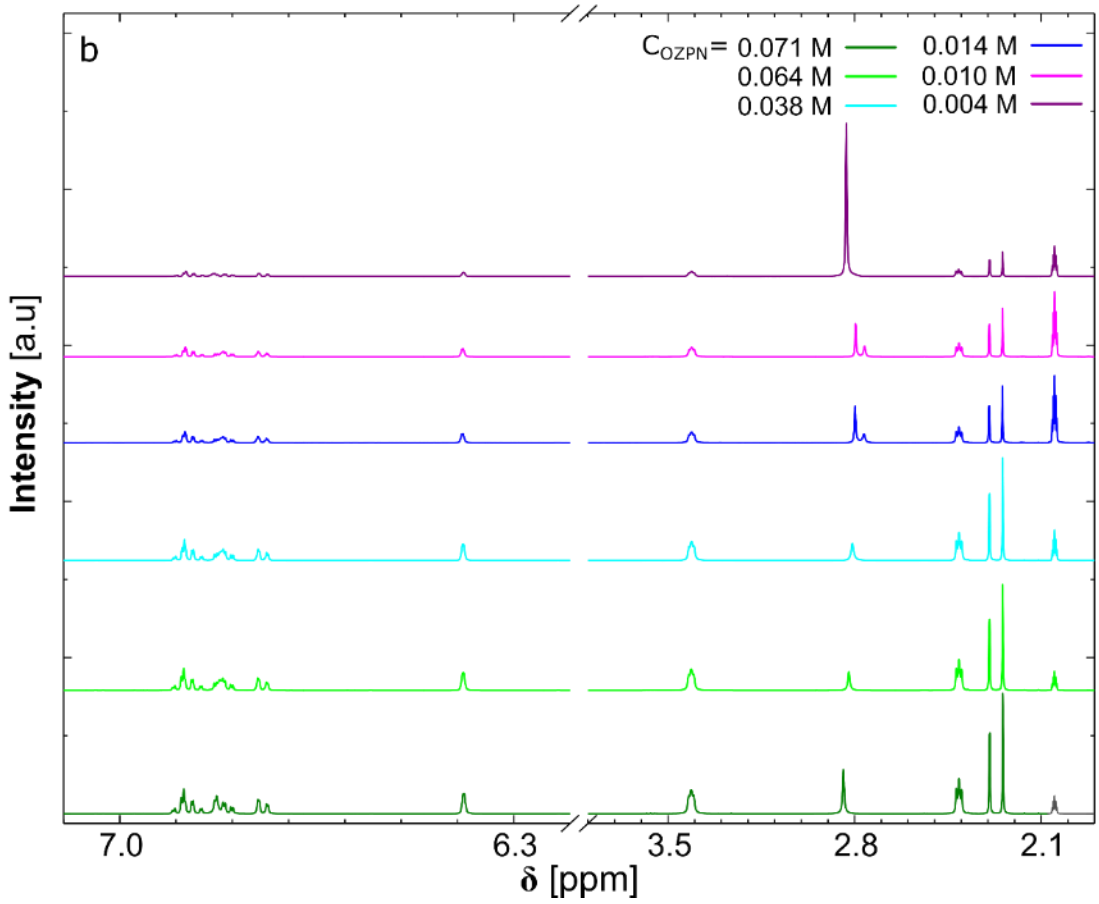

Figure 57 Concentration dependent ^{1}H NMR spectra for OZPN in acetone-d_6 at RT.

^{1}H NMR dilution data in $CDCl_3$ (Figure 58 a, Table 10) show concentration dependent changes in chemical shift suggesting association of OZPN molecules into a molecular complex. There is an up-field shift of all piperazine protons (CH12, 13, 14, 15), methyl group of thiophene ring (CH16) and aromatic protons (CH8) (marked in Figure 58 b) with increasing OZPN concentration. Complex induced shifts (CIS) are an indication of either single equilibrium of self-association of OZPN molecules into a dimer or a competition between multiple structures. The number of self-association species can be estimated from the shape of normalised dilution curves.[65,67] If there are many competitive complexes formed the shifts in the NMR spectrum will be a result of a fast exchange of protons between these complexes and dilution curves will not follow the same trend. The dilution curves for OZPN in $CDCl_3$ (Figure 58 c) follow the same fashion and indicate that only one complexation process takes place in this solvent.

Table 10 NMR shifts for OZPN protons in $CDCl_3$ with decreasing concentration. Only signals shifted more than 0.01 ppm are considered to have significant shift.

	Peak position									
C_{OZPN} [M]	CH (12,15)	CH (13,14)	CH_3 (16)	CH_3 (17)	CH (6)	CH (5)	CH (7)	CH (8)	CH (1)	NH (1)
0.206	3.52	2.49	2.33	2.30	7.02	6.96	6.85	6.59	6.29	5.03
0.169	3.52	2.49	2.33	2.30	7.03	6.96	6.86	6.59	6.29	5.03
0.087	3.53	2.50	2.35	2.30	7.03	6.96	6.87	6.60	6.29	4.99
0.023	3.62	2.59	2.40	2.31	7.04	6.96	6.88	6.63	6.29	5.03

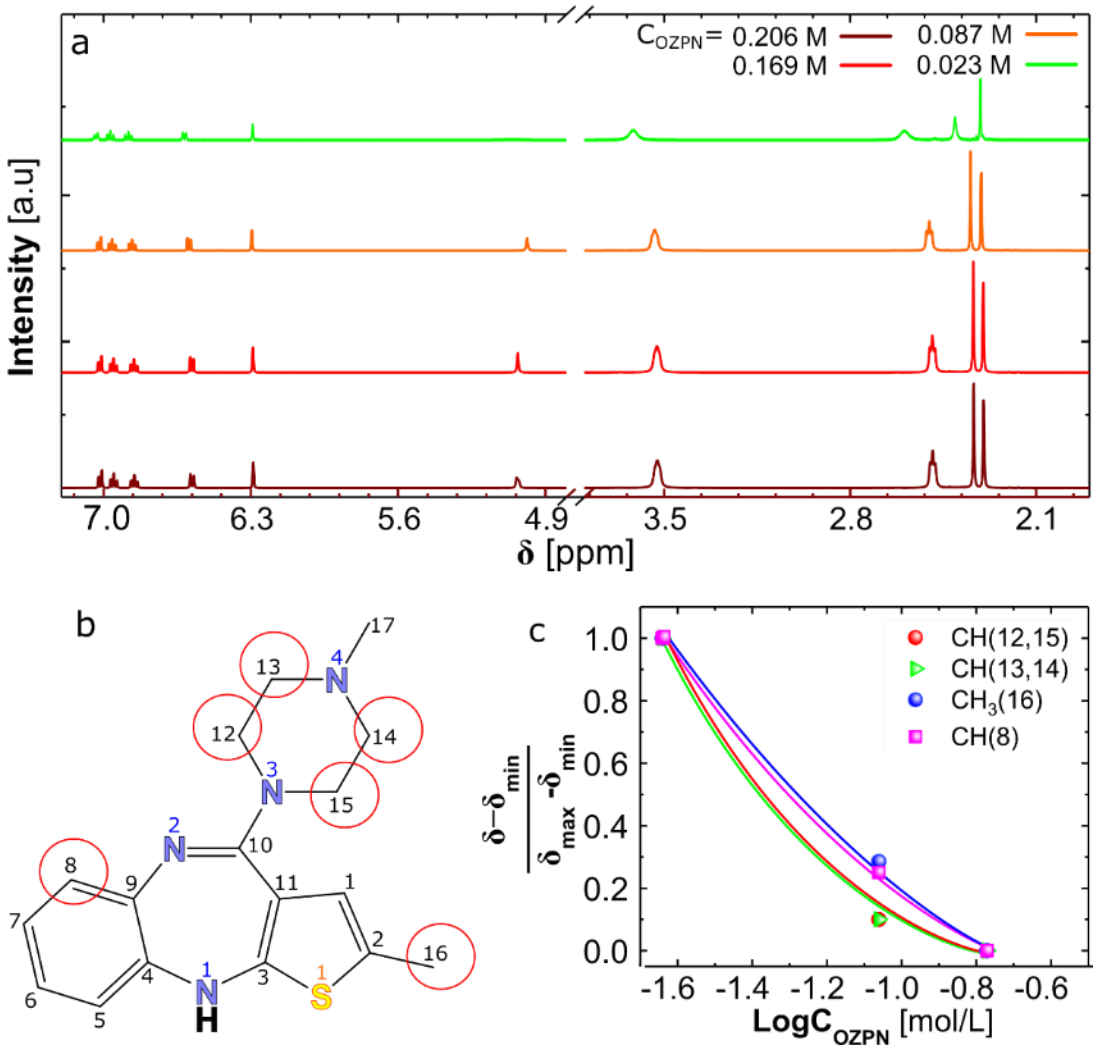

Figure 58 Evidence of the dimer formation in $CDCl_3$ a) concentration dependent ^1H NMR spectra for OZPN in chloroform at 25°C, b) structure of OZPN molecules with marked protons that show significant complex induced shift, c) Normalised changes in chemical shift observed for OZPN protons as a function of concentration in $CDCl_3$ solution at RT. Lines are guides for the eye.

The observed shifts of all piperazine protons, the methyl group of the thiophene ring and aromatic protons indicate multiple π─C─H interactions between OZPN molecules, corresponding to those observed in the structure of SC_0 dimer (Figure 54). Based on this observation it is concluded that SC_0 dimer is formed in chloroform solution. To further examine the formation of the SC_0 dimer, vibrational spectroscopy was applied. This technique is often used to study the correlation between solution

chemistry and solid-state chemistry[69,70,100] and allows wider range of concentration to be measured including saturated and supersaturated solutions. Raman concentration-dependent spectra of OZPN in chloroform and EtOH/H_2O and corresponding solid-forms are presented in Figure 59. Solid forms of both OZPN chloroform (Figure 59 a) and OZPN HE (Figure 59 b) solvates show similar Raman spectrum with characteristic peaks in the region 1500-1600 cm^{-1} corresponding to three group of bonds. 1) stretching νC=C of benzene ring, 2) stretching νC=C of thiophene ring and 3) stretching νC=N coupled with bending δNH deformations of diazepine ring and bending of thiophene δCH_3. Peak at 1050 cm^{-1} corresponding to twisting γCH_2 and rocking ρCH_3 deformation of piperazine ring.[130] Chloroform solutions measured within the same concentration range as solutions measured by NMR are presented in Figure 59 a. For concentrated solutions (0.087 M and above) the solution Raman spectrum resembles the solid-state spectrum for the chloroform solvate with both the position and intensities of the main double peak at 1600 cm^{-1} and single peak at 1050 cm^{-1} suggesting the presence of similar OZPN conformations both in concentrated OZPN solution and OZPN chloroform solvate crystal - SC_0 dimer. Below 0.023 M concentrations the double peak at 1600 cm^{-1} decreases in intensity while peaks between 1300-1400 cm^{-1} increase. These peaks correspond to bending of both methyl groups δCH_3 and methylene groups δCH_2 of piperazine ring .[130] These observation correlate to NMR data suggesting that in concentrated chloroform solutions OZPN associates into SC_0 dimers. Similar behaviour was observed for EtOH/H_2O solutions. Diluted solutions show peaks at 1050 cm^{-1} corresponding to OZPN monomers, although the peak at 1600 cm^{-1} is more pronounced at 0.043 M concentration indicating the formation of SC_0 dimer in supersaturated EtOH/H_2O solution. The full association of

OZPN dimers was not detected for EtOH/H_2O, suggesting that dimers formed stay in a minority.

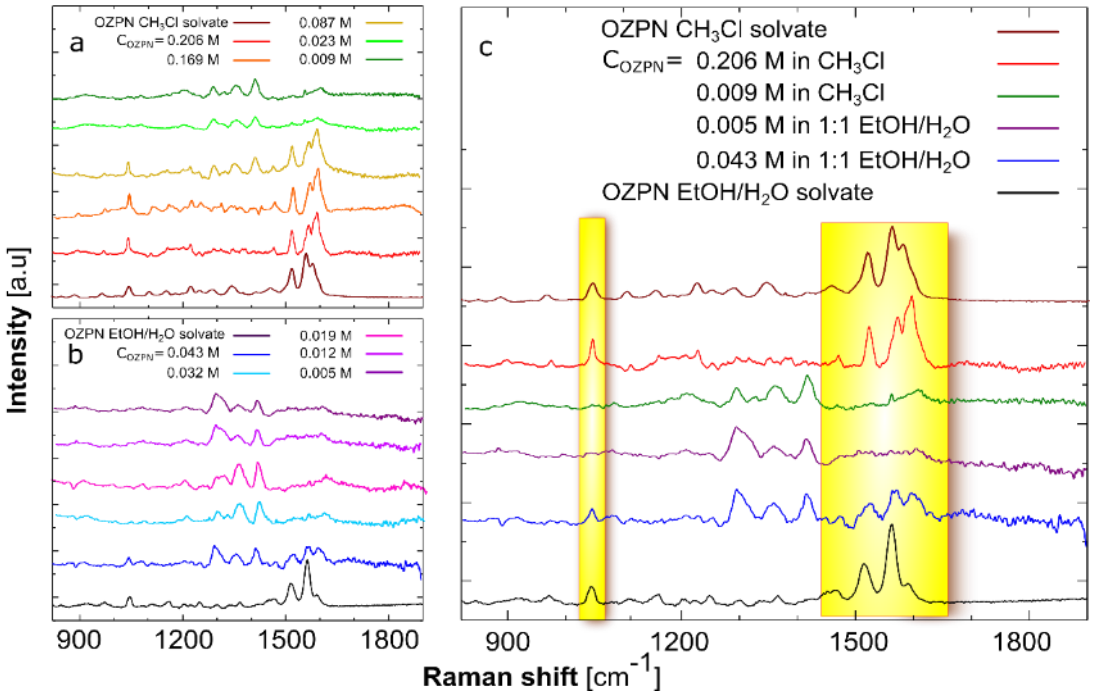

Figure 59 Measured Raman spectra for OZPN in a) chloroform, b) EtOH/H_2O, c) comparison between diluted and concentrated solution of OZPN in chloroform and EtOH/H_2O.

The Materials Studio DMol[3] COSMO[121] solvation model was used to model the Raman spectra for OZPN monomer and dimer in chloroform, water and EtOH. The spectra obtained show no significant dependence on the solvent used. Spectra for the OZPN monomer (Figure 60 a) show Raman peak between 1000-1500 cm^{-1}, while spectra for dimer show peaks around 1500-1600 cm^{-1} (Figure 60 b). This is in good agreement with experimental spectra (Figure 60 c).

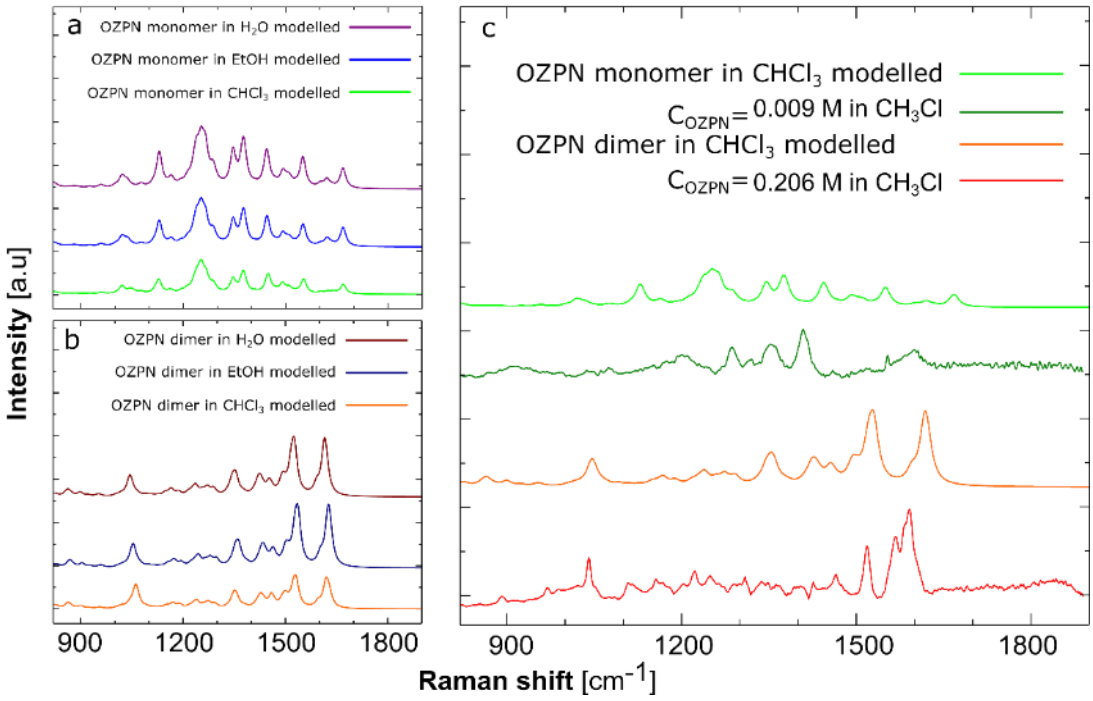

Figure 60 DMol³ modelled Raman spectra for a) OZPN monomer in water, ethanol and chloroform, b) OZPN dimer in water, ethanol and chloroform, c) comparison between measured diluted (0.009 M) chloroform solution and concentrated (0.206 M) chloroform solution.

6.3 Discussion

6.3.1 Possible pathways from solution to a crystal

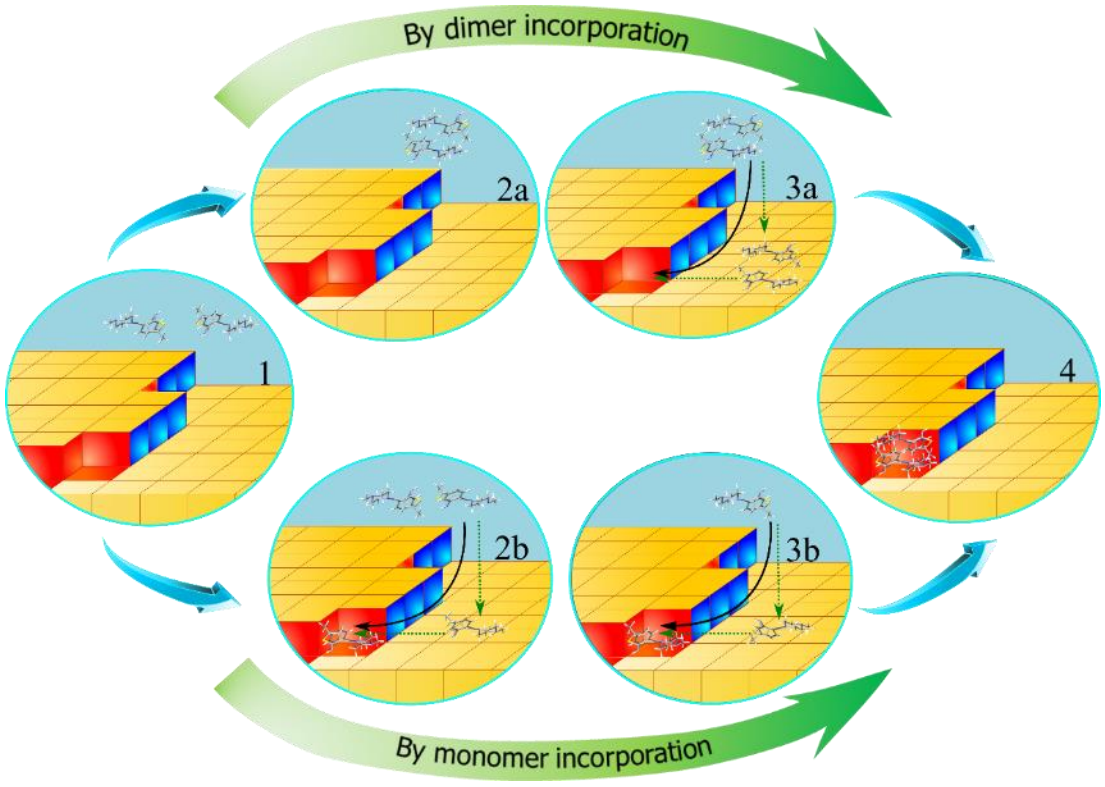

Figure 61 Possible pathways for OZPN HE crystal growth. Growth by dimer incorporation of 1) OZPN dimers present in supersaturated solution, 2a) self-association of OZPN dimers in solution, 3a) direct docking of the dimer to the kink (black arrow) or adsorption of the dimer at the terrace followed by surface diffusion (green dotted arrows) resulting in 4) OZPN dimer incorporation into the crystal structure. Growth by incorporation of monomers: 1) OZPN monomers present in supersaturated solution, 2b) direct incorporation of a OZPN monomer (black arrow) or adsorption of a monomer at the terrace followed by surface diffusion (green arrow) to a kink site, 3b) second monomer incorporated at the kink site resulting in OZPN dimer formation at the kink, 4) dimer incorporated into the crystal structure.

The growth of OZPN HE crystal layers occurs via single or multiple spiral dislocations with non-linear dependence of the step velocity on the solute concentration. Analysing the relationship between step velocity v assumes the presence of monomer and/or dimers in solution, the non-linear dependence suggests growth by OZPN SC_0 dimers that are in the minority in bulk OZPN solution compared with monomers. The

fundamental question is why the incorporation of dimers (Figure 61 a) is kinetically favoured over the incorporation of monomers (Figure 61 b) that are the main component of OZPN solution. This is discussed in the following section from consideration of the thermodynamics of solution, solvation growth units and surface integration mechanism.

6.3.2 Direct incorporation of monomers and dimers from solution to the kink

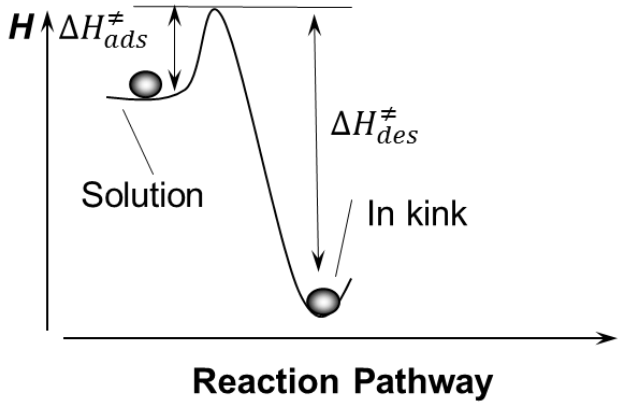

Figure 62 Enthalpy profile for molecule during direct incorporation into a step. $\Delta H_{ads}^{\neq}$ is kinetic barrier for incorporation and $\Delta H_{des}^{\neq}$ is kinetic barrier for detachment of a molecule from a growth site. Adopted from reference.[87]

Molecules can enter the crystal either by direct incorporation[86] from the solution to a kink (Figure 62) or by a surface diffusion mechanism (Figure 65).[87–89] During direct incorporation from solution to a kink site a molecule encounters a single energy barrier that takes into account multiple factors, including the orientation of the molecule, the geometry of the site, and the displacement of solvent. The kinetics of these processes will mainly depend on diffusivity of molecules in the solution and incorporation of the molecules to the kink and it is expressed by a kinetic coefficient for adsorption from bulk solution $\beta_{ads} = D/\Lambda$,[87] where D is the diffusivity of the OZPN molecules from solution and Λ is a resistance to enter the step from a bulk

solution in a units of length. Considering that monomers are a major component of the solution, while dimers are in the minority, comparing the molecular volume Ω and diffusivity D of monomers and dimers contributing to the step velocity derived from equation 31, a rough estimation expressed by equation 52 and 53 is obtained:

$$v_M = \frac{D_\mathrm{M}\Omega_\mathrm{M}}{\Lambda_\mathrm{M}}(C_{OZPN} - C_e) \approx \frac{D_\mathrm{M}\Omega_\mathrm{M}}{\Lambda_\mathrm{M}} C_M \tag{52}$$

$$v_D = \frac{D_D\Omega_\mathrm{D}}{\Lambda_\mathrm{D}} K_D(C_{OZPN}^2 - C_e^2) \approx \frac{D_D\Omega_\mathrm{D}}{\Lambda_\mathrm{D}} K_D C_M^2 \approx \frac{D_D\Omega_\mathrm{D}}{\Lambda_\mathrm{D}} C_D \tag{53}$$

Where the volume for the dimer is twice the volume of the monomer, $\Omega_D = 2\Omega_M$, the diffusivity of molecules from solution D for dimer is less than for the monomer, $D_D < ½ D_M$. Since the concentration of monomers is much higher than the concentration of dimers in solution, the greater dimer volume and stronger (quadratic) concentration dependence does not compensate for much higher concentration of monomers and do not favour faster growth by dimers (equation 54).

$$D_\mathrm{M}\Omega_\mathrm{M} \approx D_D\Omega_\mathrm{D} \text{ and } \quad C_M \gg C_D \tag{54}$$

Faster growth by dimer growth units must be due to a greater kinetic coefficient $\Lambda_\mathrm{D}^{-1} \gg \Lambda_\mathrm{M}^{-1}$. Λ^{-1} is proportional to an energy barrier that a molecule needs to overcome before it is incorporated into to the kink and it is expressed with equation 55:[203]

$$\Lambda^{-1} \approx \exp\left(\frac{\Delta S^{\neq}}{R}\right) \exp\left(-\frac{\Delta H^{\neq}}{RT}\right) \tag{55}$$

Where $\Delta S^{\neq}$ and $\Delta H^{\neq}$ are the entropy and enthalpy change of the transition state, respectively. The entropy change of the transition state can be expressed as the

difference between the entropy of the transition state $S^{\neq}$ and the entropy of the solution $S_{solution}$, equation 56:[177]

$$\Delta S^{\neq} = S^{\neq} - S_{solution} \tag{56}$$

The entropy of solution contains four components: molecular translation, rotation, intramolecular and intermolecular interaction between molecules included in equation 57:

$$S_{solution} = S_{translation} + S_{rotation} + S_{intermolecular} + S_{intramolecular} \tag{57}$$

Both $S_{intermolecular}$ and $S_{intramolecular}$ can be ignored since their values for the solutions are insignificant. The key components are $S_{translation}$ expressed with equation 58 and $S_{rotation}$, which is expressed with equation 61:[177]

$$S_{translation} = k_B \ln q_{translation} + k_B T \left(\frac{\partial \ln q_{translation}}{\partial T}\right)_V \tag{58}$$

where $q_{translation}$ is a molecular partition function defined by equation (59):

$$q_{translation} = \left(\frac{2\pi m k_B T}{h^2}\right)^{\frac{3}{2}} \tag{59}$$

Considering that $m_D = 2m_M$, the translation entropy lowers the dimer kinetic coefficient owing to contributions from mass (Equation 60):

$$\exp\left(\frac{\Delta S^{\neq}}{R}\right)_{Dimer} \approx 2^{-\frac{3}{2}} \exp\left(\frac{\Delta S^{\neq}}{R}\right)_{Monomer} = 0.35 \exp\left(\frac{\Delta S^{\neq}}{R}\right)_{Monomer} \tag{60}$$

The $S_{rotation}$ expressed with equation 61:[177]

$$S_{rotation} = k_B \ln q_{rotation} + k_B T \left(\frac{\partial \ln q_{rotation}}{\partial T}\right)_V \quad (61)$$

where $q_{rotation}$ is a molecular partition function defined by equation (62):

$$q_{rotation} = \frac{\pi m^{\frac{3}{2}} \Omega}{\sigma} \left(\frac{8\pi k_B T}{h^2}\right)^{\frac{3}{2}} \quad (62)$$

Where σ is the order of symmetry, $\sigma = 1$ for monomer, $\sigma = 2$ for dimer, $\Omega_D = 2\Omega_M$, $m_D = 2m_M$. In common with translational entropy, rotational entropy lowers the dimer kinetic coefficient owing to contributions from a greater volume and mass, partially compensated by higher symmetry (Equation 63):

$$\exp\left(\frac{\Delta S^{\neq}}{R}\right)_{Dimer} \approx 2^{-\frac{3}{2}} \exp\left(\frac{\Delta S^{\neq}}{R}\right)_{Monomer} = 0.35 \exp\left(\frac{\Delta S^{\neq}}{R}\right)_{Monomer} \quad (63)$$

This assessment depicts the conclusion that faster growth by dimer unit is not due to the translational $S_{translation}$ or rotational entropy $S_{rotation}$ that lowers Λ^{-1}, but must be owing to lower $\Delta H^{\neq}$, which will now be considered.

The removal process of strongly bounded water molecules structured around the solute molecules and at the growth sites has been identified as a significant contributor to the $\Delta H^{\neq}$.[201] The solvation of OZPN monomers and dimers was investigated with ORIENT[145] by considering the interaction of OZPN monomers and dimers with one or more water molecules. An OZPN molecule can be considered as having two sides: the front (Figure 63 right) is largely hydrophobic, and the back (Figure 63 left). Both sites have hydrogen bond donors (N1) and acceptors (N2 and N4).

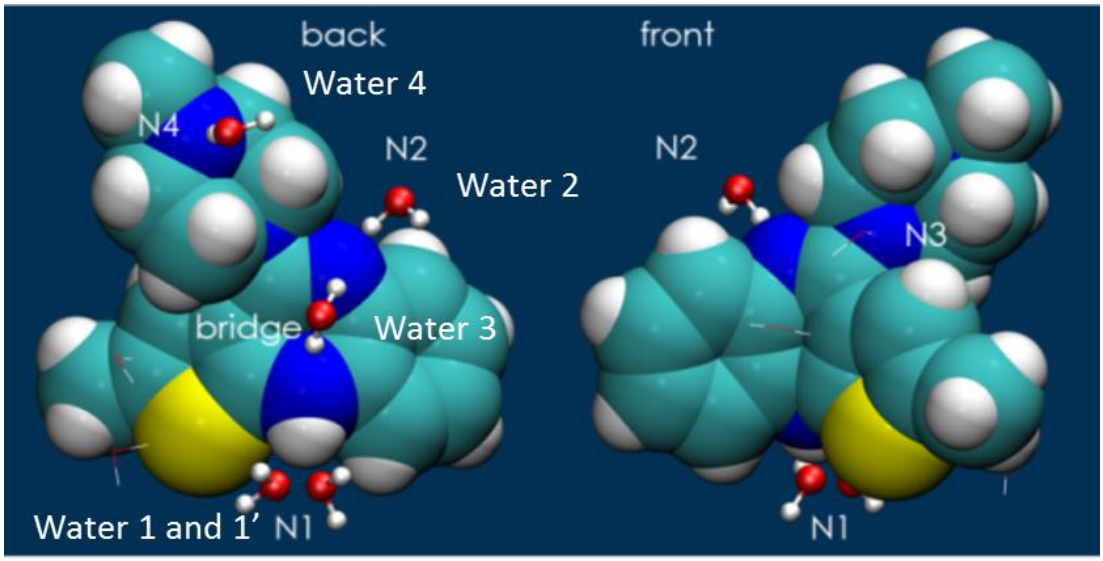

Figure 63 Solvent binding to OZPN a) monomer and b) dimer in a crystal structure of OZPN HE. Copied from reference.[145]

When forming the SC_0 dimer, two OZPN molecules will hide the hydrophobic front sides of the two molecules, yet keeping the hydrophilic back exposed and providing five strong water-binding sites (two on N1, one on N2, one on N4, and a bridge site). Hydration of an SC_0 dimer was investigated with ORIENT, leading to an interaction spectrum shown in Figure 64.

All strong water binding sites found in the OZPN monomer hydration were also found in the hydration of an SC_0 dimer and their release slows incorporation of dimers and monomers equally, therefore the process of removing strongly bound water also does not contribute to a faster growth of crystal growth by incorporation of OZPN dimers.

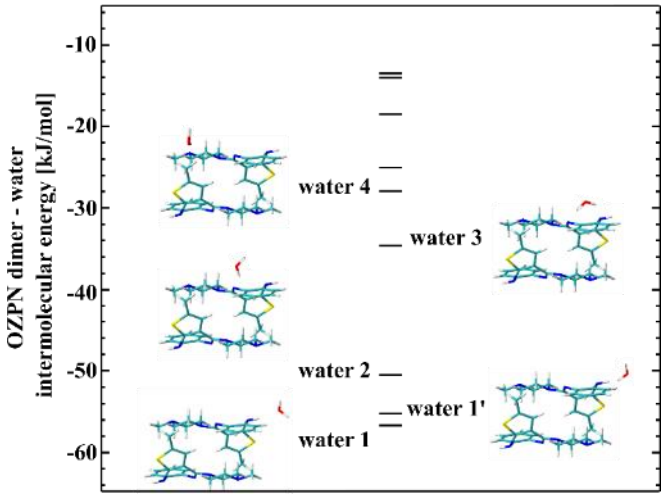

Figure 64 Interaction energies and configurations of water-SC_0 dimer complex. Adopted from reference.[145]

6.3.3 Surface diffusion of monomers and dimers to the kink

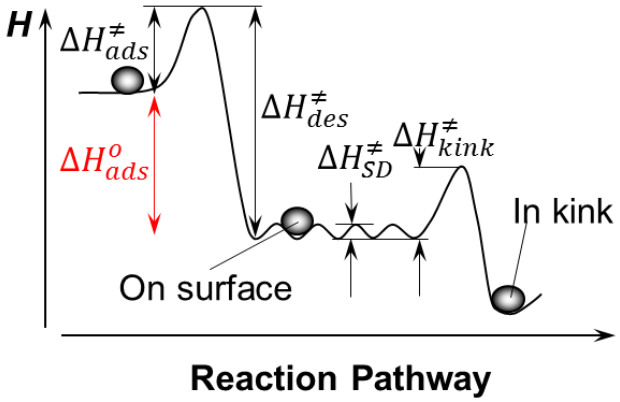

Figure 65 Enthalpy profile for a molecule diffusing toward a step via the surface diffusion mechanism with kinetic barriers for adsorption on a terrace $\Delta H^{\neq}_{ads}$, desorption $\Delta H^{\neq}_{des}$, diffusion along the surface toward a step $\Delta H^{\neq}_{des}$, and, attachment to a growth site $\Delta H^{\neq}_{kink}$. Adopted from reference. [90]

Taking into consideration direct incorporation of the molecules from the solution to a kink site it was not possible to identify a key thermodynamic factor that significantly contributes to the faster growth of OZPN HE crystals by dimer incorporation. Therefore, the surface diffusion mechanism will now be considered and its various

components will be analysed taking into consideration OZPN monomer and dimer growth units.

Assuming a surface diffusion mechanism, the dependence of the step velocity on supersaturation, step spacing, and rate of diffusion through the solution boundary layer for the crystal growth from solution is expressed by the Gilmer, Ghez and Cabrera (GGC) model.[216] In the case where the diffusion of solute from bulk solution toward the crystal interface is not a limiting factor for step motion, the step velocity can be expressed as equation 64 and based on equation 55 it is proportional to an energy barrier that a molecule needs to overcome before incorporation to the kink (Figure 65).[88,89]

$$v = \frac{\lambda}{h}\frac{\Omega D}{\Lambda}(C_{OZPN} - C_e)\left(\frac{\Lambda_s}{\lambda} + \frac{1}{2}coth\frac{l}{2\lambda}\right)^{-1} \propto exp\left(\frac{\Delta S^{\neq}}{R}\right)exp\left(-\frac{\Delta H^{\neq}}{RT}\right) \qquad (64)$$

where h is step height, λ is the characteristic length of surface diffusion, *D* is the bulk diffusion, Λ is a resistance to enter the step from a bulk solution in length units, Λ_s is the resistance for incorporation into kinks from the surface, also measured as length. All of the components contribute to the total enthalpy change in a following way (Equations 65–68):[85,90]

$$\lambda = a\exp\frac{\Delta H^{\neq}_{des} - \Delta H^{\neq}_{SD}}{2k_BT} \qquad (65)$$

$$D = D_0\exp\left(-\frac{E_{BD}}{k_BT}\right) \qquad (66)$$

$$\Lambda = a\exp\frac{\Delta H^{\neq}_{ads} - E_{BD}}{k_BT} \qquad (67)$$

$$\Lambda_s = a \exp \frac{\Delta H_{kink}^{\neq}}{k_B T} \quad (68)$$

where $\Delta H_{ads}^{\neq}$ is the kinetic barrier for adsorption on a terrace, $\Delta H_{des}^{\neq}$ is the kinetic barrier for desorption, $\Delta H_{SD}^{\neq}$ is a kinetic barrier for diffusion along the surface toward a step, and $\Delta H_{kink}^{\neq}$ is a kinetic barrier for attachment of a growth unit to a growth site, E_{BD} is the energy barrier of the bulk diffusivity.

All of these processes contribute to the total enthalpy change $\Delta H^{\neq}$ (Equation 69) during incorporation of molecules from the solution to the kink for the surface diffusion pathway: [87,90]

$$\Delta H^{\neq} \cong \Delta H_{ads}^{\neq} - \Delta H_{des}^{\neq} + \Delta H_{SD}^{\neq} + \Delta H_{kink}^{\neq} \quad (69)$$

$$\Delta H_{ads}^{o} = \Delta H_{des}^{\neq} - \Delta H_{ads}^{\neq} \quad (70)$$

$$\Delta H^{\neq} \cong \Delta H_{ads}^{0} + \Delta H_{SD}^{\neq} + \Delta H_{kink}^{\neq} \quad (71)$$

ΔH_{ads}^{o} is an equilibrium entropy of the molecules adsorbed on the terrace (equation 63) and it is a major contributor to $\Delta H^{\neq}$ (Figure 65).

As mentioned in section 6.2.4 there was no significant influence on step velocity for the steps with separation $\ell \geq 250$ nm taken into consideration for determining the relation between the step velocity and C_{OZPN}. The surface diffusion mechanism is strongly distinct for the groups of closely spaced steps that move significantly slower than well-separated steps. Figure 66 shows the evolution of several terraces on OZPN HE crystals at concentration C_{OZPN} - C_e = 3.31 mM with strong asymmetry between closely spaced and well-separated steps.

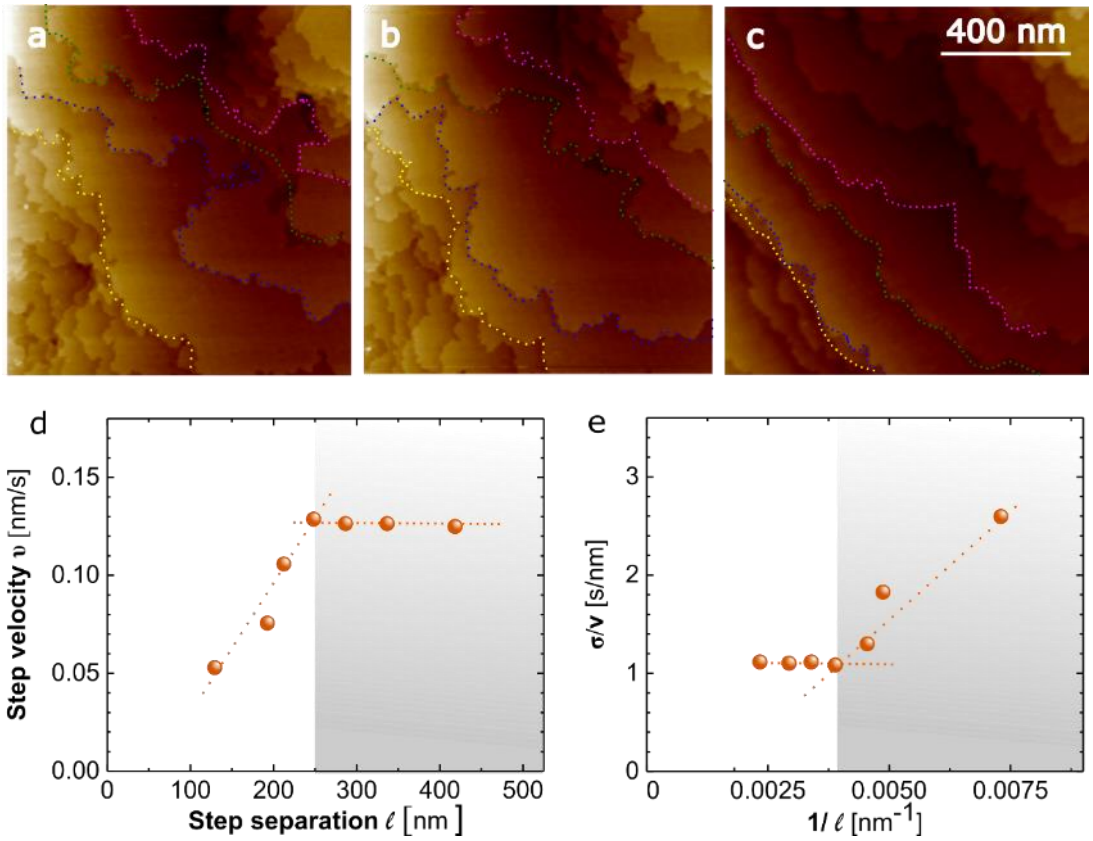

Figure 66 Evidence for surface diffusion mechanism for OZPN HE crystals. Asymmetry of the incorporation of the OZPN molecules into steps from the sides of the adjacent terraces: a) the yellow step grows slower comparing to the blue step, b) growth of the blue step slows down after reaching the yellow step, while c) well-separated steps (green and pink) grow significantly faster comparing to closely separated steps (yellow and blue), d) The step velocity, v, slows down at ℓ < 250 nm, highlighted by shading, e) the same data in (d) is replotted using coordinates [σ/v](1/ ℓ), where σ =(C_{OZPN} − C_e)/C_e. Shaded area corresponds to the one in d).

The terrace marked with blue dotted line (Figure 66 b) moves significantly faster than lower terrace marked with a yellow dotted line compared to their initial positions (Figure 66 a). This indicates that the supply of solute to the yellow terrace from a lower, much shorter ($\ell \approx 50$ nm) terrace is insufficient in contrast to a sufficient supply of the solute for a blue terrace provided by longer ($\ell \approx 200$ nm) yellow terrace. Now the blue terrace has a sufficient width to accommodate an adequate amount of the solute that will later diffuse and contribute to a growth of the green terrace. In turn, the green

terrace provides the supply of solute for the pink terrace to grow (Figure 66 c). These combined observations reveal strong asymmetry in the incorporation of molecules into closely spaced and well-separated steps. Such asymmetry would be negligible if molecules reach the steps directly from the solution.

Equation 64 can be written for two extreme cases when $\ell \gg 2\lambda$, where $\coth(l/2\lambda) \cong 1$ (Equation 73), and when $\ell \ll 2\lambda$, where $\coth(l/2\lambda) \cong 2\lambda/l$ (Equation 74) when σ is defined with Equation 72:

$$\sigma = (C_{OZPN} - C_e)/C_e \tag{72}$$

$$\frac{\sigma}{v} = \frac{h\Lambda}{\lambda\Omega C_e D}\left[\frac{\Lambda_e}{\lambda} + \frac{1}{2}\right] = \frac{1}{\Omega C_{e\beta}} \quad \text{, for } \ell >> 2\lambda \tag{73}$$

$$\frac{\sigma}{v} = \frac{h\Lambda\Lambda_s}{\lambda^2\Omega C_e D} + \frac{\Lambda}{\Omega C_e D}\frac{h}{l} \quad \text{, for } \ell << 2\lambda \tag{74}$$

If the surface diffusion mechanism operates, equation 73 indicates a constant value for the $[\sigma/v](1/\ell)$ at high values of ℓ, and according to equation 74, σ/v should increase linearly with $1/\ell$ at low values of ℓ. The data for OZPN HE in Figure 66 c fulfil both requirements for the surface diffusion growth pathway. The value of ℓ can be calculated from the intersection of lines in Figure 66 c. As $\ell = 2\lambda$, for OZPN, the characteristic length of surface diffusion λ = 120 nm. This asymmetric incorporation confirms step growth via adsorption on the terraces and surface diffusion.[87–89]

6.3.4 Determination of ΔH^o_{ads} for OZPN monomer and dimer

Since ΔH^o_{ads} is an equilibrium entropy of the molecules adsorbed on the terrace (equation 63) and it is a major contributor to $\Delta H^{\neq}$ (Figure 65), Monte Carlo molecular simulations were performed using an Adsorption Locator[217] module in Materials Studio 7.0 to obtain the energy barrier, $U_{ads,}$. It is assumed U_{ads}= ΔH^o_{ads} (at constant pressure and volume).[177]A rigid OZPN monomer and OZPN dimer was docked onto $(002)_{\text{OZPN HE}}$ step model by energy optimization, starting from random initial positions above the surface. During the course of the simulation, the dimer and monomer molecules are randomly rotated and translated around the substrate and adsorb to different sites on the surface. The simulations of adsorption sites on the $(002)_{\text{OZPNHE}}$ surface showed that a multitude of sites exist at various positions none of which were the ideal crystallographic positions. Figure 67 shows a snapshot of the lowest energy configurations obtained for a dimer and a monomer with calculated adsorption enthalpy for OZPN dimer $\Delta H^o_{ads\ dimer}$= -861 kJ/mol and for OZPN monomer $\Delta H^o_{ads\ monomer}$ = -606 kJ/mol. This result suggests that lower ΔH^o_{ads} leads to lower $\Delta H^{\neq}$ and, in consequence based on equation 64, faster growth. The difference between $\Delta H^o_{ads\ monomer}$ - $\Delta H^o_{ads\ dimer}$ = 255 kJ/mol. Since OZPN molecules reach the kinks from a layer of adsorbed molecules on the crystal terrace, crystal growth by dimers will be a faster due to higher population of dimers on the crystal terrace.

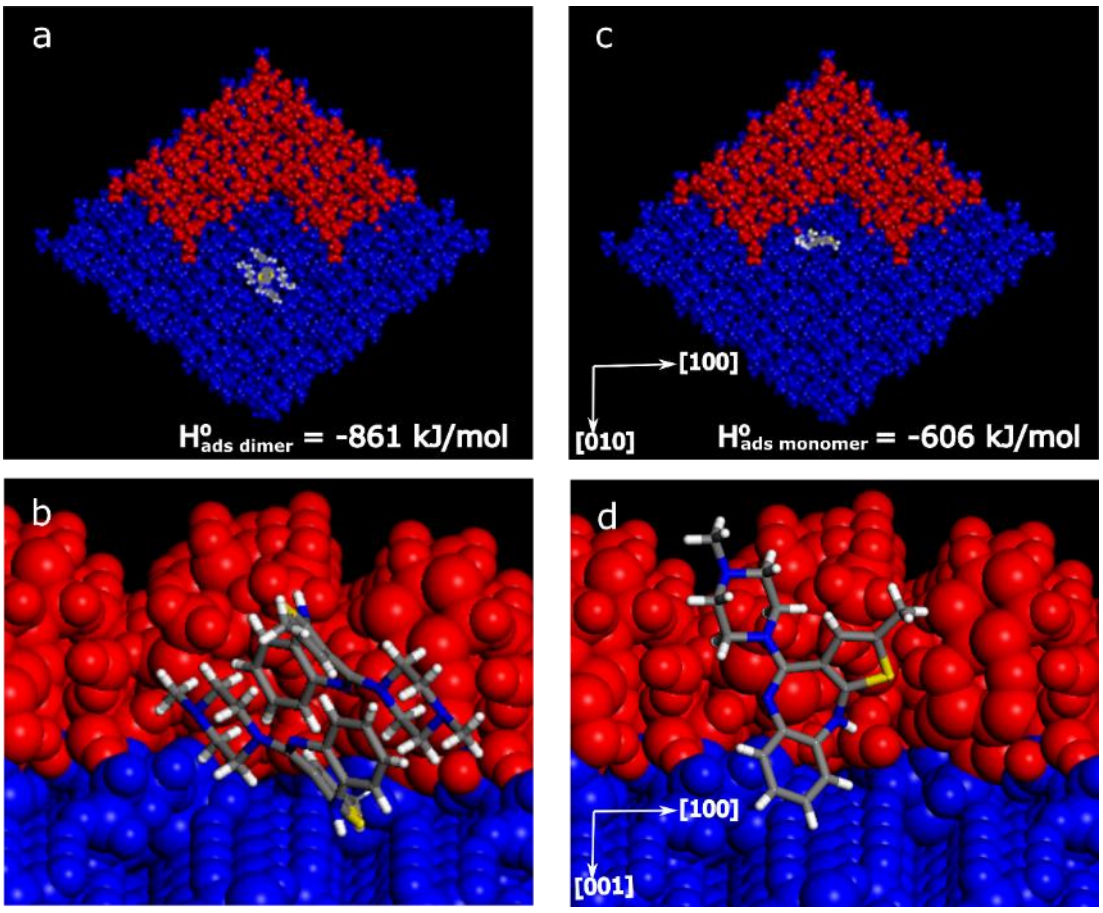

Figure 67 Calculations of ΔH^o_{ads} for SC_0 dimer and OZPN monomer. a) top view, b) side view of dimer adsorbed on $(002)_{OZPNHE}$ terrace and c) top view d) side view of OZPN monomer adsorbed on the surface of $(002)_{OZPNHE}$.

6.4 Conclusions

This chapter has been focused on the growth mechanism for OZPN HE crystals. Several scenarios were considered: classical growth by monomer-to-monomer addition and non-classical growth by SC_0 dimers and growth by incorporation of prenucleation clusters.

Although, mesoscopic clusters detected in OZPN solutions are significant for the OZPN anhydrate to hydrate transition, it was observed that they do not take part in a growth mechanism and new OZPN HE layers. Instead, $(002)_{OZPNHE}$ grows by spiral growth mechanism by addition of preformed OZPN dimers. This non-classical mechanism has been experimentally demonstrated for the first time using an in-situ AFM technique. In solution, self-association of OZPN molecules to dimers was detected using NMR and Raman spectroscopy. These dimers are the minor species in OZPN solution and that determines a super linear dependence of step velocity, ν, on the OZPN concentration. Several kinetic factors for growth by monomers and dimers have been considered and it was concluded that growth by dimers is faster not owing to spatial or entropic factors or to weakly bound solvent. The surface diffusion mechanism was discussed and adsorption enthalpies ΔH^o_{ads} for OZPN monomer and OZPN dimer reveal that OZPN dimer has lower adsorption energy and the crystal surface of $(002)_{OZPNHE}$ serves as a collector of dimers. Since the population of dimers on the surface is much higher, the growth by dimers is kinetically favoured over growth by incorporation of monomers. Formation of OZPN dimers in solution strongly depends on the nature of the solvent and was easily detected in chloroform while in ethanol/water mixtures dimers were present in a minority and could be detected in highly supersaturated solutions. Self-assembly of dimers has not been tested in other

solvents, although previous studies show solid-form screening for OZPN did not result in diverse crystal packing. All crystal structure obtained from 56 solvents and vapour phase contain SC_0 dimers. Together with the conclusions from this chapter. This suggests that the dimer could be a building block for all OZPN neat and solvated solid-forms, even though it is not a major component of OZPN solutions. This could explain why predicted crystal structures with other OZPN motifs have not been crystallised to date and to obtain these structure more unconventional crystallisation methods have to be applied.

7 Overall conclusions

7.1 Nucleation

The overall aim of this thesis was to provide a better understanding of the processes occurring during crystal nucleation, solid-state transitions and growth in aqueous solutions of olanzapine. Olanzapine, in common with many more protein, organic and inorganic systems aggregate in an aqueous solution into prenucleation, solute-rich clusters. The nucleation mechanism for these systems has been described as non-classical or two-step nucleation mechanism that assumes that clusters are the intermediate form between a solution and fully developed crystal. The clusters were detected in undersaturated and supersaturated OZPN solutions, although due to their small size (30-70 nm in radius) and low volume fraction ($10^{-8} – 10^{-7)}$ it was difficult to characterize their internal structure. Both OIM and AFM techniques were able to provide the information about the size and volume fraction of these nanoscale species. In common with, to clusters found in many protein systems, OZPN cluster radius R was independent of the OZPN concentration and the solvent composition or time. On the other hand, the volume of the cluster population ϕ was dependent on the thermodynamic parameters of the solution. These discrepancies suggest that the OZPN-rich cluster behaviour is consistent with the predictions of the model for protein prenucleation clusters that assumes the formation of dimers and water structuring around the molecules are the key factors for the formation of clusters. The detailed study of the OZPN clusters allowed us to compare the mechanism of their formation to a well-established two-step nucleation model for a protein crystallisation and for the first time it was proven that the same mechanism operates for a formation of clusters containing small organic molecules, in this case - OZPN, and clusters containing much complex and bigger molecules such as proteins.

A deeper understanding of the nucleation mechanism for small organic molecules opens up new opportunities in designing specific strategies such as tailor-made additives to manipulate nucleation process characteristics such as induction time, nucleation rate or polymorphic form.

7.2 Solid-state transformations

Solid-form transformations, especially these leading to the hydrate formation, are the most widespread and undesirable in the pharmaceutical industry. In the case of OZPN, the impact of dissolution properties on drug product performance is critical. Conversion to a more stable, less soluble hydrated form could compromise dissolution. Transformations limited to the surface of the crystal are difficult to detect by conventional techniques, (e.g., PXRD) therefore employing surface related techniques such as AFM provided lots of valuable information about hydration processes. In the case of OZPN, the presence of prenucleation clusters was a critical step during OZPN I to OZPN dihydrate transformation. The clusters aggregated to bigger droplets and their further crystallisation pathway was dictated by the internal reorganisation in the presence or absence of OZPN I surface. In quiescent conditions, only the presence of the thermodynamic form OZPN DD was observed. This crystal form was produced by the templating effect of the $(100)_{OZPNI}$ surface which shows a structural similarity and energetic preference for OZPN DD over the metastable OZPN DB. Under stirred conditions, nanodroplets were detached from the surface, resulting in the nucleation and formation of OZPN DB without any templating effect from $(100)_{OZPNI}$ surface. Strong effect of templating in OZPN I to OZPN hydrate transformation shows that the polymorph transformation pathways can be controlled by specific interactions between the underlying surface and the OZPN clusters. Additionally, this type of transformation

could be delayed or suppressed by controlling the volume fraction of the clusters e.g. by modifying the thermodynamic parameters of the solution and suppressing the formation of dimers or other oligomers using tailor made additives.

7.3 Crystal growth

The work reported in this thesis was also focused on a growth mechanism for olanzapine crystals. Although, mesoscopic clusters have been proven to take part in growth mechanism for different system such as proteins and amino acids, clusters detected in OZPN solutions were not observed to incorporate into OZPN crystal layers. In turn, they did not take part in the growth mechanism. Instead, $(002)_{OZPNHE}$ grows by spiral growth mechanism by addition of preformed OZPN dimers.
In solution, self-association of OZPN molecules to dimers was detected using NMR and Raman spectroscopy. These preformed dimers are the minor species in OZPN solution and this determines the non-linear dependence of step velocity, v, on the OZPN concentration. Several kinetic factors for growth by monomers and dimers have been considered and it was concluded that growth by dimers is faster not due to spatial or entropic factors or weakly bound solvent, but to the accumulation of dimers on crystal surfaces due to stronger binding. Since the population of dimers on the surface is much higher on the crystal surface, the growth by dimers is kinetically favoured over growth by incorporation of monomers. Stronger binding of OZPN dimers to the crystal surface may also explain why computed, thermodynamically stable solid-forms of OZPN with different structural motifs have not been crystallised to date.

The crystallisation of API is challenging due to the low symmetry and high flexibility of organic molecules. An organic molecule may crystallise in numerous distinct

lattices and the slow and unpredictable transitions between multiple crystal forms is a significant concern in its pharmaceutical application. This study provides considerable insights into how pharmaceutical molecules, with their far from spherical shapes and highly anisotropic intermolecular interactions, do not confirm to the models of crystal nucleation and growth for spherical isotropic growth units. Therefore, further understanding of the nucleation and the growth mechanism will lead to a better design of crystallisation processes and a greater degree of control over crystal properties such as polymorphism, morphology, purity or size distribution which are key properties of pharmaceutical products.

8 Future Research

8.1 Unconventional crystallisation of OZPN

The majority of the structures on the predicted crystal energy landscape for OZPN do not contain the centrosymmetric SC_0 dimer that is observed in all of the known polymorphs and solvates obtained experimentally using techniques such as cooling crystallisation, evaporation, grinding, freeze-drying, etc. The CSP provide evidence that the alternative packing arrangements are nonetheless thermodynamically competitive. Application of less typical crystallisation conditions such as crystallisation on polymeric surfaces or self-assembled monolayers (SAMs) could potentially disturb the packing arrangement of OZPN molecules. Polymeric substrates with imprinted nanoscale features design to match the angles between major crystallographic faces have been used to crystallise aspirin and indomethacin.[12] A substrate was made of biocompatible poly(vinyl alcohol) (PVA) and was proven to reduce the nucleation induction time due to favourable interactions between the polymer and nucleus. This has been further enhanced by the fact that the angles between the nanofeatures closely match the angles between the major crystallographic faces of the model compounds. In common with polymer surfaces, SAMs surfaces have been successfully applied in polymorph screening[22,140,141,218] with multiple polymorphs of ROY, isonicotinamide, or 2,6- dihydroxybenzoic acid nucleated on patterned metallic gold islands. Specific intermolecular interactions between modelled compounds and SAMs were identified using Raman spectroscopy and were responsible for the formation of a specific polymorph.[218] Computer simulations such as adsorption energy measurements using Materials Studio package could be used to guide the selection of the surfaces.

8.2 Non-classical nucleation and transformation for small pharmaceutical molecules

Investigation of hydrate formation is crucial for the pharmaceutical industry. Therefore, further study extended to other pharmaceutical molecules would improve our current understanding of hydrate formation. If the hydrate nucleation is directed by the water structuring and molecular association between the solute molecules, various additives could be designed to inhibit the transformation kinetics. Compounds structurally related to OZPN such as Clozapine and Amoxapine could be used as model compounds to further investigate anhydrate to hydrate transitions and to investigate if two-step nucleation process are unique for the OZPN system or is a common process occurring for other pharmaceutical compounds during hydrate nucleation. Wikström *et. al.*[219] studied several drugs hydration mechanism looking at their specific properties such as solubility, dissolution rate, and growth rate of hydrate phase, and the influence of external factors such as seeding and agitation conditions. The finding present that the overall transformation rate from anhydrous to hydrate form was not a simple relationship between the transformation kinetics and solubility or intrinsic dissolution rate, but rather a function of compound-specific properties. Therefore, further investigation of this process would be beneficial for crystallisation processes.

9 References

(1) Saleemi, A. N.; Rielly, C. D.; Nagy, Z. K. Comparative Investigation of Supersaturation and Automated Direct Nucleation Control of Crystal Size Distributions Using ATR-UV/Vis Spectroscopy and FBRM. *Cryst. Growth Des.* **2012**, *12* (4), 1792–1807.

(2) Simone, E.; Zhang, W.; Nagy, Z. K. Application of Process Analytical Technology-Based Feedback Control Strategies To Improve Purity and Size Distribution in Biopharmaceutical Crystallization. *Cryst. Growth Des.* **2015**, *15* (6), 2908–2919.

(3) Quon, J. L.; Chadwick, K.; Wood, G. P. F.; Sheu, I.; Brettmann, B. K.; Myerson, A. S.; Trout, B. L. Templated Nucleation of Acetaminophen on Spherical Excipient Agglomerates. *Langmuir* **2013**, *29* (10), 3292–3300.

(4) Sudha, C.; Srinivasan, K. Supersaturation Dependent Nucleation Control and Separation of Mono, Ortho and Unstable Polymorphs of Paracetamol by Swift Cooling Crystallization Technique. *CrystEngComm* **2013**, *15* (10), 1914–1921.

(5) Bučar, D. K.; Lancaster, R. W.; Bernstein, J. Disappearing Polymorphs Revisited. *Angew. Chemie - Int. Ed.* **2015**, *54* (24), 6972–6993.

(6) Rampton, C. H. S. F. Physicochemical Characterization of the Orthorhombic Polymorph of Paracetamol Crystallized from Solution. *J. Pharm. Sci.* **1998**, *87* (6), 684–693.

(7) Bhardwaj, R. M.; Price, L. S.; Price, S. L.; Reutzel-Edens, S. M.; Miller, G. J.; Oswald, I. D. H.; Johnston, B. F.; Florence, A. J. Exploring the Experimental and Computed Crystal Energy Landscape of Olanzapine. *Cryst. Growth Des.* **2013**, *13* (4), 1602–1617.

(8) Arlin, J.-B.; Price, L. S.; Price, S. L.; Florence, A. J. A Strategy for Producing Predicted Polymorphs: Catemeric Carbamazepine Form V. *Chem. Commun.* **2011**, *47* (25), 7074–7076.

(9) Braun, D. E.; McMahon, J. A.; Koztecki, L. H.; Price, S. L.; Reutzel-Edens, S. M. Contrasting Polymorphism of Related Small Molecule Drugs Correlated and Guided by the Computed Crystal Energy Landscape. *Cryst. Growth Des.* **2014**, *14* (4), 2056–2072.

(10) Price, S. L. Predicting Crystal Structures of Organic Compounds. *Chem. Soc. Rev.* **2014**, *43* (7), 2098–2111.

(11) Bonafede, S.; Ward, M. D. Selective Nucleation and Growth of an Organic Polymorph by Ledge-Directed Epitaxy on a Molecular Crystal Substrate. *J. Am. Chem. Sociaty* **1995**, *117* (1), 7853–7861.

(12) Tan, L.; Davis, R. M.; Myerson, A. S.; Trout, B. L. Control of Heterogeneous Nucleation via Rationally Designed Biocompatible Polymer Surfaces with Nanoscale Features. *Cryst. Growth Des.* **2015**, *15*, 2176–2186.

(13) Lee, E. H.; Boerrigter, S. X. M.; Byrn, S. R. Epitaxy of a Structurally Related Compound on the (100) Faces of Flufenamic Acid Form i and Iii Single Crystals. *Cryst. Growth Des.* **2010**, *10* (2), 518–527.

(14) Mitchell, C. a.; Yu, L.; Ward, M. D. Selective Nucleation and Discovery of Organic Polymorphs through Epitaxy with Single Crystal Substrates. *J. Am. Chem. Soc.* **2001**, *123* (44), 10830–10839.

(15) Srirambhatla, V. K.; Guo, R.; Price, S. L.; Florence, A. J. Isomorphous Template Induced Crystallisation: A Robust Method for the Targeted Crystallisation of Computationally Predicted Metastable Polymorphs. *Chem. Commun.* **2016**, *52* (46), 7384–7386.

(16) Campione, M.; Sassella, A.; Moret, M.; Papagni, A.; Trabattoni, S.; Resel, R.; Lengyel, O.; Marcon, V.; Raos, G. Organic-Organic Epitaxy of Incommensurate Systems: Quaterthiophene on Potassium Hydrogen Phthalate Single Crystals. *J. Am. Chem. Soc.* **2006**, *128* (41), 13378–13387.

(17) Lang, M.; Grzesiak, A. L.; Matzger, A. J. The Use of Polymer Heteronuclei for Crystalline Polymorph Selection. *J. Am. Chem. Soc.* **2002**, *124* (50), 14834–14835.

(18) Grzesiak, A. L.; Uribe, F. J.; Ockwig, N. W.; Yaghi, O. M.; Matzger, A. J. Polymer-Induced Heteronucleation for the Discovery of New Extended Solids. *Angew. Chemie - Int. Ed.* **2006**, *45* (16), 2553–2556.

(19) Chadwick, K.; Chen, J.; Myerson, A. S.; Trout, B. L. Toward the Rational Design of Crystalline Surfaces for Heteroepitaxy: Role of Molecular Functionality. *Cryst. Growth Des.* **2012**, *12* (3), 1159–1166.

(20) Price, C. P.; Grzesiak, A. L.; Matzger, A. J. Crystalline Polymorph Selection and Discovery with Polymer Heteronuclei. *J. Am. Chem. Soc.* **2005**, *127* (15),

5512–5517.

(21) Sudha, C.; Nandhini, R.; Srinivasan, K. Polymer-Induced Selective Nucleation of Mono or Ortho Polymorphs of Paracetamol through Swift Cooling of Boiled Aqueous Solution. *Cryst. Growth Des.* **2014**, *14* (2), 705–715.

(22) Singh, A.; Lee, I. S.; Kim, K.; Myerson, A. S. Crystal Growth on Self-Assembled Monolayers. *CrystEngComm* **2011**, *13* (1), 24.

(23) Pfund, L. Y.; Matzger, A. J. Towards Exhaustive and Automated High-Throughput Screening for Crystalline Polymorphs. *ACS Comb. Sci.* **2014**, *16*, 309−313.

(24) Gibbs, J. W. No Title. *Trans. Connect. Acad. Arts Sci.* **1876**, *3*, 108–248.

(25) Volmer, M.; Weber, A. Nuclei Formation in Supersaturated States. *Zeitschrift für Phys. Chemie* **1925**, *119*, 277–301.

(26) Becker, R.; Döring, W. Kinetische Behandlung Der Keimbildung in Übersättigten Dämpfen. *Ann. Phys.* **1935**, *24*, 719–752.

(27) Frankel, J. No Title. *J. Chem. Phys.* **1939**, *7*, 538–547.

(28) Kashchiev, D. *Nucleation: Basic Theory with Applications*; Butterworth-Heinemann, Oxford, 2000.

(29) Vekilov, P. G. Dense Liquid Precursor for the Nucleation of Ordered Solid Phase from Solution. *Cryst. Growth Des.* **2004**, *4* (4), 671–685.

(30) Vekilov, P. G. The Two-Step Mechanism of Nucleation of Crystals in Solution.

Nanoscale **2010**, *2* (11), 2346–2357.

(31) Gliko, O.; Neumaier, N.; Pan, W.; Haase, I.; Fischer, M.; Bacher, A.; Weinkauf, S.; Vekilov, P. G. A Metastable Prerequisite for the Growth of Lumazine Synthase Crystals. *J. Am. Chem. Soc.* **2005**, *127* (10), 3433–3438.

(32) Galkin, O.; Vekilov, P. G. Control of Protein Crystal Nucleation around the Metastable Liquid-Liquid Phase Boundary. *Proc. Natl. Acad. Sci. U. S. A.* **2000**, *97* (12), 6277–6281.

(33) Vekilov, P. G. Nucleation. *Cryst. Growth Des.* **2010**, *10* (12), 5007–5019.

(34) Malkin, A. J.; Kuznetsov, Y. G.; Land, T. A.; DeYoreo, J. J.; McPherson, A. Mechanisms of Growth for Protein and Virus Crystals. *Nat Struct Mol Biol* **1995**, *2* (11), 956–959.

(35) Li, Y.; Lubchenko, V.; Vorontsova, M. A.; Filobelo, L.; Vekilov, P. G. Ostwald-like Ripening of the Anomalous Mesoscopic Clusters in Protein Solutions. *J. Phys. Chem. B* **2012**, *116* (35), 10657–10664.

(36) Li, Y.; Lubchenko, V.; Vekilov, P. G. The Use of Dynamic Light Scattering and Brownian Microscopy to Characterize Protein Aggregation. *Rev. Sci. Instrum.* **2011**, *82* (5), 053106.

(37) Gebauer, D.; Cölfen, H. Prenucleation Clusters and Non-Classical Nucleation. *Nano Today* **2011**, *6* (6), 564–584.

(38) Gebauer, D.; Kellermeier, M.; Gale, J. D.; Bergström, L.; Cölfen, H. Pre-Nucleation Clusters as Solute Precursors in Crystallisation. *Chem. Soc. Rev.*

2014, *43* (7), 2348–2371.

(39) Nielsen, M. H.; Aloni, S.; Yoreo, J. J. De. In Situ TEM Imaging of CaCO 3 Nucleation Reveals Coexistence of Direct and Indirect Pathways. *Science (80-.).* **2013**, *218* (2004), 213–218.

(40) Sebastiani, F.; Wolf, S. L. P.; Born, B.; Luong, T. Q.; Cölfen, H.; Gebauer, D.; Havenith, M. Water Dynamics from THz Spectroscopy Reveal the Locus of a Liquid-Liquid Binodal Limit in Aqueous CaCO3 Solutions. *Angew. Chemie Int. Ed.* **2017**, *56* (2), 490–495.

(41) Chattopadhyay, S.; Erdemir, D.; Evans, J. M. B.; Ilavsky, J.; Amenitsch, H.; Segre, C. U.; Myerson, A. S. SAXS Study of the Nucleation of Glycine Crystals from a Supersaturated Solution. *Cryst. Growth Des.* **2005**, *5* (2), 523–527.

(42) Aber, J. E.; Arnold, S.; Garetz, B. A.; Myerson, A. S. Strong Dc Electric Field Applied to Supersaturated Aqueous Glycine Solution Induces Nucleation of the γ Polymorph. *Phys. Rev. Lett.* **2005**, *94* (14), 1–4.

(43) Jawor-Baczynska, A.; Moore, B. D.; Lee, H. S.; McCormick, A. V.; Sefcik, J. Population and Size Distribution of Solute-Rich Mesospecies within Mesostructured Aqueous Amino Acid Solutions. *Faraday Discuss.* **2013**, *167* (0), 425–440.

(44) Jawor-Baczynska, A.; Moore, B. D.; Sefcik, J. Effect of Mixing, Concentration and Temperature on the Formation of Mesostructured Solutions and Their Role in the Nucleation of Dl-Valine Crystals. *Faraday Discuss.* **2015**, *179* (0), 141–154.

(45) Jawor-Baczynska, A.; Sefcik, J.; Moore, B. D. 250 Nm Glycine-Rich Nanodroplets Are Formed on Dissolution of Glycine Crystals But Are Too Small To Provide Productive Nucleation Sites. *Cryst. Growth Des.* **2013**, *13* (2), 470–478.

(46) Peng, Y.; Wang, F.; Wang, Z.; Alsayed, A. M.; Zhang, Z.; Yodh, A. G.; Han, Y. Two-Step Nucleation Mechanism in Solid–solid Phase Transitions. *Nat Mater* **2015**, *14* (1), 101–108.

(47) Bera, M. K.; Antonio, M. R. Crystallization of Keggin Heteropolyanions via a Two-Step Process in Aqueous Solutions. *J. Am. Chem. Soc.* **2016**, *138* (23), 7282–7288.

(48) Ito, F.; Suzuki, Y.; Fujimori, J.; Sagawa, T.; Hara, M.; Seki, T.; Yasukuni, R.; Lamy de la Chapelle, M. Direct Visualization of the Two-Step Nucleation Model by Fluorescence Color Changes during Evaporative Crystallization from Solution. *Sci. Rep.* **2016**, *6*, 1–6.

(49) DeYoreo, J. J.; Gilbert, P. U. P. A.; Sommerdijk, N. A. J. M.; Penn, R. L.; Whitelam, S.; Joester, D.; Zhang, H.; Rimer, J. D.; Navrotsky, A.; Banfield, J. F.; et al. Crystallization by Particle Attachment in Synthetic, Biogenic, and Geologic Environments. *Science (80-.).* **2015**, *349* (6247), 498.

(50) Jiang, Y.; Kellermeier, M.; Gebaue, D.; Lu, Z.; Rosenberg, R.; Moise, A.; Przybylski, M.; Cölfen, H. Growth of Organic Crystals via Attachment and Transformation of Nanoscopic Precursors. *Nat. Commun.* **2017**, 1–6.

(51) Sleutel, M.; Van Driessche, A. E. S. Role of Clusters in Nonclassical Nucleation

and Growth of Protein Crystals. *Proc. Natl. Acad. Sci. U. S. A.* **2014**, *111* (5), E546-53.

(52) Xie, B.; Halter, T. J.; Borah, B. M.; Nancollas, G. H. Tracking Amorphous Precursor Formation and Transformation during Induction Stages of Nucleation. *Cryst. Growth Des.* **2014**, *14* (4), 1659–1665.

(53) Zhu, Q.; Toth, S. J.; Simpson, G. J.; Hsu, H.; Taylor, L. S.; Harris, M. T. Crystallization and Dissolution Behavior of Naproxen / Polyethylene Glycol Solid Dispersions. *J. Phys. Chem. C* **2013**, *117*, 1494–1500.

(54) Ehmann, H. M. A.; Werzer, O. Surface Mediated Structures: Stabilization of Metastable Polymorphs on the Example of Paracetamol. *Cryst. Growth Des.* **2014**, *14* (8), 3680–3684.

(55) Musumeci, D.; Ward, M. D. Elucidation of the Crystal Growth Mechanism of Melamine-Cyanuric Acid by Using Real Time in Situ Atomic Force Microscopy. *CrystEngComm* **2011**, *13* (4), 1067.

(56) Thakuria, R.; Eddleston, M. D.; Chow, E. H. H.; Lloyd, G. O.; Aldous, B. J.; Krzyzaniak, J. F.; Bond, A. D.; Jones, W. Use of in Situ Atomic Force Microscopy to Follow Phase Changes at Crystal Surfaces in Real Time. *Angew. Chem. Int. Ed. Engl.* **2013**, *52* (40), 10541–10544.

(57) Cai, T.; Zhu, L.; Yu, L. Crystallization of Organic Glasses: Effects of Polymer Additives on Bulk and Surface Crystal Growth in Amorphous Nifedipine. *Pharm. Res.* **2011**, *28* (10), 2458–2466.

(58) Govedarica, B.; Sovány, T.; Pintye-Hódi, K.; Skarabot, M.; Baumgartner, S.; Muševič, I.; Srčič, S. Addressing Potent Single Molecule AFM Study in Prediction of Swelling and Dissolution Rate in Polymer Matrix Tablets. *Eur. J. Pharm. Biopharm.* **2012**, *80* (1), 217–225.

(59) Miyazaki, T.; Aso, Y.; Kawanishi, T. Feasibility of Atomic Force Microscopy for Determining Crystal Growth Rates of Nifedipine at the Surface of Amorphous Solids with and Without Polymers. *J. Pharm. Sci.* **2011**, *100* (10), 4413–4420.

(60) Rimer, J. D.; An, Z.; Zhu, Z.; Lee, M. H.; Goldfarb, D. S.; Wesson, J. a; Ward, M. D. Crystal Growth Inhibitors for the Prevention of L-Cystine Kidney Stones through Molecular Design. *Science (80-.).* **2010**, *330*, 337–341.

(61) Tilbury, C. J.; Green, D. A.; Marshall, W. J.; Doherty, M. F. Predicting the Effect of Solvent on the Crystal Habit of Small Organic Molecules. *Cryst. Growth Des.* **2016**, *16* (5), 2590–2604.

(62) Sun, Y.; Tilbury, C. J.; Reutzel-Edens, S. M.; Bhardwaj, R. M.; Li, J.; Doherty, M. F. Modeling Olanzapine Solution Growth Morphologies. *Cryst. Growth Des.* **2018**, acs.cgd.7b01389.

(63) Kuvadia, Z. B.; Doherty, M. F. Spiral Growth Model for Faceted Crystals of Non-Centrosymmetric Organic Molecules Grown from Solution. *Cryst. Growth Des.* **2011**, *11* (7), 2780–2802.

(64) Li, J.; Tilbury, C. J.; Kim, S. H.; Doherty, M. F. A Design Aid for Crystal Growth Engineering. *Prog. Mater. Sci.* **2016**, *82*, 1–38.

(65) Spitaleri, A.; Hunter, C. A.; McCabe, J. F.; Packer, M. J.; Cockroft, S. L. A 1H NMR Study of Crystal Nucleation in Solution. *CrystEngComm* **2004**, *6* (80), 489.

(66) Hunter, C. A.; Packer, M. J. Complexation-Induced Changes in 1H NMR Chemical Shift for Supramolecular Structure Determination. *Chem. – A Eur. J.* **1999**, *5* (6), 1891–1897.

(67) Hunter, C. A.; McCabe, J. F.; Spitaleri, A. Solvent Effects of the Structures of Prenucleation Aggregates of Carbamazepine. *CrystEngComm* **2012**, *14* (21), 7115.

(68) Back, K. R.; Davey, R. J.; Grecu, T.; Hunter, C. A.; Taylor, L. S. Molecular Conformation and Crystallization: The Case of Ethenzamide. *Cryst. Growth Des.* **2012**, *12* (12), 6110–6117.

(69) Davey, R. J.; Dent, G.; Mughal, R. K.; Parveen, S. Concerning the Relationship between Structural and Growth Synthons in Crystal Nucleation: Solution and Crystal Chemistry of Carboxylic Acids as Revealed through IR Spectroscopy. *Cryst. Growth Des.* **2006**, *6* (8), 1788–1796.

(70) Sullivan, R. A.; Davey, R. J.; Sadiq, G.; Dent, G.; Back, K. R.; Ter Horst, J. H.; Toroz, D.; Hammond, R. B. Revealing the Roles of Desolvation and Molecular Self-Assembly in Crystal Nucleation from Solution: Benzoic and p -Aminobenzoic Acids. *Cryst. Growth Des.* **2014**, *14* (5).

(71) Sultana, M.; Jensen, K. F. Micro Fluidic Continuous Seeded Crystallization: Extraction of Growth Kinetics and Impact of Impurity on Morphology. *Cryst.*

Growth Des. **2012**, *12*, 6260–6266.

(72) Wong, S. Y.; Cui, Y.; Myerson, A. S. Contact Secondary Nucleation as a Means of Creating Seeds for Continuous Tubular Crystallizers. *Cryst. Growth Des.* **2013**, *13* (6), 2514–2521.

(73) Rashid, A.; White, E. T.; Howes, T.; Litster, J. D.; Marziano, I. Growth Rates of Ibuprofen Crystals Grown from Ethanol and Aqueous Ethanol. *Chem. Eng. Res. Des.* **2012**, *90* (1), 158–161.

(74) Jiang, Q.; Ward, M. D. Crystallization under Nanoscale Confinement. *Chem. Soc. Rev.* **2014**, *43* (7), 2066–2079.

(75) Davey, R. J.; Schroeder, S. L. M.; ter Horst, J. H. Nucleation of Organic Crystals-A Molecular Perspective. *Angew. Chemie - Int. Ed.* **2013**, *52* (8), 2166–2179.

(76) Vekilov, P. G. Two-Step Mechanism for the Nucleation of Crystals from Solution. *J. Cryst. Growth* **2005**, *275* (1–2), 65–76.

(77) Pan, W.; Vekilov, P. G.; Lubchenko, V. Origin of Anomalous Mesoscopic Phases in Protein Solutions. *J. Phys. Chem. B* **2010**, *114* (22), 7620–7630.

(78) Gliko, O.; Pan, W.; Katsonis, P.; Neumaier, N.; Galkin, O.; Weinkauf, S.; Vekilov, P. G. Metastable Liquid Clusters in Super- and Undersaturated Protein Solutions. *J. Phys. Chem. B* **2007**, *111* (12), 3106–3114.

(79) Uzunova, V.; Pan, W.; Lubchenko, V.; Vekilov, P. G. Control of the Nucleation of Sickle Cell Hemoglobin Polymers by Free Hematin. *Faraday Discuss.* **2012**,

159, 87.

(80) Yamazaki, T.; Kimura, Y.; Vekilov, P. G.; Furukawa, E.; Shirai, M.; Matsumoto, H.; Van Driessche, A. E. S.; Tsukamoto, K. Two Types of Amorphous Protein Particles Facilitate Crystal Nucleation. *Proc. Natl. Acad. Sci.* **2017**, *114* (9), 2154–2159.

(81) Wang, L.; Li, S.; Ruiz-Agudo, E.; Putnis, C. V.; Putnis, A. Posner's Cluster Revisited: Direct Imaging of Nucleation and Growth of Nanoscale Calcium Phosphate Clusters at the Calcite-Water Interface. *CrystEngComm* **2012**, *14*, 6252.

(82) Salvalaglio, M.; Mazzotti, M.; Parrinello, M. Urea Homogeneous Nucleation Mechanism Is Solvent Dependent. *Faraday Discuss.* **2015**.

(83) Harano, K.; Homma, T.; Niimi, Y.; Koshino, M.; Suenaga, K.; Leibler, L.; Nakamura, E. Heterogeneous Nucleation of Organic Crystals Mediated by Single-Molecule Templates. *Nat. Mater.* **2012**, *11* (10), 877–881.

(84) Rodríguez-Hornedo, N.; Murphy, D. Significance of Controlling Crystallization Mechanisms and Kinetics in Pharmaceutical Systems. *J. Pharm. Sci.* **1999**, *88* (7), 651–660.

(85) Burton, W. K.; Cabrera, N.; Frank, F. C. The Growth of Crystals and the Equilibrium Structure of Their Surfaces. *Philos. Trans. R. Soc. A Math. Phys. Eng. Sci.* **1951**, *243* (866), 299–358.

(86) Gratz, A. J.; Hillner, P. E.; Hansma, P. K. Step Dynamics and Spiral Growth on

Calcite. *Geochim. Cosmochim. Acta* **1993**, *57* (2), 491–495.

(87) Olafson, K. N.; Ketchum, M. A.; Rimer, J. D.; Vekilov, P. G. Molecular Mechanisms of Hematin Crystallization from Organic Solvent. *Cryst. Growth Des.* **2015**, *15* (11), 5535–5542.

(88) Vekilov, P. G. G.; Kuznetsov, Y. G.; Chernov, A. A. A. Interstep Interaction in Solution Growth; (101) ADP Face. *J. Cryst. Growth* **1992**, *121* (4), 643–655.

(89) Vekilov, P. G.; Kuznetsov, Y. G.; Chernov, A. A. The Effect of Temperature on Step Motion; (101) ADP Face. *J. Cryst. Growth* **1992**, *121* (1), 44–52.

(90) Chen, K.; Vekilov, P. G. Evidence for the Surface-Diffusion Mechanism of Solution Crystallization from Molecular-Level Observations with Ferritin. *Phys. Rev. E - Stat. Physics, Plasmas, Fluids, Relat. Interdiscip. Top.* **2002**, *66* (2), 1–5.

(91) Lovette, M. a.; Browning, A. R.; Griffin, D. W.; Sizemore, J. P.; Snyder, R. C.; Doherty, M. F. Crystal Shape Engineering. *Ind. Eng. Chem. Res.* **2008**, *47* (24), 9812–9833.

(92) Tung, H.-H. Industrial Perspectives of Pharmaceutical Crystallization. *Org. Process Res. Dev.* **2013**, *17* (3), 445–454.

(93) MacLeod, C. S.; Muller, F. L. On the Fracture of Pharmaceutical Needle-Shaped Crystals during Pressure Filtration: Case Studies and Mechanistic Understanding. *Org. Process Res. Dev.* **2012**, *16* (3), 425–434.

(94) Klapwijk, A. R.; Simone, E.; Nagy, Z. K.; Wilson, C. C. Tuning Crystal

Morphology of Succinic Acid Using a Polymer Additive. *Cryst. Growth Des.* **2016**, *16* (8), 4349–4359.

(95) Price, S.; Rimez, B.; Sun, W.; Peters, B.; Christenson, H.; Hughes, C.; Sun, C. C.; Veesler, S.; Pan, H.; Brandel, C.; et al. Nucleation in Complex Multi-Component and Multi-Phase Systems: General Discussion. *Faraday Discuss.* **2015**, *179* (Nucleation--A Transition State to the Directed Assembly of Materials), 503–542.

(96) Gong, Y. U. T.; Killian, C. E.; Olson, I. C.; Appathurai, N. P.; Amasino, A. L.; Martin, M. C.; Holt, L. J.; Wilt, F. H.; Gilbert, P. U. P. A. Phase Transitions in Biogenic Amorphous Calcium Carbonate. *Proc. Natl. Acad. Sci.* **2012**, *109* (16), 6088 LP-6093.

(97) Beniash, E.; Aizenberg, J.; Addadi, L.; Weiner, S. Amorphous Calcium Carbonate Transforms into Calcite during Sea Urchin Larval Spicule Growth. *Proc. R. Soc. London. Ser. B Biol. Sci.* **1997**, *264* (1380), 461 LP-465.

(98) Li, D.; Nielsen, M. H.; Lee, J. R. I.; Frandsen, C.; Banfield, J. F.; De Yoreo, J. J. Direction-Specific Interactions Control Crystal Growth by Oriented Attachment. *Science (80-.).* **2012**, *336* (6084), 1014 LP-1018.

(99) Zhang, J.; Huang, F.; Lin, Z. Progress of Nanocrystalline Growth Kinetics Based on Oriented Attachment. *Nanoscale* **2010**, *2* (1), 18–34.

(100) Parveen, S.; Davey, R. J.; Dent, G.; Pritchard, R. G. Linking Solution Chemistry to Crystal Nucleation: The Case of Tetrolic Acid. *Chem. Commun.* **2005**, No. 12, 1531–1533.

(101) Kulkarni, S. A.; McGarrity, E. S.; Meekes, H.; ter Horst, J. H. Isonicotinamide Self-Association: The Link between Solvent and Polymorph Nucleation. *Chem. Commun.* **2012**, *48* (41), 4983.

(102) Hulme, A. T.; Johnston, A.; Florence, A. J.; Fernandes, P.; Shankland, K.; Bedford, C. T.; Welch, G. W. A.; Sadiq, G.; Haynes, D. A.; Motherwell, W. D. S.; et al. Search for a Predicted Hydrogen Bonding Motif - A Multidisciplinary Investigation into the Polymorphism of 3-Azabicyclo[3.3.1]Nonane-2,4-Dione. *J. Am. Chem. Soc.* **2007**, *129* (12), 3649–3657.

(103) Chen, J.; Trout, B. L. Computational Study of Solvent Effects on the Molecular Self-Assembly of Tetrolic Acid in Solution and Implications for the Polymorph Formed from Crystallization. *J. Phys. Chem. B* **2008**, *112* (26), 7794–7802.

(104) Magnetic, P. Interaction and Association of Bases and Nucleosides in Aqueous Solutions . V . Studies of the Association of Purine Nucleosides by Vapor Pressure Osmometry and by Proton Magnetic Resonancela , B. **1967**, *523* (6), 3612–3622.

(105) Gardner, M.; J. Guerin, A.; A. Hunter, C.; Michelsen, U.; Rotger, C. Self-Assembly of Zinc Aminoporphyrins. *New J. Chem.* **1999**, *23* (3), 309.

(106) Vorontsova, M. a.; Maes, D.; Vekilov, P. G. Recent Advances in the Understanding of Two-Step Nucleation of Protein Crystals. *Faraday Discuss.* **2015**, *179*, 27–40.

(107) Li, Y.; Lubchenko, V.; Vekilov, P. G.; Li, Y.; Lubchenko, V.; Vekilov, P. G. The Use of Dynamic Light Scattering and Brownian Microscopy to

Characterize Protein Aggregation. *Rev. Sci. Instrum.* **2015**, *82* (2011), 053106.

(108) Maes, D.; Vorontsova, M. A.; Potenza, M. A. . C.; Sanvito, T.; Sleutel, M.; Giglio, M.; Vekilov, P. G. Do Protein Crystals Nucleate within Dense Liquid Clusters ? *Acta Crystallogr. Sect. F* **2015**, *71* (7), 815–822.

(109) Vorontsova, M. A.; Chan, H. Y.; Lubchenko, V.; Vekilov, P. G. Lack of Dependence of the Sizes of the Mesoscopic Protein Clusters on Electrostatics. *Biophys. J.* **2015**, *109* (9), 1959–1968.

(110) Völkle, C. M.; Gebauer, D.; Cölfen, H. High-Resolution Insights into the Early Stages of Silver Nucleation and Growth. *Faraday Discuss.* **2015**, *179*.

(111) Olafson, K. N.; Rimer, J. D.; Vekilov, P. G. Growth of Large Hematin Crystals in Biomimetic Solutions. *Cryst. Growth Des.* **2014**, *14* (5), 2123–2127.

(112) Ketchum, M. A.; Olafson, K. N.; Petrova, E. V.; Rimer, J. D.; Vekilov, P. G. Hematin Crystallization from Aqueous and Organic Solvents. *J. Chem. Phys.* **2013**, *139* (12).

(113) Olafson, K. N.; Ketchum, M. A.; Rimer, J. D.; Vekilov, P. G. Mechanisms of Hematin Crystallization and Inhibition by the Antimalarial Drug Chloroquine. *Proc. Natl. Acad. Sci.* **2015**, *112* (16), 4946–4951.

(114) Vekilov, P. G.; Chung, S.; Olafson, K. N. Shape Change in Crystallization of Biological Macromolecules. *MRS Bull.* **2016**, *41* (5), 375–380.

(115) Olafson, K. N.; Rimer, J. D.; Vekilov, P. G. Early Onset of Kinetic Roughening Due to a Finite Step Width in Hematin Crystallization. *Phys. Rev. Lett.* **2017**,

119 (19), 1–6.

(116) Lupulescu, A. I.; Rimer, J. D. In Situ Imaging of Silicalite-1. *Science (80-.).* **2014**, *344*, 729–733.

(117) Van Eerdenbrugh, B.; Lo, M.; Kjoller, K.; Marcott, C.; Taylor, L. S. Nanoscale Mid-Infrared Evaluation of the Miscibility Behavior of Blends of Dextran or Maltodextrin with Poly(Vinylpyrrolidone). *Mol. Pharm.* **2012**, *9* (5), 1459–1469.

(118) Stadler, J.; Schmid, T.; Zenobi, R. Developments in and Practical Guidelines for Tip-Enhanced Raman Spectroscopy. *Nanoscale* **2012**, *4* (6), 1856.

(119) Bravais, A. *Etudes Crystallographique*; Sciences, A. des, Ed.; Paris, 1913.

(120) Gibbs, J. *The Collected Works*; Green and Co.: New York, 1928.

(121) Klamt, A.; Schüürmann, G. COSMO: A New Approach to Dielectric Screening in Solvents with Explicit Expressions for the Screening Energy and Its Gradient. *J. Chem. Soc., Perkin Trans. 2* **1993**, No. 5, 799–805.

(122) Kirkpatrick, S.; Gelatt, C. D. J.; Vecchi, M. P. Optimization by Simulated Annealing’. *Sci. Vol.* **1983**, *220pp* (4598), 671–680.

(123) Reutzel-Edens, S. M.; Bush, J. K.; Magee, P. A.; Stephenson, G. A.; Byrn, S. R. Anhydrates and Hydrates of Olanzapine: Crystallization, Solid-State Characterization, and Structural Relationship. *Cryst. Growth Des.* **2003**, *3* (6), 897–907.

(124) Wawrzycka-Gorczyca, I.; Borowski, P.; Osypiuk-Tomasik, J.; Mazur, L.; Koziol, A. E. Crystal Structure of Olanzapine and Its Solvates. Part 3. Two and Three-Component Solvates with Water, Ethanol, Butan-2-Ol and Dichloromethane. *J. Mol. Struct.* **2007**, *830* (1–3), 188–197.

(125) Dahan, A.; Miller, J. M.; Amidon, G. L. Prediction of Solubility and Permeability Class Membership : Provisional BCS Classification of the World ' s Top Oral Drugs. **2009**, *11* (4), 740–746.

(126) Fulton, B.; Goa, K. L. A Review of Its Pharmacological Properties and Therapeutic Related Psychoses. *Drugs* **1997**, *53* (2), 281–298.

(127) Sanger, T. M.; Grundy, S. L.; Gibson, P. J.; Namjoshi, M. A.; Greaney, M. G.; Tohen, M. F. Long-Term Olanzapine Therapy in the Treatment of Bipolar I Disorder: An Open-Label Continuation Phase Study. *J. Clin. Psychiatry* **2001**, *62* (4), 273–281.

(128) Thakuria, R.; Nangia, A. Olanzapinium Salts, Isostructural Solvates, and Their Physicochemical Properties. *Cryst. Growth Des.* **2013**, *13* (8), 3672–3680.

(129) Wawrzycka-Gorczyca, I.; Koziol, A. E.; Glice, M.; Cybulski, J. Polymorphic Form II of 2-Methyl-4-(4-Methyl-1-Piperazinyl)-10 *H* -Thieno[2,3- *b*][1,5]Benzodiazepine. *Acta Crystallogr. Sect. E Struct. Reports Online* **2004**, *60* (1), o66–o68.

(130) Ayala, A.; Siesler, H.; Boese, R. Solid State Characterization of Olanzapine Polymorphs Using Vibrational Spectroscopy. *Int. J. Pharm.* **2006**, *326*, 69–79.

(131) Sarmah, K. K.; Sarma, A.; Roy, K.; Rao, D. R.; Thakuria, R. Olanzapine Salts and Diversity in Molecular Packing. *Cryst. Growth Des.* **2015**, *16*, 1047–1055.

(132) Clarke, H. D.; Hickey, M. B.; Moulton, B.; Perman, J. a.; Peterson, M. L.; Wojtas, Ł.; Almarsson, Ö.; Zaworotko, M. J. Crystal Engineering of Isostructural Quaternary Multicomponent Crystal Forms of Olanzapine. *Cryst. Growth Des.* **2012**, *12* (8), 4194–4201.

(133) Paisana, M. C.; Wahl, M. A.; Pinto, J. F. Role of Moisture on the Physical Stability of Polymorphic Olanzapine. *Int. J. Pharm.* **2016**, *509*, 135–148.

(134) Davey, R. J.; Schroeder, S. L. M.; Ter Horst, J. H. Nucleation of Organic Crystals - A Molecular Perspective. *Angew. Chemie - Int. Ed.* **2013**, *52* (8), 2167–2179.

(135) Anwar, J.; Zahn, D. Uncovering Molecular Processes in Crystal Nucleation and Growth by Using Molecular Simulation. *Angew. Chemie* **2011**, *50* (9), 1996–2013.

(136) Anwar, J.; Khan, S.; Lindfors, L. Secondary Crystal Nucleation: Nuclei Breeding Factory Uncovered. *Angew. Chemie - Int. Ed.* **2015**, *54* (49), 14681–14684.

(137) Lee, C. H.; Schiros, T.; Santos, E. J. G.; Kim, B.; Yager, K. G.; Kang, S. J.; Lee, S.; Yu, J.; Watanabe, K.; Taniguchi, T.; et al. Epitaxial Growth of Molecular Crystals on van Der Waals Substrates for High-Performance Organic Electronics. *Adv. Mater.* **2014**, *26* (18), 2812–2817.

(138) Dunning, J. W. *Structure of Surfaces. In Physics and Chemistry of the Solid State*; D.; Labes, M. M. ., Weissburger, A., Eds.; Interscience: New York, 1965.

(139) Olmsted, B. K.; Ward, M. D. The Role of Chemical Interactions and Epitaxy during Nucleation of Organic Crystals on Crystalline Substrates. *CrystEngComm* **2011**, *13*, 1070.

(140) Lee, A. Y.; Lee, I. S.; Dette, S. S.; Boerner, J.; Myerson, A. S. Crystallization on Confined Engineered Surfaces: A Method to Control Crystal Size and Generate Different Polymorphs. *J. Am. Chem. Soc.* **2005**, *127* (43), 14982–14983.

(141) Singh, A.; Lee, I. S.; Myerson, A. S. Concomitant Crystallization of ROY on Patterned Substrates : Using a High Throughput Method to Improve the Chances of Crystallization of Different Polymorphs Concomitant Crystallization of ROY on Patterned Substrates : Using a High Throughput Method to Im. **2009**, 2–5.

(142) Poloni, L. N.; Zhong, X.; Ward, M. D.; Mandal, T. Best Practices for Real-Time in Situ Atomic Force and Chemical Force Microscopy of Crystals. *Chem. Mater.* **2017**, *29* (1), 331–345.

(143) Cui, Y.; Myerson, A. S. Experimental Evaluation of Contact Secondary Nucleation Mechanisms. *Cryst. Growth Des.* **2014**, *14* (10), 5152–5157.

(144) Debenedetti, P. G. *Metastable Liquids: Concepts and Principals*; Princeton University Press, 1996.

(145) Warzecha, M.; Guo, R.; Bhardwaj, R. M.; Reutzel-Edens, S. M.; Price, S. L.; Lamprou, D.; Florence, A. J. Direct Observation of Templated Two-Step Nucleation Mechanism during Olanzapine Hydration. *Cryst. Growth Des.* **2017**, *17* (12), 6382–6393.

(146) Rodríguez-Hornedo, N.; Lechuga-Ballesteros, D. Phase Transition and Heterogeneous/Epitaxial Nucleation of Hydrated and Anhydrous Theophylline Crystals. *Int. J. Pharm.* **1992**, *85* (1–3), 149–162.

(147) Vekilov, P. G. Sickle-Cell Haemoglobin Polymerization : Is It the Primary Pathogenic Event of Sickle-Cell Anaemia ? *Br. J. Haematol.* **2007**, *139*, 173–184.

(148) Walsh, G. Therapeutic Insulins and Their Large-Scale Manufacture. **2005**, *67*, 151–159.

(149) Pan, W.; Galkin, O.; Filobelo, L.; Nagel, R. L.; Vekilov, P. G. Metastable Mesoscopic Clusters in Solutions of Sickle-Cell Hemoglobin. *Biophys. J.* **2007**, *92* (1), 267–277.

(150) Byington, M. C.; Safari, M. S.; Conrad, J. C.; Vekilov, P. G. Protein Conformational Flexibility Enables the Formation of Dense Liquid Clusters: Tests Using Solution Shear. *J. Phys. Chem. Lett.* **2016**, *7* (13), 2339–2345.

(151) Erdemir, D.; Lee, A. Y.; Myerson, A. S. Nucleation of Crystals from Solution: Classical and Two-Step Models. *Acc. Chem. Res.* **2009**, *42* (5), 621–629.

(152) De Yoreo, J. Crystal Nucleation: More than One Pathway. *Nat. Mater.* **2013**, *12*

(4).

(153) Bonnett, P. E.; Carpenter, K. J.; Dawson, S.; Davey, R. J. Solution Crystallisation via a Submerged Liquid – Liquid Phase Boundary : Oiling Out. *Chem. Commun.* **2003**, 698–699.

(154) Sedlak, M.; Rak, D. Large-Scale Inhomogeneities in Solutions of Low Molar Mass Compounds and Mixtures of Liquids : Supramolecular Structures or Nanobubbles ? *J. Phys. Chem. B* **2013**, *117*, 2495–2504.

(155) Chaikin, P. .; Lubensky, T. . *Principles of Condensed Matter Physics*; Cambridge University Press: Cambridge, 1995.

(156) Johnston, K. P.; Maynard, J. A.; Truskett, T. M.; Borwankar, A. U.; Miller, M. A.; Wilson, B. K.; Dinin, A. K.; Khan, T. A.; Kaczorowski, K. J. Concentrated Dispersions of Equilibrium Protein Nanoclusters That Reversibly Dissociate into Active Monomers. *ACS Nano* **2012**, *6* (2), 1357–1369.

(157) Stradner, A.; Sedgwick, H.; Cardinaux, F.; Poon, W. C. K.; Egelhaaf, S. U. P. S. Equilibrium Cluster Formation in Concentrated Protein Solutions and Colloids. *Nature* **2004**, *432*, 492–495.

(158) Porcar, L.; Falus, P.; Chen, W.-R.; Faraone, A.; Fratini, E.; Hong, K.; Baglioni, P.; Liu, Y. Formation of the Dynamic Clusters in Concentrated Lysozyme Protein Solutions. *J. Phys. Chem. Lett.* **2010**, *1* (1), 126–129.

(159) Erlkamp, M.; Grobelny, S.; Faraone, A.; Czeslik, C.; Winter, R. Solvent Effects on the Dynamics of Amyloidogenic Insulin Revealed by Neutron Spin Echo

Spectroscopy. *J. Phys. Chem. B* **2014**, *118* (12), 3310–3316.

(160) Borwankar, A. U.; Dinin, A. K.; Laber, J. R.; Twu, A.; Wilson, B. K.; Maynard, J. A.; Truskett, T. M.; Johnston, K. P. Tunable Equilibrium Nanocluster Dispersions at High Protein Concentrations. *Soft Matter* **2013**, *9* (6), 1766–1771.

(161) Soraruf, D.; Roosen-Runge, F.; Grimaldo, M.; Zanini, F.; Schweins, R.; Seydel, T.; Zhang, F.; Roth, R.; Oettel, M.; Schreiber, F. Protein Cluster Formation in Aqueous Solution in the Presence of Multivalent Metal Ions – a Light Scattering Study. *Soft Matter* **2014**, *10* (6), 894–902.

(162) Yearley, E. J.; Godfrin, P. D.; Perevozchikova, T.; Zhang, H.; Falus, P.; Porcar, L.; Nagao, M.; Curtis, J. E.; Gawande, P.; Taing, R.; et al. Observation of Small Cluster Formation in Concentrated Monoclonal Antibody Solutions and Its Implications to Solution Viscosity. *Biophys. J.* **2014**, *106* (8), 1763–1770.

(163) Cardinaux, F.; Stradner, A.; Schurtenberger, P.; Sciortino, F.; Zaccarelli, E. Modeling Equilibrium Clusters in Lysozyme Solutions. *EPL (Europhysics Lett.* **2007**, *77* (4), 48004.

(164) Schubert, R.; Meyer, A.; Baitan, D.; Dierks, K.; Perbandt, M.; Betzel, C. Real-Time Observation of Protein Dense Liquid Cluster Evolution during Nucleation in Protein Crystallization. *Cryst. Growth Des.* **2017**, *17* (3), 954–958.

(165) Lutsko, J. F.; Niclois, G. Mechanism for the Stabilization of Protein Clusters above the Solubility Curve: The Role of Non-Ideal Chemical Reactions. *Soft Matter* **2016**, *28* (24), 93–98.

(166) Byington, M. C.; Safari, M. S.; Conrad, J. C.; Vekilov, P. G. Shear Flow Suppresses the Volume of the Nucleation Precursor Clusters in Lysozyme Solutions. *J. Cryst. Growth* **2017**, *468* (December 2016), 493–501.

(167) Derewenda, Z. S.; Vekilov, P. G. Entropy and Surface Engineering in Protein Crystallization. *Acta Crystallogr. Sect. D Biol. Crystallogr.* **2006**, *62* (1), 116–124.

(168) Leckband, D.; Israelachvili, J. Intermolecular Forces in Biology. *Q. Rev. Biophys.* **2001**, *42* (2), 105–267.

(169) Raviv, U.; Klein, J. Fluidity of Bound Hydration Layers. *Science (80-.).* **2002**, *297* (5586), 1540–1544.

(170) Ball, P. Water as an Active Constituent in Cell Biology. *Chem. Rev.* **2008**, *108* (1), 74–108.

(171) Pal, S. K.; Zewail, A. H. Dynamics of Water in Biological Recognition. *Chem. Rev.* **2004**, *104* (4), 2099–2124.

(172) Eisenberg, D.; Kauzamann, W. *The Structure and Properties of Water*; University Press: Oxford, 1969.

(173) Eisenberg, D.; Crothers, D. *Physical Chemistry with Application to Life Sciences*; The Benjamin/Cummins: Menlo Park, 1979.

(174) Dunitz, J. D. The Entropic Cost of Bound Water in Crystals and Biomolecules. *Science (80-.).* **1994**, *264* (5159), 670–670.

(175) Fresht, A. *Structure and Mochanism in Protein Science*; W.H. Freeman: New York, 1999.

(176) Haynes, W. . *CRC Handbook of Chemistry and Physics*; CRC Press: Boca Raton, 2011.

(177) Dill, K.; Bromberg, S. *Molecular Driving Forces: Statistical Thermodynamics in Biology, Chemistry, Physics and Nanoscience*; Science, G., Ed.; Garland Science: New York, 2011.

(178) Petsev, D. N.; Vekilov, P. G. Evidence for Non-DLVO Hydration Interactions in Solutions of the Protein Apoferritin. *Phys. Rev. Lett.* **2000**, *84* (6), 1339–1342.

(179) Berry, P.; Rice, S. .; Ross, J. *Physical Chemistry. Second Ed.*; Oxford University Press: New York, 2000.

(180) Sun, Y.; Zhu, L.; Wu, T.; Cai, T.; Gunn, E. M.; Yu, L. Stability of Amorphous Pharmaceutical Solids: Crystal Growth Mechanisms and Effect of Polymer Additives. *AAPS J.* **2012**, *14* (3), 380–388.

(181) Shtukenberg, A. G.; Poloni, L. N.; Zhu, Z.; An, Z.; Bhandari, M.; Song, P.; Rohl, A. L.; Kahr, B.; Ward, M. D. Dislocation-Actuated Growth and Inhibition of Hexagonal L -Cystine Crystallization at the Molecular Level. *Cryst. Growth Des.* **2015**, *15* (2), 921–934.

(182) Sarmah, K. K.; Sarma, A.; Roy, K.; Rao, D. R.; Thakuria, R.; Frincu, M. C.; Fleming, S. D.; Rohl, A. L.; Swift, J. A. The Epitaxial Growth of Cholesterol

Crystals from Bile Solutions on Calcite Substrates. *Cryst. Growth Des.* **2004**, *126* (25), 7915–7924.

(183) Gliko, O.; Neumaier, N.; Fischer, M.; Haase, I.; Bacher, A.; Weinkauf, S.; Vekilov, P. G. Dense Liquid Droplets as a Step Source for the Crystallization of Lumazine Synthase. *J. Cryst. Growth* **2005**, *275*, 1409–1416.

(184) Gliko, O.; Reviakine, I.; Vekilov, P. G. Stable Equidistant Step Trains during Crystallization of Insulin. *Phys. Rev. Lett.* **2003**, *90* (22), 4.

(185) Land, T. A.; De Yoreo, J. J. The Evolution of Growth Modes and Activity of Growth Sources on Canavalin Investigated by in Situ Atomic Force Microscopy. *J. Cryst. Growth* **2000**, *208* (1–4), 623–637.

(186) De Yoreo, J. J. In-Situ Liquid Phase TEM Observations of Nucleation and Growth Processes. *Progress in Crystal Growth and Characterization of Materials*. 2016.

(187) Keefer, K. D.; Schaefer, D. W. Growth of Fractally Rough Colloids. *Phys. Rev. Lett.* **1986**, *56* (11), 2376–2379.

(188) Dalmaschio, C. J.; Ribeiro, C.; Leite, E. R. Impact of the Colloidal State on the Oriented Attachment Growth Mechanism. *Nanoscale* **2010**, *2* (11), 2336–2345.

(189) Gidalevitz, D.; Feidenhans'l, R.; Matlis, S.; Smilgies, D.-M.; Christensen, M. J.; Leiserowitz, L. Monitoring In Situ Growth and Dissolution of Molecular Crystals: Towards Determination of the Growth Units. *Angew. Chemie Int. Ed. English* **1997**, *36* (9), 955–959.

(190) Huang, J.; Stringfellow, T. C.; Yu, L. Glycine Exists Mainly as Monomers, Not Dimers, in Supersaturated Aqueous Solutions: Implications for Understanding Its Crystallization and Polymorphism. *J. Am. Chem. Soc.* **2008**, *130* (42), 13973–13980.

(191) Chen, J.; Trout, B. L. A Computational Study of the Mechanism of the Selective Crystallization of α- and β-Glycine from Water and Methanol - Water Mixture. **2010**, *114*, 13764–13772.

(192) Hamad, S.; Catlow, C. R. A. Are Glycine Cyclic Dimers Stable in Aqueous Solution? *CrystEngComm* **2011**, *13*, 4304.

(193) Burton, R. C.; Ferrari, E. S.; Davey, R. J.; Finney, J. L.; Bowron, D. T. The Relationship between Solution Structure and Crystal Nucleation: A Neutron Scattering Study of Supersatruated Methanolic Soltions of Benzoic Acid. *J. Phys. Chem. B* **2010**, *114* (26), 8807–8816.

(194) Chiarella, R. a; Gillon, A. L.; Burton, R. C.; Davey, R. J.; Sadiq, G.; Auffret, A.; Cioffi, M.; Hunter, C. a. The Nucleation of Inosine: The Impact of Solution Chemistry on the Appearance of Polymorphic and Hydrated Crystal Forms. *Faraday Discuss.* **2007**, *136*, 179–193;

(195) Niederberger, M.; Cölfen, H. Oriented Attachment and Mesocrystals: Non-Classical Crystallization Mechanisms Based on Nanoparticle Assembly. *Phys. Chem. Chem. Phys.* **2006**, *8* (28), 3271–3287.

(196) Kumar, M.; Luo, H.; Román-Leshkov, Y.; Rimer, J. D. SSZ-13 Crystallization by Particle Attachment and Deterministic Pathways to Crystal Size Control. *J.*

Am. Chem. Soc. **2015**, *137* (40), 13007–13017.

(197) Gower, L. B. Biomimetic Model Systems for Investigating the Amorphous Precursor Pathway and Its Role in Biomineralization. *Chem. Rev.* **2008**, *108* (11), 4551–4627.

(198) Dunitz, J. D. Are Crystal Structures Predictable? *Chem. Commun. (Camb).* **2003**, No. 5, 545–548.

(199) Price, S. L.; Reutzel-Edens, S. M. The Potential of Computed Crystal Energy Landscapes to Aid Solid-Form Development. *Drug Discov. Today* **2016**, *21* (6), 912–923.

(200) Price, S. L.; Braun, D. E.; Reutzel-Edens, S. M. Can Computed Crystal Energy Landscapes Help Understand Pharmaceutical Solids? *Chem. Commun.* **2016**, *52* (52), 7065–7077.

(201) Vekilov, P. G. What Determines the Rate of Growth of Crystals from Solution? *Cryst. Growth Des.* **2007**, *7* (12), 2796–2810.

(202) Li, J.; Tilbury, C. J.; Joswiak, M. N.; Peters, B.; Doherty, M. F. Rate Expressions for Kink Attachment and Detachment during Crystal Growth. *Cryst. Growth Des.* **2016**, *16* (6), 3313–3322.

(203) Eyring, H.; Lin, S. H.; Lin, S. M. *Basic Chemical Kinetics*; John Wiley and Sons: New York, 1980.

(204) Houston, P. L. *Chemical Kinetics and Reaction Dynamics*; McGraw-Hill Higher Education: New York, 2001.

(205) Chernov, A. A. The Spiral Growth of Crystals. *Sov. Phys. Uspekhi* **1961**, *4* (1), 116–148.

(206) Van der Eerden, J. P. *In Handbook of Crystal Growth*; Hurle, D., Ed.; North Holland: Amsterdam, 1994.

(207) Georgiou, D. K.; Vekilov, P. G. A Fast Response Mechanism for Insulin Storage in Crystals May Involve Kink Generation by Association of 2D Clusters. *Proc. Natl. Acad. Sci. U. S. A.* **2006**, *103* (6), 1681–1686.

(208) Voronkov, V. The Movement of an Elementary Step by Means of the Formation of One-Dimensional Nuclei. *Sov. Phys. Cryst* **1970**, *15*, 8–13.

(209) Teng, H. H.; Dove, P. M.; De Yoreo, J. J. Kinetics of Calcite Growth: Surface Processes and Relationships to Macroscopic Rate Laws. *Geochim. Cosmochim. Acta* **2000**, *64* (13), 2255–2266.

(210) Cabrera, N. .; Vermileya, D. A. *Growth and Perfection of Crystals*; Doremus, R. H., Roberts, B. W., Turnbul, D., Eds.; Wiley: New York, 1958.

(211) Voronkov, V. V; Rashkovich, L. N. Step Kinetics in the Presence of Mobile Adsorbed Impurity. *J. Cryst. Growth* **1994**, *144* (1), 107–115.

(212) Maruyama, M.; Tsukamoto, K.; Sazaki, G.; Nishimura, Y.; Vekilov, P. G. Chiral and Achiral Mechanisms of Regulation of Calcite Crystallization. *Cryst. Growth Des.* **2009**, *9* (1), 127–135.

(213) Bostanov, V.; Staikov, G.; Roe, D. K. Rate of Propagation of Growth Layers on Cubic Crystal Faces in Electrocrystallization of Silver. **1975**, *122* (10), 2–6.

(214) Rashkovich, L. N.; Chernov, A. A. Limited Rate of Fluctuations May Influence Crystal Growth Morphology. *Japanese Assoc. Cryst. Growth* **2001**, *34*, 330–334.

(215) Bennema, P. Analysis of Crystal Growth Models for Slightly Supersaturated Solutions. *J. Cryst. Growth* **1967**, *1* (5), 278–286.

(216) Gilmer, G. H.; Ghez, R.; Cabrera, N. An Analysis of Combined Surface and Volume Diffusion Processes in Crystal Growth. *J. Cryst. Growth* **1971**, *8* (1), 79–93.

(217) Akkermans, R. L. C.; Spenley, N. A.; Robertson, S. H. Monte Carlo Methods in Materials Studio. *Molecular Simulation*. Taylor & Francis 2013, pp 1153–1164.

(218) Kulkarni, S. a.; Weber, C. C.; Myerson, A. S.; ter Horst, J. H. Self-Association during Heterogeneous Nucleation onto Well-Defined Templates. *Langmuir* **2014**, *30* (41), 12368–12375.

(219) Wikström, H.; Rantanen, J.; Gift, A. D.; Taylor, L. S.; Wikstrom, H. Toward an Understanding of the Factors Influencing Anhydrate-to-Hydrate Transformation Kinetics in Aqueous Environments. *Cryst. Growth Des.* **2008**, *8* (8), 2684–2693.